University of California
Santa Barbara

(Thermo)Dynamics of Ultracold Quantum Degenerate Gases

A dissertation submitted in partial satisfaction
of the requirements for the degree

Doctor of Philosophy
in
Physics

by

Ethan Q. Simmons

Committee in charge:

Professor David Weld, Chair
Professor Andrew Jayich
Professor Matthew Fisher

March 2024

The Dissertation of Ethan Q. Simmons is approved.

Professor Andrew Jayich

Professor Matthew Fisher

Professor David Weld, Committee Chair

March 2024

(Thermo)Dynamics of Ultracold Quantum Degenerate Gases

by

Ethan Q. Simmons

No touching!
- George Oscar Bluth, Sr.

Acknowledgements

To my parents, Motherland and Daddio, you've both wanted the best for me and have fully supported me from the day I was born. You have helped me move forward, persist and be resilient in the most challenging and difficult of times, showing me the light ahead when I couldn't see it. Without you both, I would never have gotten this far, and I'm so profoundly grateful to have you as parents.

To my sister Emma/bro/brolioli/heeeeeeeeeey brother, your wicked sense of humor and our inside jokes have brought levity and joy in times of stress, and words can't express how vital that has been in keeping me afloat on this long journey. Further, it has been an honor and an absolute privilege to watch you grow up, define who you are, what you stand for and fight for what's right and what matters to you. You are a treasure, and I hope you always remember that.

To Roshan, the subject of my as-of-yet unwritten bromance novel, all I can is, "Okay, one Krabby Patty and one room with cheese. Oh, and can I get cheese on the Krabby Patty, too?". People doing precision measurement experiments should really be studying you instead of atomic transitions because you are the most consistent, reliable and rock-steady object in the known universe. Day in, day out, you've shown up with a positive and open-minded attitude and slogged through the rough times, like all those summers where we were plumbing interns...BUUUUUUUUCKET MAAAAAAAAN. No matter how hard we were banging our heads against the wall, you always found humor in the moment and provided catharsis. I couldn't have asked for a better lab mate and friend, and I wouldn't be where I am today without you.

To David, I will be forever grateful to you for the opportunity to be a part of this group. You have always supported and encouraged thinking outside the box, and your genuine scientific curiosity and excitement has been contagious. Some of my fondest

memories are of the periods of scientific exploration during which we had no agenda and were encouraged to come up with and test out new experimental ideas. Further, I have been grateful to have an advisor who I identify as an actual human being (rare in physics), as evidenced by our shared appreciation of *Arrested Development*. Your feedback, guidance and encouragement have helped me to grow and evolve into the scientist I am today.

To the village of people (not to be confused with the *Village People*) who have guided and supported me on this incredible journey, know that each and every one of you has played a critical role in getting me to this point, whether undergrad or grad student or post-doc or staff. From the bottom of my heart, I am deeply grateful for every single one of you.

And finally, my acknowledgements wouldn't be complete if I didn't give credit to those who made the late data-collection nights and pushes through low-energy afternoons possible. Ava Max, you'll probably never read this, but you are my personal hero. Additionally, the sweet bass drops of Da Tweekaz, The Chainsmokers and *Blood is Pumping* from the *Blade* club scene have been revitalizing forces and allowed me to push on...FOR SCIENCE.

Curriculum Vitæ

Ethan Q. Simmons

Education

2024	Ph.D. in Physics (Expected), University of California, Santa Barbara.
2021	M.A. in Physics, University of California, Santa Barbara.
2015	B.A. in Physics, University of California, Berkeley.

Publications

Thermodynamic engine with a quantum degenerate working fluid. **E.Q. Simmons**, R. Sajjad, K. Keithley, H. Mas, J.L. Tanlimco, E. Nolasco-Martinez, Y. Bai, G.H. Fredrickson, and D.M. Weld. *Phys. Rev. Research* **5**, L042009 (2023)

Interaction-driven breakdown of dynamical localization in a kicked quantum gas. A. Cao, R. Sajjad, H. Mas, **E.Q. Simmons**, J.L. Tanlimco, E. Nolasco-Martinez, T. Shimasaki, H.E. Kondakci, V. Galitski, and D.M. Weld. *Nature Physics* **18**, 1302-1306 (2022).

Observation of the quantum boomerang effect. R. Sajjad, J.L. Tanlimco, H. Mas, A. Cao, E. Nolasco-Martinez, **E.Q. Simmons**, F.L.N. Santos, P. Vignolo, T. Macrì, and D.M. Weld. *Phys. Rev. X* **12**, 011035 (2022).

Transport controlled by Poincaré orbit topology in a driven inhomogeneous lattice gas. A. Cao, R. Sajjad, **E.Q. Simmons**, C.J. Fujiwara, T. Shimasaki, and D.M. Weld. *Phys. Rev. Research* **2**, 032032(R) (2020).

Probing Nonexponential Decay in Floquet-Bloch Bands. A. Cao, C.J. Fujiwara, R. Sajjad, **E.Q. Simmons**, E. Lindroth, and D.M. Weld. *Zeitschrift für Naturforschung A* **75**, 5, 443-448 (2020).

Atom-interferometry constraints on dark energy. P. Hamilton, M. Jaffe, P. Haslinger, **Q. Simmons**, H. Müller, and J. Khoury. *Science* **349**, 849-851 (2015).

Abstract

(Thermo)Dynamics of Ultracold Quantum Degenerate Gases

by

Ethan Q. Simmons

Quantum degenerate gases, in the form of Bose-Einstein condensates, are ideal objects for probing fundamental quantum mechanical phenomena. These platforms are highly isolated, and enable coherent control and manipulation of quantum matter with exquisite precision. The work presented in this thesis utilizes quantum degenerate gases of bosonic ^{7}Li which have tunable interactions, allowing for studies of both single-particle and many-body physics. By subjecting these gases to periodic driving, a rich and diverse landscape of physical phenomena is unlocked. I will first describe our work realizing a thermodynamic engine with a quantum degenerate working fluid, achieved via slow periodic driving, and the effect of quantum degeneracy on engine performance. In the regime of fast driving, I will then propose a scheme for a noise-tolerant continuously-trapped atom interferometer.

Contents

Chapter 1

Introduction

There are very few contexts in which $\sim 10^5$-10^6 particles, all completely identical, occupy the same exact quantum state, evolve according to the same Hamiltonian, and are otherwise completely isolated. Ultracold quantum gas experiments, which trap and cool neutral atoms to temperatures just billionths of degrees above absolute zero, are able to create such an environment. In these settings, the wave-like nature of each atom is on full display, and the fascinating (and sometimes frustrating) unintuitive and counterintuitive nature of quantum mechanics becomes accessible in these highly isolated and precisely controlled platforms. The ability to prepare a macroscopic number of quantum particles and manipulate them by subjecting them to a Hamiltonian of interest enables probes of fundamental quantum mechanical behavior.

Ultracold quantum gas experiments can be used to study a wide range of physical models and phenomena, which is a direct result of the high degree of flexibility and control that the experimentalist has over the Hamiltonian. Subjecting a quantum gas to a Hamiltonian which is analogous to that which governs another physical system of interest, e.g. electrons in a crystal lattice, the field of quantum simulation or quantum emulation emerges. That is, by studying the behavior and dynamics of the ultracold gas,

insights into the physics of the analogous system are revealed.

Tunable interparticle interactions add to the rich variety of physics that can be explored with ultracold gases. Our experiment uses bosonic ^{7}Li which has a broad magnetic Feshbach resonance, allowing us to apply a DC magnetic field to set the s-wave scattering length between atoms. The presence of this Feshbach resonance allows us to tune interactions from infinitely repulsive, to non-interacting, to infinitely attractive, and anywhere in between. Tunable interactions enable investigations of single-particle physics if operating in the non-interacting regime, or probes of interaction effects and studies of many-body physics in the attractive or repulsive interaction regimes.

An additional axis of control is gained by subjecting quantum gases to periodic driving, i.e. cyclic variation of some parameter(s) in the Hamiltonian in time. Nearly all of the experiments done on our ^{7}Li apparatus have harnessed the power of periodic driving, and the work I present in this thesis is no exception. Our first result is achieved using extremely slow driving while the second result drives about five orders of magnitude faster, and these two regimes of driving give rise to dramatically different novel physics.

In the next chapter, I will cover the key concepts which underlie our experimental platform and our research. Chapter 3 gives an overview of our experimental apparatus, goes through the cooling stages required to create a quantum degenerate gas, and discusses how we perform readout using absorption imaging. Chapter 4 covers important properties of harmonically-trapped condensates, while chapter 5 discusses the behavior of BECs in both static and driven optical lattices. Chapter 6 presents our work realizing an isentropic thermodynamic engine with a quantum degenerate working fluid in the regime of very slow driving. In chapter 7, we propose a scheme for realizing a noise-robust continuously-trapped atom interferometer and discuss our experimental progress towards this goal. The appendices contain notes about experimental techniques and procedures.

1.1 Permissions and Attributions

1. Much of the theoretical content presented in this thesis is adapted from the following sources: *Atomic Physics* by C.J. Foot [1], *Bose-Einstein Condensation* by L. Pitaevskii and S. Stringari [2], *Bose-Einstein Condensation in Dilute Gases* by C.J. Pethick and H. Smith [3], and *Floquet engineering with quasienergy bands of periodically driven optical lattices* by M. Holthaus [4].

2. The content of chapter 6 is the result of a collaobration with Roshan Sajjad, Kimberlee Keithley, Hector Mas, Jeremy L. Tanlimco, Eber Nolasco-Martinez, Yifei Bai, Glenn H. Fredrickson, and David M. Weld, and has previously appeared in *Physical Review Research* [5]. It is reproduced here with the permission of the American Physical Society: `https://journals.aps.org/copyrightFAQ.html`.

Chapter 2

Background

The works presented in this thesis both harness the power of periodic driving to create two very different quantum devices. In the regime of very slow driving ($\sim$2 Hz), where adiabaticity is maintained to a high degree, alternating cyclic variation of harmonic trap frequency and interparticle scattering length produce a thermodynamic engine where the condensate acts as a working fluid. In a vastly different regime of drive frequency ($\sim$50-150 kHz) and interaction strength ($a_s = 0a_0$), amplitude modulation of an optical lattice enables versatile engineering of position-space trajectories and, in principle, this periodic driving can be used to synthesize a noise-robust continuously-trapped atom interferometer.

This chapter aims to give context for and motivate these works by providing an overview of the relevant concepts and techniques for our experimental platform. Specifically, we discuss the benefits of using ^{7}Li in an ultracold quantum gas experiment and explain the phenomenon of magnetic Feshbach resonance. We then justify the significant added complexity in creating Bose-Einstein condensates by detailing their advantages as coherent quantum objects, particularly in the context of quantum simulation. In the final section, we describe how periodic driving can be used as a powerful axis of control

in quantum simulation experiments.

2.1 Neutral ^{7}Li

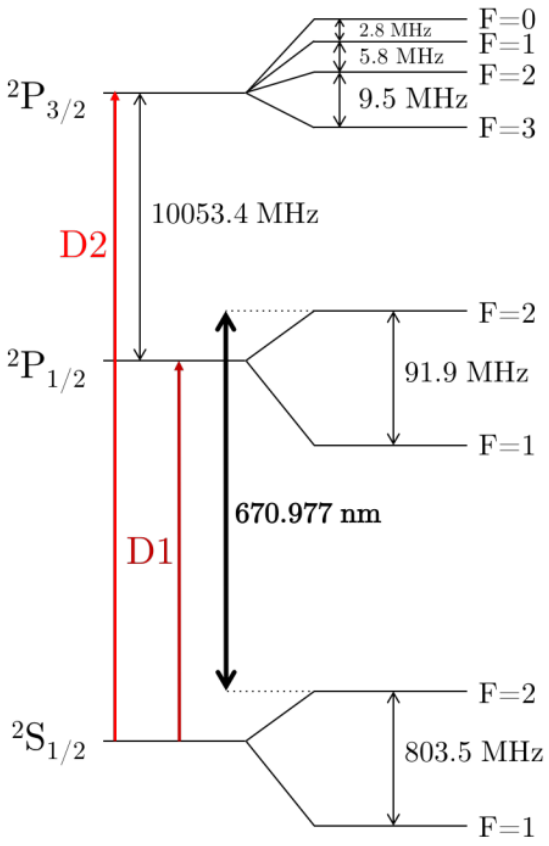

Figure 2.1: Level structure of ^{7}Li reproduced from [6].

Our experimental apparatus is single-species and uses neutral bosonic ^{7}Li, which has a number of properties that make it well-suited to studies of fundamental quantum mechanical phenomena:

1. ^{7}Li has a broad magnetic Feshbach resonance (to be discussed further shortly) which allows interparticle scattering to be tuned through application of a DC magnetic

field. The resonance at 736.8 Gauss is experimentally accessible and enables studies in the attractive, repulsive and non-interacting regimes.

2. ^{7}Li has a low mass of 7 amu which results in fast dynamics and tunneling, with the former occurring on spatial scales resolvable on our imaging camera.

3. As an alkali metal with a single valence electron, the level structure of ^{7}Li is relatively simple and the primary cooling transition around 671 nm is addressable with commercial lasers.

4. The two hyperfine ground states are separated by 803.5 MHz which allows a single source of resonant light to be shifted using a radiofrequency (RF) source and electro-optic modulator (EOM) so that transitions from both ground states are addressed.

2.2 Magnetic Feshbach resonances

As previously mentioned, a key feature of ^{7}Li is its broad magnetic Feshbach resonance which allows us to tune interparticle interactions with an applied DC magnetic field. Here, we give a brief description of this phenomenon, but a thorough treatment of Feshbach resonances can be found in [8].

Consider the interaction between just two atoms, for which there are two possible scattering processes: the atoms can scatter off of each other, or they can form a molecular bound state. The former is referred to as the open channel, while the latter is known as the closed channel, and the left diagram in figure 2.2 shows cartoon interatomic potentials for both of these channels. The bound and scattering states have different magnetic moments, which means that the relative energy between them changes with an applied DC magnetic field B.

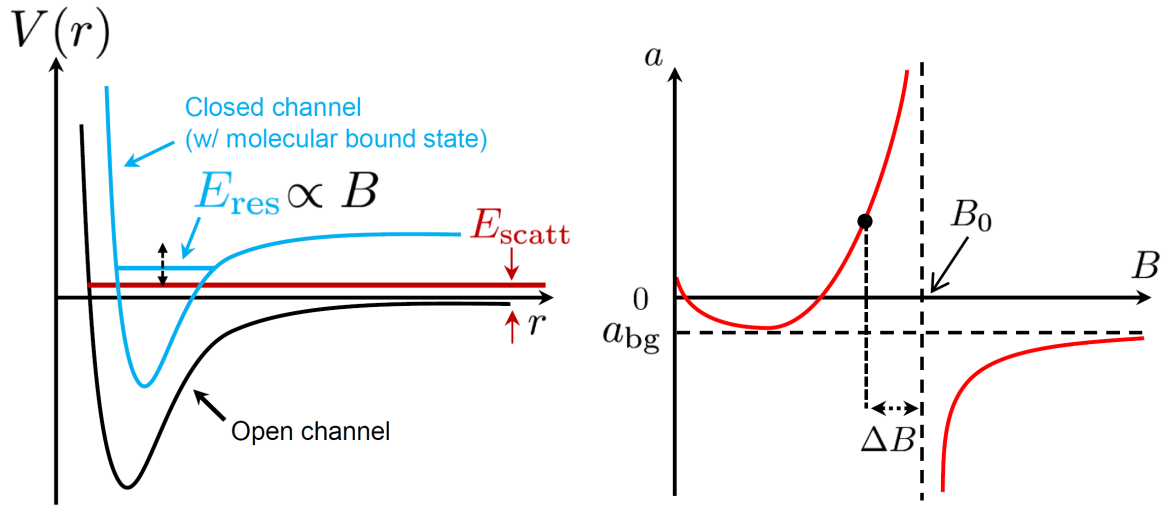

Figure 2.2: Left: cartoon interatomic potentials for the scattering state (open channel, black curve) and the bound state (closed channel, blue curve), with associated energies $E_{\rm scatt}$ and $E_{\rm res}$, respectively. Energetic separation between $E_{\rm scatt}$ and $E_{\rm res}$ depends on applied field B, and resonance occurs when $E_{\rm res} = E_{\rm scatt}$. Right: cartoon of scattering length as a function of magnetic field. Resonance occurs at field B_0 and is indicated by vertical dashed line. Distance away from resonance ΔB determines s-wave scattering length a, and a_{bg} is the background scattering length. Figure reproduced from [7].

A Feshbach resonance occurs when $E_{\rm res}$ is equal to the scattering state energy $E_{\rm scatt}$, where the s-wave scattering between atoms diverges, as shown in the right diagram of figure 2.2. Near the resonance, significant mixing occurs between the two channels and, due to their differing magnetic moments, the mixture of these states depends on the magnetic field. This results in a field-dependent scattering length $a_s(B)$, which is approximately given by the following functional form in the vicinity of the resonance [9]:

$$a_s(B) = a_{\rm BG}\left(1 - \frac{\Delta}{B - B_0}\right), \tag{2.1}$$

where $a_{\rm BG} = -24.5a_0$, $\Delta = -192.3$ G, and $B_0 = 736.8$ G for the $|1,1\rangle$ hyperfine state of ^{7}Li. Here, B is the applied field, B_0 is the location of the resonance, Δ is its width, and $a_{\rm BG}$ is the background scattering length, with a_0 the Bohr radius. The field at which

atoms are non-interacting, i.e. where $a_s = 0a_0$, is approximately 543.6 G.

The accessible magnetic Feshbach resonance in ^{7}Li is a powerful tool which allows us explore many different interaction regimes and investigate both non-interacting, i.e. single-particle, and many-body phenomena.

2.3 Bose-Einstein condensation

The process of creating an ultracold, quantum degenerate gas around 200-400 nK is significantly more complex than creating a cold gas at ~ 100 μK, so it is worth discussing the benefits of using a Bose-Einstein condensate (BEC) as our experimental starting point given the effort involved.

As the term "ultracold" implies, BECs are very cold objects with very low kinetic energy. Low kinetic energy reduces the degree to which the cloud expands over the course of an experiment. Additionally, the entropy associated with a condensate is small as the majority of atoms occupy the same ground state. In fact, the condensate itself possesses zero entropy for precisely this reason, and it is only the presence of "non-condensed" thermal atoms that gives the combined ensemble non-zero entropy. Therefore, this is a maximally clean starting point for quantum simulation experiments which are not aimed at simulating thermal phenomena.

Bose statistics, which enable condensation, result in Bose-enhancement of the density distribution which makes interparticle interactions extremely important and allows us to observe interaction-induced effects. Further, a high density in a single quantum state results in a quantum object with a very "bright" signal.

The high degree of isolation and control required to create a condensate mean that a BEC is strongly insulated against the lab environment. Control and manipulation are achieved using optical and magnetic fields whose timing and strength can be set precisely

using control hardware. Using these fields, we can create and subject a BEC to Hamiltonians of interest and study the resulting behavior and dynamics. If the Hamiltonian of interest maps directly onto that of another physical system, e.g. electrons in a lattice, studying the dynamics on our ultracold atom experiment is dubbed quantum emulation or quantum simulation, and this is discussed further in the next section. We can probe dynamics which may be otherwise challenging to study in the actual system, with the added benefits of greater control and longer coherence and relaxation times. Taken together, these factors make a BEC experiment an ideal testbed for studying quantum mechanical phenomena.

2.4 Quantum simulation with ultracold atoms

Now that we have a dense, coherent quantum object in an isolated environment, we can perform quantum simulation by subjecting our atoms to a Hamiltonian which directly maps the behavior of another system of interest. This provides a number of benefits, the first being that our experiment is an "analog" quantum simulator. As opposed to simulations performed on digital platforms (computers) using classical bits, the atoms in our experiments are truly quantum mechanical objects. What better way is there to simulate a quantum mechanical system of interest than by using quantum mechanical objects? Interference, scattering, coherence, entanglement, and superposition are all inherently accounted for. A second benefit of our platform is its "cleanliness", i.e. the high degree of isolation between our ultracold atoms and other particles, in addition to the quantum state purity endowed by bosonic statistics.

Much of the quantum simulation work done by our group has made use of optical lattices, which are standing waves of light with spatially-periodic intensity profiles. In the simplest case, an optical lattice is formed by retro-reflecting a laser beam back on

itself using a mirror. The intensity profiles of optical lattices give rise to spatially-periodic potential landscapes, and for lattice light red-detuned from resonance, the nodes and anti-nodes correspond to potential minima and maxima, respectively. Thus, optical lattices can be used to mimic the potential landscape of electrons in a crystal lattice, as one example, and they can be made in multiple dimensions or imbued with exotic properties to model other condensed matter systems of interest. Optical lattices are thus a very powerful tool in the context of quantum simulation due to the wide variety of tunable potential landscapes which can be synthesized.

The combination of strongly isolated, tunably-interacting quantum particles and flexible synthesis of optical potentials makes our experimental apparatus quite advantageous for quantum simulation.

2.5 Periodically driven quantum gases

An additional axis of control over our ultracold atoms is achieved through the introduction of periodic driving. Specifically, we can cyclically modulate one or more parameters in the governing Hamiltonian in time to access new physical regimes, to which the ^{7}Li machine is particularly well-suited. Our dual optical lattices with tunable relative spatial phase shift, independently-programmable modulation parameters, and arbitrary modulation waveforms have enabled an abundance of scientific exploration [10–17]. Periodic driving greatly enhances the capabilities of our apparatus in the realm of quantum simulation.

While classical intuition might suggest that driven quantum systems heat continuously and have unbounded energy growth, this is not always the case in the quantum realm. In fact, questions of how and when driven quantum systems thermalize and how exactly they transition to ergodicity are topics of great interest in the broader scientific

community, and our group has performed investigations along these lines in [14–16]. For the work presented in this thesis, periodic driving in two very different frequency regimes enables explorations into quantum-enhanced thermodynamic processes and steps toward realization of trapped quantum sensors.

In the regime of slow driving, cyclic variation of parameters in the Hamiltonian for a harmonically trapped, interacting BEC creates an isentropic, adiabatic cycle. The harmonic trap is compressed and relaxed, and we exploit the tunable nature of interactions in ^{7}Li to enhance and suppress interparticle scattering. By interleaving strokes of trap compression/relaxation and enhancement/suppression of interactions, we create a thermodynamic cycle. Due to the Bose-enhanced density of a condensate, interaction effects contribute significantly to its internal energy, making its energy evolution distinctly different than that of a classical gas over the course of the cycle.

In the regime of fast driving, we can perform Floquet band engineering where we amplitude-modulate an optical lattice periodically in time. The energy associated with the modulation frequency creates degeneracies between static bands wherever they differ by an integer multiple of this drive energy. The result is that portions of different static bands are effectively "stitched" together and a hybrid band structure results, with character inherited from multiple static bands. These hybrid bands are known as Floquet bands, and they have modified dispersion relations and thus dictate entirely different position-space trajectories than their static band counterparts. Further, the frequency and strength of the amplitude modulation can be set almost arbitrarily, allowing us to "pick and choose" different portions of different static bands to create a Floquet band structure which has desirable dispersion, and thus transport, properties.

Further, by Feshbach-tuning interactions to $0a_0$, we can eliminate interaction-induced decoherence. In chapter 7, we use the power of Floquet band engineering to propose a scheme for a noise-robust continuously-trapped atom interferometer, where the narrow

momentum width of a condensate makes it ideal for quantum sensing.

Chapter 3

Trapping, cooling and manipulating quantum gases

In this chapter, we first give an overview of our ultracold ^{7}Li experimental apparatus and then describe the slowing, cooling and trapping techniques used to achieve Bose-Einstein condensation. The design and construction of the machine are detailed in [6, 7, 18–20].

3.1 Experimental apparatus overview

Our ^{7}Li BEC machine, shown in Figure 3.1, lives on a 4-foot by 10-foot optical table and is made almost entirely out of 304 and 316 stainless steel. This entire apparatus is kept under high to ultra-high vacuum, depending on the section, using ion pumps which operate continuously and a titanium sublimation pump which we fire a handful of times each year. The oven section pressure is $\sim 10^{-9}$ Torr, reduced to $\sim 10^{-10}$ Torr after the first differential pumping tube, and reaches $\sim 10^{-12}$ Torr in the main chamber which is where we create BECs and conduct experiments.

All of our atoms begin life in the oven section where a hot atomic vapor is created

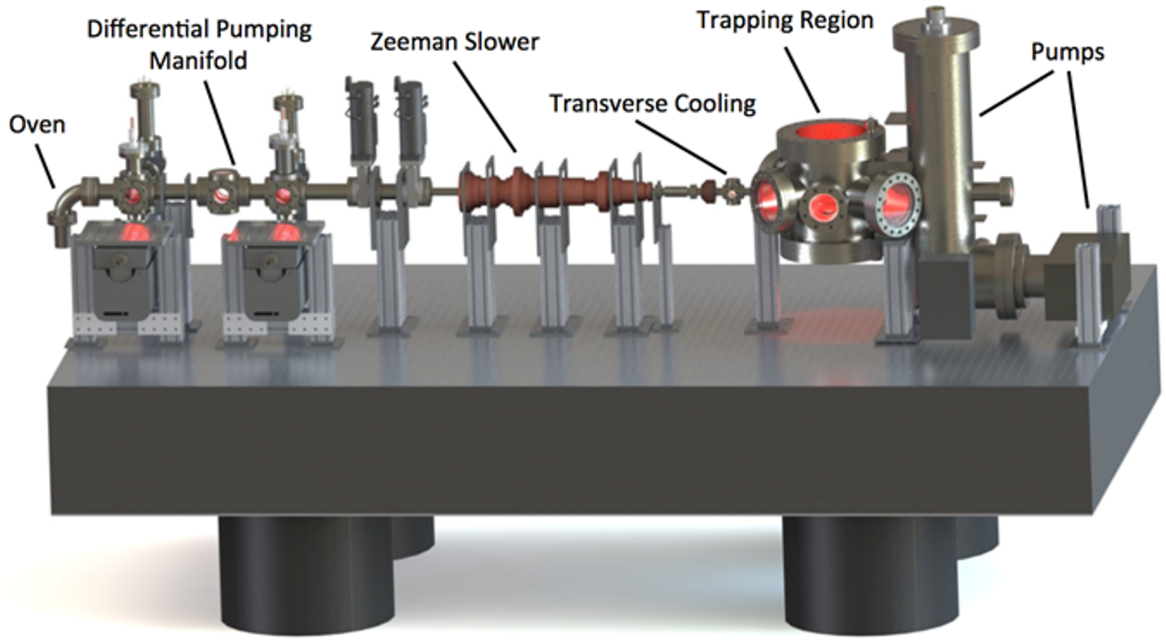

Figure 3.1: CAD diagram of the ^{7}Li BEC apparatus. For orientation, oven is at North end while main chamber and trapping region are at South end. Reproduced from [21].

by heating solid ^{7}Li to 820 K (550° C). These hot atoms then pass through a nozzle, described further in section 3.2.1 and in [22], which acts to collimate the vapor, creating a "beam" of atoms. This beam then passes through a cold plate which blocks atoms with larger divergence angles then through a differential pumping tube (DPT). The DPT has a small aperture which, as the name suggests, maintains a pressure difference between the oven and post-DPT sections, allowing us to reach a lower pressure post-DPT. The atomic beam then enters a six-way cube where the first stage of transverse cooling, described in section 3.2.2, takes place and helps to maintain collimation of the atomic beam. Both the oven and transverse cooling sections have their own ion pumps.

After passing through a second DPT and two gate valves (one for redundancy), the atoms enter the Zeeman slower section which accounts for a significant portion of the length of the machine. Described further in section 3.2.3, atoms are slowed as they traverse the Zeeman slower section by the combination of red-detuned resonant light and

a spatially-varying magnetic field. Atoms entering the slower with velocities $v \leq 1$ km/s exit the slower traveling at about 50 m/s, at which point they encounter a second stage of transverse cooling (see section 3.2.4) and then enter the main chamber, whey they are captured in a magneto-optical trap (section 3.2.5).

3.2 Cooling to quantum degeneracy

This section serves as an overview of the techniques we use to achieve Bose-Einstein condensation. Further discussion can be found in [6, 7, 18–21].

3.2.1 Generating a collimated atomic beam

Following the generation of lithium vapor around 820 K in the oven section, the velocity components transverse to the axis of the machine are reduced using a nozzle, described in [22], which contains a triangular array of microcapillary tubes. The aspect ratio of each microcapillary tube ensures that the majority of the atoms able to pass through emerge with velocity predominantly along the machine axis. Specifically, collisions with the walls of the microcapillaries redistribute the velocity components of atoms with significant transverse velocities, and in this way the array of microcapillaries generates a collimated beam of atoms. After the nozzle, a cold plate attached to a feedthrough blocks atoms which have spread since exiting the nozzle, further aiding to keep the atomic beam collimated. A collimated atomic beam is important, as the length of the machine, roughly eight feet, means that small transverse velocities can lead to a significant portion of the beam not making it to the magneto-optical trap. This reduced atomic beam flux requires longer load times and negatively impacts the cyclic rate of the machine.

After emerging from the oven and passing through the nozzle, both the $F = 1$ and

$F = 2$ hyperfine states are populated. The relative abundance of each state can be estimated using their respective Boltzmann factors and the known ground state hyperfine splitting of 803.5 MHz:

$$\frac{N_{F=2}}{N_{F=1}} = \frac{e^{-E_{F=2}/k_BT}}{e^{-E_{F=1}/k_BT}} = \exp\left(-\frac{\Delta E}{k_BT}\right) \approx 0.999952974. \tag{3.1}$$

So, for a temperature of 820 K (the temperature of the nozzle), we can treat the distribution among ground states as being equal.

3.2.2 Transverse cooling

After passing through the six-way cube containing the cold plate, the atomic beam enters another cube where the first stage of transverse cooling takes place. Red-detuned 671 nm light enters the cube from the West and top view ports, and retro-reflecting mirrors on the East and bottom sides ensure that all transverse velocity directions are addressed. Transverse cooling works to maintain collimation of the atomic beam. For atoms with velocity components transverse to the slower axis, the Doppler shift brings the transverse cooling light into resonance with these atoms which results in absorption and subsequent spontaneous emission of a photon. Because the transverse cooling light points along a particular direction while the spontaneously emitted photon is emitted in a random direction, the result is that, on average, atoms experience a momentum "kick" $\hbar k$ in the direction opposite to their motion. This results in the slowing and cooling of the transverse velocity components of the atomic beam.

3.2.3 Zeeman slower

The length of the machine is dominated by the Zeeman slower section whose purpose is to slow the atoms from an initial velocity of ∼1 km/s to 50 m/s at the entrance of

the main chamber. Similar to the transverse cooling beams, the Zeeman slower beam is red-detuned from resonance so that the Doppler shift brings this light into resonance with fast-moving atoms. Without the Zeeman slower section and with a fixed detuning for the slower beam, atoms would scatter photons until they were effectively no longer addressed by the detuned slower beam and the slowing process would terminate. To compensate for this, the Zeeman slower uses windings of electromagnet coils to create a spatially-varying magnetic field profile which shifts the atomic energy levels via the Zeeman effect, which brings the slower beam back into resonance with the primary cooling transition. This allows the slowing and cooling process to continue for the length of the slower section. In order to slow atoms from both the $F = 1$ and $F = 2$ ground state manifolds, the Zeeman slower beam passes through an 813.5 MHz electro-optic modulator before entering the vacuum chamber.

3.2.4 More transverse cooling

After exiting the Zeeman slower but before entering the main chamber, it is important to perform a second stage of transverse cooling. Unlike the first stage, whose purpose is to aid in maintaining a collimated atomic beam, the second stage is used to prevent "beam bloom" before the atoms enter the main chamber. As the transverse velocity components of the slowed atomic beam are now comparable to the axial component, the beam will expand outwards unless subjected to additional transverse cooling. Compared to TC1, the detunings for TC2 are smaller as the atoms are moving much more slowly when they emerge from the Zeeman slower. This second stage of transverse cooling is implemented with a 1.33" cube and a red-detuned beam in a bow-tie configuration.

3.2.5 Magneto-optical trap

The slowed atomic beam then enters the main chamber where atoms are captured in a magneto-optical trap (MOT). Four pairs of circularly-polarized counter-propagating laser beams enter the main chamber where a quadrupolar magnetic field is created by large electromagnets in an anti-Helmholtz configuration. Each pair of counter-propagating MOT beams creates an optical molasses along that axis which slows the atoms. The presence of a field gradient ($\sim$20 G/cm) gives rise to a spatially-varying Zeeman shift, so as atoms move away from the field zero, the Zeeman shift brings the cooling transition into resonance with the MOT light. At resonance, the atoms receive a kick back towards the field zero from the absorbed photon and in this way remain trapped. The combination of optical molasses along each axis and a spatially-varying Zeeman shift creates a magneto-optical trap, where the former acts as a drag force to slow and cool atoms while the latter acts as a restoring force to bring atoms back towards the trap center.

3.2.6 Gray molasses

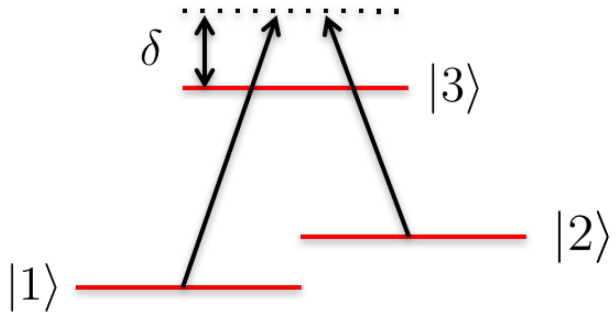

Figure 3.2: A two-photon Λ-type Raman transition level structure. Reproduced from [6].

After the compressed MOT, we perform sub-Doppler laser cooling via Λ-enhanced gray molasses, a technique described in [23,24] which operates using a Λ-type two-photon

Raman transition. While it's possible to increase phase-space density without this technique, it is much more challenging from a technical standpoint as it requires UV light and optics. The gray molasses cooling method operates on the D_1 line where, unlike the D_2 line, the excited hyperfine states are resolved (see Figure 2.1).

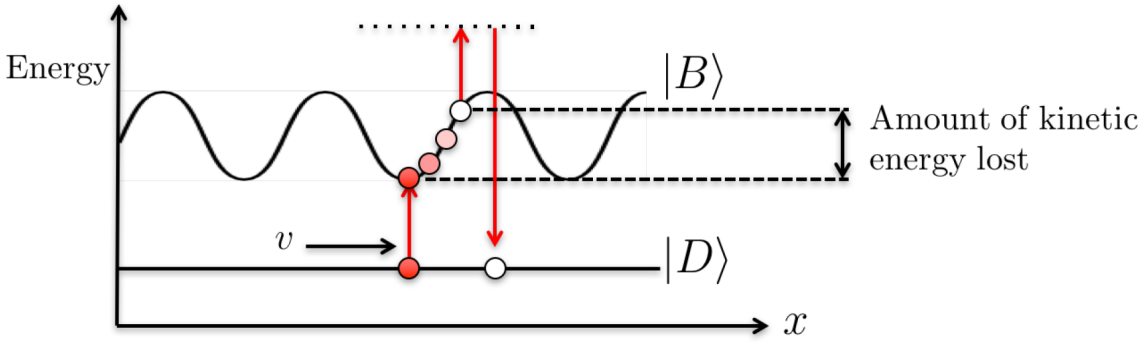

Figure 3.3: Schematic of gray molasses. Reproduced from [6].

To perform gray molasses, we create a three-dimensional standing wave of laser light which creates a spatially-periodic AC Stark shift. To understand the cooling process, it is useful to think of the system in the dressed-state picture in which we can construct states which are superpositions of the $F = 1$ and $F = 2$ ground states. These superposition states are referred to as "bright" and "dark", where the former couples to the optical field while the latter does not. We denote these by $|B\rangle$ and $|D\rangle$, respectively, with the excited state denoted by $|E\rangle$. The cooling process then proceeds as follows, and is shown schematically in Figure 3.3:

1. An atom in state $|B\rangle$ at a potential minimum "climbs" the potential over time due to the evolution caused by the atom-light interaction. Conservation of energy requires that the atom lose kinetic energy as it moves up the potential.

2. Once it has reached a potential maximum, the atom simultaneously undergoes an electric dipole transition to $|E\rangle$ and stimulated emission down to $|D\rangle$ due to the

laser field. This is the two-photon part of this scheme.

3. Once in $|D\rangle$, the atom is optically dark. However, $|D\rangle$ is not an eigenstate of the kinetic energy operator, so an atom in $|D\rangle$ evolves back into $|B\rangle$ over time at rate proportional to its momentum. The result is that atoms with larger momenta evolve back into $|B\rangle$ more rapidly and undergo this cooling process repeatedly, losing energy each time. Eventually, the kinetic energy of each atom reaches a point where it is insufficient to climb the potential and undergo further cooling.

This sub-Doppler cooling process results in a cloud with a temperature of about 50 μK.

3.2.7 D_1 optical pumping

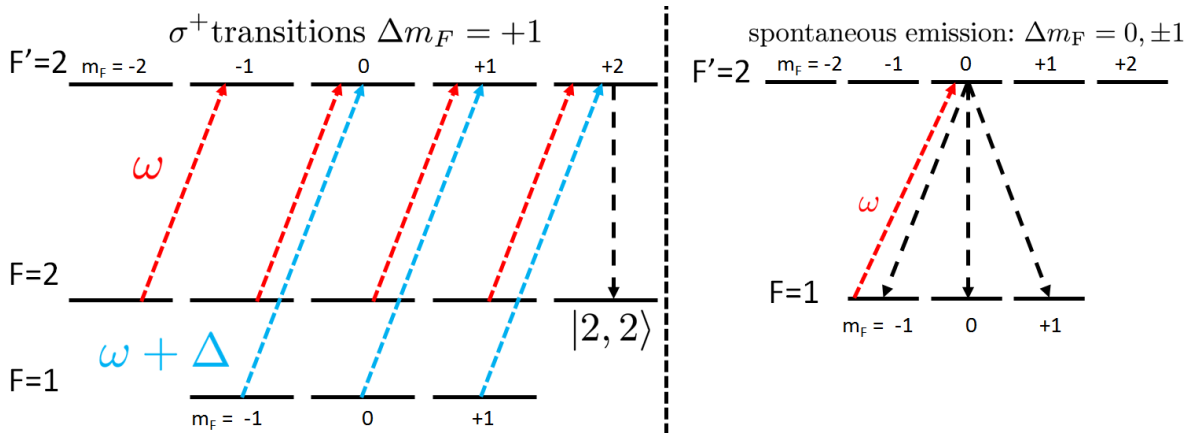

Figure 3.4: D_1 optical pumping scheme in ^{7}Li. Light resonant with both hyperfine ground states is σ^+-polarized to enforce $\Delta m_F = +1$ and drive transitions to the $F' = 2$ excited hyperfine state manifold. Once in the excited hyperfine state manifold, atoms undergo spontaneous emission events resulting in $\Delta m_F = 0, \pm 1$, but the σ^+-polarized light has the net effect of driving population into the $|2, 2\rangle$ stretched state over repeated absorption events, where atoms cannot undergo any further transitions and become optically dark. The detuning $\Delta = 803.5$ MHz, corresponding to the zero-field hyperfine splitting between $F = 1$ and $F = 2$ ground states. Figure reproduced from [7].

In preparation for the magnetic trap, we spin-polarize the ensemble of atoms by

shining σ^+-polarized D_1 light in the presence of a weak DC magnetic bias field to create a quantization axis. Before reaching the atoms, the D_1 light passes through an 803.5 MHz EOM which adds frequency-shifted sidebands so that both hyperfine ground states are addressed. This process drives transitions from both the $F = 1$ and $F = 2$ ground states to the $F' = 2$ excited state, and the light's circular polarization enforces the selection rule $\Delta m_F = +1$. Over the course of repeated absorption and spontaneous emission events, this drives atoms into the stretched state $|F = 2, m_F = +2\rangle$ of the $F = 2$ ground state hyperfine manifold. Once in this state, atoms can no longer scatter σ^+ light, so scattering is self-terminating. Figure 3.4 shows a diagram of this process.

3.2.8 Magnetic trap and RF evaporation

After optical pumping, the strength of the quadrupolar magnetic field is ramped to its maximum value, achieved by sending 500 A to both the inner and outer sets of coils; this results in a field gradient of ∼420 G/cm. Depending on the particular hyperfine sublevel, an atom will either be trapped or anti-trapped by the field gradient, as the spatially-varying Zeeman shift will create either a potential minimum or maximum, respectively, at the field zero. For this reason, and to avoid losses from interspin collisions, it is critical to spin-polarize the sample using optical pumping to maximize the number of atoms in the $|2, 2\rangle$ state which is trapped by the field gradient.

Our magnetic trap requires the use of an intense (∼15 W), blue-detuned laser beam focused tightly at the magnetic field zero, referred to as the "plug" beam. Without it, atoms in the $|2, 2\rangle$ state which have accumulated in the trap pass through the field zero, at which position there is no quantization axis. This allows the spins to precess freely, and once an atom has passed through the field zero and again has a quantization axis, it will likely be in a different spin state. Crucially, if it ends up in an anti-trapped state,

it will be lost from the magnetic trap. The plug beam remedies this problem as its high intensity and blue detuning from resonance create a strong, repulsive barrier at the field zero which repels atoms and largely prevents these so-called Majorana losses.

With the magnetic trap plugged and the atoms spin-polarized, we can now perform forced evaporative cooling by sweeping the frequency of an RF source from 927 MHz to 805 MHz. This so-called "RF knife" drives transitions from the trapped $|2,2\rangle$ state to the anti-trapped $|1,1\rangle$, and the net result is that the hottest atoms located at higher potential energies get ejected from the magnetic trap. By sweeping the RF, we lose a significant number of atoms but those which remain rethermalize to a lower temperature, somewhere around 10 μK.

3.2.9 Optical evaporation

After forced evaporation from the magnetic trap, atoms are loaded into a far-detuned 1064 nm crossed optical dipole trap (ODT) by increasing the 1064 nm optical power from zero to 15-20 W in each dipole beam. The ODT is loaded away from the plug beam and center of the cloud to avoid capturing atoms which have excess potential energy from their proximity to the plug beam. In parallel, we ramp the strength of the quadrupolar field down to zero. With atoms now loaded in the dipole trap, we apply a small DC magnetic bias field to lift the degeneracy between m_F sublevels and perform rapid adiabatic passage by sweeping the RF frequency from 809.6 MHz to 807.5 MHz in 60 ms. This process transfers atoms from $|2,2\rangle$ to $|1,1\rangle$, which is critical as the former state has an attractive background scattering length of $-24.5a_0$ which would make any BEC formation unstable due to three-body recombination. Additionally, the $|2,2\rangle$ lacks a magnetic Feshbach resonance. However, the $|1,1\rangle$ state has both a favorable background scattering length of $7.7a_0$ as well as an accessible Feshbach resonance.

Once in $|1,1\rangle$, we Feshbach-tune the scattering length to $240a_0$ to facilitate rapid thermalization, which is relevant as we are about to perform further evaporative cooling. We perform optical evaporation by ramping down the optical power in the dipole beams with a functional form exponential in time, resulting in relaxation of the trapping potential. The result is that the hottest atoms, which are furthest up the optical potential, escape as the trap depth decreases. At the same time, the remaining atoms rethermalize to a lower temperature, and this occurs throughout the ramp. As more atoms escape from the trap, those which remain become colder and more dense, until eventually the phase-space density reaches order unity and Bose-Einstein condensation occurs.

3.3 Absorption imaging

For all of the experiments performed on the machine so far, the readout of data is accomplished through absorption imaging, in which a beam of resonant light is shot through the cloud. To properly reconstruct the density distribution of the cloud, three images must be taken. The first is the image obtained when shining imaging (i.e. resonant) light onto the camera with the atoms present; this is known as the "probe with atoms" or PWA image. Secondly, an image is taken after the atoms have been blown away by the imaging beam and are no longer on the camera sensor; this is known as the "probe without atoms", or PWOA, image. Lastly, a dark image is taken without atoms or imaging light, unintuitively called the "dark image". Denoting the set of these images as $\{I_i\}$, we can obtain the desired normalized optical density profile:

$$\mathrm{OD}(x,y) = \ln\left(\frac{I_{\mathrm{PWOA}} - I_{\mathrm{dark}}}{I_{\mathrm{PWA}} - I_{\mathrm{dark}}}\right) \tag{3.2}$$

From here, the actual density distribution can be obtained using

$$n(x,y) = \frac{A_{\text{px}}^2}{\sigma_0^{\text{eff}}}\ \text{OD}(x,y) \tag{3.3}$$

where A_{px} is the conversion between camera pixels and microns and σ_0^{eff} is the effective scattering cross-section. For the entirety of our experiments so far, we have assumed $\sigma_0^{\text{eff}} = (1/3)\sigma_0^{\text{res}}$ where σ_0^{res} is the resonant scattering cross-section. The factor of $1/3$ is a result of the atomic electric dipole moments having random orientations. From the density distribution, we can integrate to find the total atom number N:

$$N = \iint dx\ dy\ n(x,y), \tag{3.4}$$

or

$$N = \iint dx\ dy\ \frac{A_{\text{px}}^2}{\sigma_0^{\text{eff}}}\ \text{OD}(x,y). \tag{3.5}$$

Chapter 4

Bose-Einstein condensate physics

Following our discussions of Bose-Einstein condensation and imaging, this chapter reviews some key properties of BECs which we utilize in chapters 6 and 7.

4.1 Introduction

Quantum degenerate gases, in the form of Bose-Einstein condensates (BECs), serve as the starting point for all of our experiments. In this regime, a macroscopic number of particles occupy the ground state of the trap, giving rise to a "giant" matter wave. Thus, the dynamics of an individual particle are amplified by the total number of condensed particles which makes their behavior easier to study. This chapter aims to cover some key properties of BECs as well as some of their relevant behavior in optical traps. The next chapter will focus on condensates in optical lattices and the resulting dynamics.

4.2 The Gross-Pitaevskii equation and Thomas-Fermi approximation

This chapter closely follows the treatment in *Bose-Einstein Condensation* by Pitaevskii and Stringari [2] and *Bose-Einstein Condensation in Dilute Gases* by Pethick and Smith [3]. The time-dependent Gross-Pitaevskii equation (GPE) is given by [2]

$$i\hbar\partial_t\Psi(\mathbf{r},t) = \left(-\frac{\hbar^2\nabla^2}{2m} + V_{\text{ext}}(\mathbf{r},t) + g|\Psi(\mathbf{r},t)|^2\right)\Psi(\mathbf{r},t), \tag{4.1}$$

where $\Psi(\mathbf{r},t)$ is the wave function describing the condensate, g is the interaction coupling constant given by $g = 4\pi\hbar^2 a_s/m$ where a_s is the s-wave scattering length and $V_{\text{ext}}(\mathbf{r},t)$ is an external potential, often a harmonic trap. Note that 4.1 reduces to the standard time-dependent Schrödinger equation (TDSE) for non-interacting bosons where $a_s = 0a_0$, with a_0 the Bohr radius. The non-linear term $g|\Psi(\mathbf{r},t)|^2$ represents the so-called mean-field approximation, where the otherwise intractable problem of treating all pairwise boson-boson interactions is instead replaced by each boson interacting with an effective "field" of strength $g|\Psi(\mathbf{r},t)|^2$. As discussed in section 2.2, the strength of interparticle scattering between ^{7}Li atoms can be tuned with an applied DC magnetic field, so by extension the coupling strength g is also tunable. The scattering length a_s can be set anywhere between infinitely repulsive and infinitely attractive, including the point where atoms are "non-interacting" in the sense that the s-wave scattering length vanishes.

The time-independent Gross-Pitaevskii equation is given by

$$\mu\Psi(\mathbf{r}) = \left(-\frac{\hbar^2\nabla^2}{2m} + V_{\text{ext}}(\mathbf{r}) + g|\Psi(\mathbf{r})|^2\right)\Psi(\mathbf{r}) \tag{4.2}$$

Multiplying both sides by $\Psi^*(\mathbf{r})$ and integrating over space gives [2]

$$\mu \int d\mathbf{r}\ |\Psi(\mathbf{r})|^2 = N\mu = \frac{\hbar^2}{2m}\int d\mathbf{r}\ |\nabla\Psi(\mathbf{r})|^2 + \int d\mathbf{r}\ V_{\text{ext}}(\mathbf{r})|\Psi(\mathbf{r})|^2 + \frac{g}{2}\int d\mathbf{r}\ |\Psi(\mathbf{r})|^4, \quad (4.3)$$

and we can identify the following quantities:

$$\begin{aligned} E_{\text{kin}} &= \frac{\hbar^2}{2m}\int d\mathbf{r}\ |\nabla\Psi(\mathbf{r})|^2 \\ E_{\text{pot}} &= \int d\mathbf{r}\ V_{\text{ext}}(\mathbf{r})|\Psi(\mathbf{r})|^2 \\ E_{\text{int}} &= \frac{g}{2}\int d\mathbf{r}\ |\Psi(\mathbf{r})|^4, \end{aligned} \quad (4.4)$$

where we have used the normalization condition

$$\int d\mathbf{r}\ |\Psi(\mathbf{r})|^2 = N, \quad (4.5)$$

where N is the total number of atoms in the condensate. Inserting these into 4.2 then gives the following relation:

$$\mu = \frac{1}{N}\left(E_{\text{kin}} + E_{\text{pot}} + 2E_{\text{int}}\right) \quad (4.6)$$

In the Thomas-Fermi limit, kinetic energy is neglected and the time-independent GPE reduces to

$$\mu_{\text{TF}}\Psi_{\text{TF}}(\mathbf{r}) = \left[V_{\text{ext}}(\mathbf{r}) + g|\Psi_{\text{TF}}(\mathbf{r})|^2\right]\Psi_{\text{TF}}(\mathbf{r}) \quad (4.7)$$

where μ_{TF} and $\Psi_{\text{TF}}(\mathbf{r})$ are the chemical potential and wave function in the Thomas-Fermi limit, respectively, and it follows that

$$\mu_{\mathrm{TF}} = V_{\mathrm{ext}}(\mathbf{r}) + g|\Psi_{\mathrm{TF}}(\mathbf{r})|^2, \tag{4.8}$$

so

$$|\Psi_{\mathrm{TF}}(\mathbf{r})|^2 = n(\mathbf{r}) = \max\left(\frac{\mu_{\mathrm{TF}} - V_{\mathrm{ext}}(\mathbf{r})}{g}, 0\right), \tag{4.9}$$

and

$$|\Psi_{\mathrm{TF}}(\mathbf{r})| = \max\left(\sqrt{\frac{\mu_{\mathrm{TF}} - V_{\mathrm{ext}}(\mathbf{r})}{g}}, 0\right). \tag{4.10}$$

Here, we have identified $|\Psi_{\mathrm{TF}}(\mathbf{r})|^2$ as the density distribution $n(\mathbf{r})$, and it follows that for a generic 3D anisotropic harmonic potential, the form of the density distribution is that of an inverted paraboloid. Additionally, $|\Psi_{\mathrm{TF}}(\mathbf{r})|$ gives the wave function up to a phase factor. It is important to note that, when fitting a Thomas-Fermi profile to experimental data, one needs to use an integrated Thomas-Fermi distribution. For example, when fitting a distribution to an optical density profile which has been integrated along one direction, it is appropriate to use a twice-integrated Thomas-Fermi wave function before squaring to find the density distribution. The first integral accounts for the fact that absorption imaging acts as a column integration along z while the second integral corresponds to integration of the optical density $\mathrm{OD}(x, y)$ over either x or y. The chemical potential μ_{TF} can be found by imposing the normalization condition $\int d^3\mathbf{r}\ n(\mathbf{r}) = N$:

$$\int d^3\mathbf{r}\ n(\mathbf{r}) = \int d^3\mathbf{r}\ |\Psi_{\mathrm{TF}}(\mathbf{r})|^2 = \frac{1}{g}\int d^3\mathbf{r}\ (\mu_{\mathrm{TF}} - V_{\mathrm{ext}}(\mathbf{r})) \tag{4.11}$$

$$\mu_{\mathrm{TF}} = \frac{\hbar\bar{\omega}}{2}\left(\frac{15Na}{a_{\mathrm{HO}}}\right)^{2/5} \tag{4.12}$$

where $\bar{\omega} = (\omega_x\omega_y\omega_z)^{1/3}$ is the geometric mean trap frequency and $a_{\mathrm{HO}} = \sqrt{\frac{\hbar}{m\bar{\omega}}}$ is the

harmonic oscillator length associated with trap frequency $\bar{\omega}$.

Using this result, the total energy per particle in the Thomas-Fermi limit is given by [3]

$$\frac{E_{\mathrm{TF}}}{N} = \frac{5}{7}\mu_{\mathrm{TF}} \tag{4.13}$$

The extent of the cloud along each principle axis can be found looking at the classical turning points along each axis, i.e. where the chemical and harmonic potentials are equal:

$$\mu_{\mathrm{TF}} = \frac{1}{2}m\omega_i^2 R_{\mathrm{TF},i}^2, \tag{4.14}$$

where $R_{\mathrm{TF},i}$ is known as the Thomas-Fermi radius along the i^{th} direction. It follows that the Thomas-Fermi radii are given by

$$R_{\mathrm{TF},i} = \sqrt{\frac{2\mu_{\mathrm{TF}}}{m\omega_i^2}}. \tag{4.15}$$

The Thomas-Fermi limit refers to a regime in which the kinetic energy of the cloud is negligible, i.e. $E_{\mathrm{kin}} \approx 0$, so $E_{\mathrm{tot}} = E_{\mathrm{kin}} + E_{\mathrm{pot}} + E_{\mathrm{int}} \approx E_{\mathrm{pot}} + E_{\mathrm{int}}$. In the Thomas-Fermi limit, the chemical potential is given by 4.12, and we can see that there is a dependence on both scattering length and trap frequency.

Another useful result which can be derived from the time-independent Gross-Pitaevskii equation 4.2 is the virial relation [2]

$$2E_{\mathrm{kin}} + 3E_{\mathrm{int}} - 2E_{\mathrm{pot}} = 0, \tag{4.16}$$

which, in the Thomas-Fermi limit where $E_{\mathrm{kin}} \approx 0$, can be used to measure E_{int} and thus E_{pot}. Specifically, performing a sufficiently long time of flight results in the conversion of interaction to kinetic energy, so a measurement of E_{kin} after TOF actually gives E_{int}, from

which we calculate $E_{\rm pot} = (3/2)E_{\rm int}$. In the coming sections, we will also be interested in the release energy of the cloud, given by $E_{\rm rel} = E_{\rm kin} + E_{\rm int}$ in the Thomas-Fermi limit.

4.3 Finite-temperature analytics

The Gross-Pitaevskii equation and the Thomas-Fermi approximation are valid at zero temperature, which of course is not yet achievable in the laboratory. However, below the critical temperature T_c^0 for bosons in a harmonic trap, finite-temperature effects can be incorporated into the expressions for entropy and each contribution to the total energy [2]:

$$\frac{E_{\rm tot}}{Nk_BT_c^0} = 3\frac{\zeta(4)}{\zeta(3)}t^4 + \frac{1}{7}\eta(1-t^3)^{2/5}(5+16t^3), \tag{4.17}$$

$$\frac{E_{\rm kin}}{Nk_BT_c^0} = \frac{3\zeta(4)}{2\zeta(3)}t^4 + \frac{1}{7}\eta(1-t^3)^{2/5}\left(\frac{17}{2}t^3\right) \tag{4.18}$$

$$\frac{E_{\rm pot}}{Nk_BT_c^0} = \frac{3\zeta(4)}{2\zeta(3)}t^4 + \frac{1}{7}\eta(1-t^3)^{2/5}(3+\frac{15}{2}t^3) \tag{4.19}$$

$$\frac{E_{\rm int}}{Nk_BT_c^0} = \frac{2}{7}\eta(1-t^3)^{2/5}, \tag{4.20}$$

where

$$\eta = \frac{\mu(T=0)}{k_BT_c^0} = \frac{15^{2/5}[\zeta(3)]^{1/3}}{2}\left(N^{1/6}\frac{a}{a_{\rm HO}}\right)^{2/5}, \tag{4.21}$$

$t = T/T_c^0$ is the reduced temperature and T_c^0 is given by

$$T_c^0 = \frac{\hbar\bar{\omega}}{k_B}\left(\frac{N}{\zeta(3)}\right)^{1/3}, \tag{4.22}$$

which is the critical temperature for a non-interacting Bose gas in a harmonic trap with geometric mean trap frequency $\bar{\omega} = (\omega_x \omega_y \omega_z)^{1/3}$. Corrections to T_c^0 accounting for finite-size and interaction effects are given, respectively, by [25]

$$\frac{\delta T_c^0}{T_c^0} = -\frac{\zeta(2)}{2\zeta(3)^{2/3}} \frac{\omega_{\text{mean}}}{\bar{\omega}} N^{-1/3} \tag{4.23}$$

and

$$\frac{\delta T_c^{\text{int}}}{T_c^0} = -1.33 \frac{a}{a_{\text{HO}}} N^{1/6}, \tag{4.24}$$

where $\omega_{\text{mean}} = (\omega_x + \omega_y + \omega_z)/3$. The condensed fraction f_c is also modified by the presence of interparticle interactions through the parameter η:

$$\frac{N_0}{N} = f_c = 1 - t^3 - \frac{\zeta(2)}{\zeta(3)} \eta t^2 \left(1 - t^3\right)^{2/5}. \tag{4.25}$$

Another quantity of interest is the entropy of the gas at finite temperature:

$$\frac{S}{N k_B} = 4 \frac{\zeta(4)}{\zeta(3)} t^3 + 3\eta t^2 \left(1 - t^3\right)^{2/5}. \tag{4.26}$$

A quantity which we make use of in chapter 6 is the energy of the cloud once the harmonic trap has been snapped off, which known as the release energy E_{rel} and only contains contributions from kinetic and interaction components:

$$\frac{E_{\text{rel}}}{N k_B T_c^0} = \frac{E_{\text{kin}} + E_{\text{int}}}{N k_B T_c^0} = \frac{3\zeta(4)}{2\zeta(3)} t^4 + \frac{1}{7} \eta (1 - t^3)^{2/5} (2 + \frac{17}{2} t^3). \tag{4.27}$$

An important note is that these equations account for both the condensate and thermal clouds, while results derived from the Gross-Pitaevskii equation only treat the former.

4.4 Thermometry

A pure BEC, something which can only be achieved at absolute zero, does not have a temperature as the temperature of a condensate is defined by the thermal atoms with which it is in contact. At zero temperature, the condensed fraction is unity so there are no thermal atoms with which one can define a temperature. Since we cannot create a pure BEC, it is of great importance to calculate the temperature of the thermal atoms, and thus the condensate, using experimental measurements. Bosonic statistics, which are responsible for the macroscopic occupation of the ground state, give rise to the characteristic Thomas-Fermi profile of a condensate. In contrast, the remaining thermal atoms obey a Boltzmann, i.e. Gaussian, distribution. In order to accurately describe the system, one must account for both of these distributions with a bimodal distribution. This is simply the sum of a Thomas-Fermi profile, which captures the behavior of the condensate within the Thomas-Fermi radius, and a Gaussian distribution which captures the behavior of thermal atoms outside the Thomas-Fermi radius, which are the so-called "thermal wings".

To extract the temperature of the condensate using the thermal wings, one needs to first perform an experimental sequence varying time of flight. The goal is to fit the thermal wings at each value of TOF and extract the thermal cloud size σ^{th}. Then, fitting a square root function to a plot of σ^{th} versus t_{TOF} allows the temperature to be calculated [26]:

$$\sigma^{\text{th}}(t) = \sqrt{\left(\sigma_0^{\text{th}}\right)^2 + \left(\frac{k_B T}{m}\right) t_{\text{TOF}}^2} \tag{4.28}$$

where σ_0^{th} is the cloud size at $t_{\text{TOF}} = 0$. Expansion of the condensate over time, i.e. Thomas-Fermi radius versus TOF, does not give the temperature as it does not determine the shape of the BEC profile or the expansion dynamics, which can be seen from equation 4.9 for the density $n(\mathbf{r})$ in the Thomas-Fermi limit. Instead, the profile of the condensate

and its expansion dynamics are solely determined by the trap parameters and interaction strength.

To fit a bimodal distribution to the optical density profile obtained from an absorption image, it is important to be able to consistently discriminate between condensate and thermal wings. One approach we have tried, as described in [27], uses a three-step method to fit the thermal wings. This procedure applies to the 1D profiles obtained by summing the optical density $\mathrm{OD}(x, y)$ over either x or y. First, a Thomas-Fermi profile is fit to the entire distribution, which will naturally result in some broadening due to the thermal wings. To correct for this, a scale factor $s \leq 1$ is used to identify the region which is condensate. In [27], they found that a scale factor of about 0.85 gives accurate results, and from the fit testing we have done, we can confirm their findings. So, from the Thomas-Fermi radius R_{TF} found in the first step, the region $-sR_{\mathrm{TF}} \leq x \leq sR_{\mathrm{TF}}$ is taken to be condensate and is masked off, meaning the data in that range is not used for subsequent fitting. For appropriate values of s, this results in only the thermal wings remaining, and one can then fit a Gaussian to find the cloud size. The multi-step process must be done for each image in a TOF sequence to extract the temperature.

Another useful metric which can be calculated using bimodal fitting is the condensate fraction f_c. After fitting a bimodal distribution to a summed OD, one can simply divide the integral of the Thomas-Fermi profile by the integral of the entire bimodal distribution to obtain f_c. It is best to perform the fitting at long TOFs so that the thermal wings have sufficient time to expand and become distinct from the BEC. In principle, condensate fraction can be used to estimate temperature, but because $f_c = 1 - t^3 - \frac{\zeta(2)}{\zeta(3)} \eta t^2 \left(1 - t^3\right)^{2/5}$, back-calculating temperature comes with large error bars unless f_c is known very precisely.

An alternative method to extract temperature exists, as described in [26]. If the trap frequencies are known, the temperature along the i^{th} axis after time of flight t_{TOF} is given

by

$$k_B T = \frac{1}{2} m \left(\frac{\omega_i^2}{1 + \omega_i^2 t_{\mathrm{TOF}}^2} \right) \left(\sigma_i^{\mathrm{th}} \right)^2, \tag{4.29}$$

where ω_i is the trap frequency along that axis and σ_i^{th} is the thermal cloud size at time t_{TOF}. As an aside, an interesting point noted in [26] is that one should really perform bimodal fitting using the sum of a Bose-enhanced distribution, rather than a Gaussian distribution, and a Thomas-Fermi profile. The Bose-enhanced density distribution of the thermal cloud is obtained by first writing the Bose-Einstein distribution function for harmonically trapped particles [2]:

$$n_{\boldsymbol{p}}(\boldsymbol{r}) = \frac{1}{\exp[\beta(\epsilon(\boldsymbol{r}, \boldsymbol{p}) - \mu)] - 1}, \tag{4.30}$$

where $n_{\mathbf{p}}(\mathbf{r})$ is the momentum-space density distribution, $\epsilon(\mathbf{r}, \mathbf{p}) = p^2/2m + V_{\mathrm{ext}}(\mathbf{r})$ and $\beta = (k_B T)^{-1}$. The thermal density distribution is then found through integration:

$$n_{\mathrm{th}}(\mathbf{r}) = \int \frac{d\mathbf{p}}{(2\pi\hbar)^3} n_{\mathbf{p}}(\mathbf{r}). \tag{4.31}$$

Below T_c^0, the chemical potential $\mu = 0$ and the above integral evaluates to

$$n_{\mathrm{th}}(\mathbf{r}) = \frac{1}{\lambda_T^3} g_{3/2} \left[\exp\left(-\beta V_{\mathrm{ext}}(\mathbf{r}) \right) \right], \tag{4.32}$$

where $\lambda_T = h/\sqrt{2\pi m k_B T}$ is the thermal de Broglie wavelength, and the Bose function $g_p(z)$ is given by

$$g_p(z) = \frac{1}{\Gamma(p)} \int_0^\infty \mathrm{d}x \; x^{p-1} \frac{1}{z^{-1}\mathrm{e}^x - 1} = \sum_{\ell=1}^{\infty} \frac{z^\ell}{\ell^p}. \tag{4.33}$$

Thus, 4.32 is the Bose-enhanced density distribution of the thermal fraction, so when

fitting a bimodal distribution, we can use the form

$$n_{\rm tot}(\mathbf{r}) = n_{\rm th}\; g_{3/2}\left(\prod_{i=1}^{3} e^{-x_i^2/{\sigma_i^{\rm th}}^2}\right) + n_c \max\left(1 - \sum_{i=1}^{3}\frac{x_i^2}{R_{{\rm TF},i}^2}, 0\right), \tag{4.34}$$

where $n_{\rm th}$ and n_c are the thermal and condensed fractions, respectively, $R_{{\rm TF},i}$ is the Thomas-Fermi radius along the $i^{\rm th}$ axis given by 4.15, and $\sigma_i^{\rm th}$ is the thermal cloud size along the $i^{\rm th}$ axis after a time $t_{\rm TOF}$. The set of $\{\sigma_i^{\rm th}\}$ are used as the fitting parameters, and from them the temperature along each axis can be obtained.

Absorption imaging gives us the column-integrated optical density profile $\mathrm{OD}(x, y)$, and we are often interested in fitting the one-dimensional density profiles obtained by integrating along x or y. To find the proper 1D fit function, we must account for both of these integrals. Recall that a Thomas-Fermi distribution in three dimensions is given by equation 4.9

$$n_{\rm TF}(\mathbf{r}) = \max\left(\frac{\mu_{\rm TF} - V_{\rm ext}(\mathbf{r})}{g}, 0\right), \tag{4.35}$$

with a corresponding wave function (up to a phase factor)

$$|\Psi_{\rm TF}(\mathbf{r})| = \max\left(\sqrt{\frac{\mu_{\rm TF} - V_{\rm ext}(\mathbf{r})}{g}}, 0\right). \tag{4.36}$$

For the purposes of fitting, we need to find the one and two-dimensional density distributions $n_{\rm TF}^{\rm 1D}(x)$ and $n_{\rm TF}^{\rm 2D}(x, y)$, respectively. The 2D density distribution is given by

$$\begin{aligned} n_{\rm TF}^{\rm 2D}(x, y) &= \int dz\; \left(\frac{\mu_{\rm TF} - V_{\rm ext}(\mathbf{r})}{g}\right) \\ &= \frac{\mu_{\rm TF}}{g}\int dz\; \left[1 - \left(\frac{V_{\rm ext}(\mathbf{r})}{\mu_{\rm TF}}\right)\right] \\ &= \frac{\mu_{\rm TF}}{g}\int dz\; \left[1 - \frac{m}{2\mu_{\rm TF}}\left(\omega_x^2 x^2 + \omega_y^2 y^2 + \omega_z^2 z^2\right)\right]. \end{aligned} \tag{4.37}$$

Recalling that $R_{\mathrm{TF},i} = \sqrt{2\mu_{\mathrm{TF}}/m\omega_i^2}$, we can rewrite this as

$$n_{\mathrm{TF}}^{\mathrm{2D}}(x,y) = \frac{\mu_{\mathrm{TF}}}{g}\int dz\ \left(1 - \left[\left(\frac{x}{R_{\mathrm{TF},x}}\right)^2 + \left(\frac{y}{R_{\mathrm{TF},y}}\right)^2 + \left(\frac{z}{R_{\mathrm{TF},z}}\right)^2\right]\right). \tag{4.38}$$

Then, defining $\bar{x}_i := x_i/R_{\mathrm{TF},i}$ and noting that $\bar{z}$ is constrained by $\bar{z}^2 = 1 - \bar{x}^2 - \bar{y}^2$, this integral becomes

$$\begin{aligned} n_{\mathrm{TF}}^{\mathrm{2D}}(\bar{x},\bar{y}) &= \frac{\mu_{\mathrm{TF}}}{g}R_{\mathrm{TF},z}\int_{-\sqrt{1-\bar{x}^2-\bar{y}^2}}^{\sqrt{1-\bar{x}^2-\bar{y}^2}} d\bar{z}\ \left(1 - \left[\bar{x}^2 + \bar{y}^2 + \bar{z}^2\right]\right) \\ &= \frac{4}{3}\frac{\mu_{\mathrm{TF}}}{g}R_{\mathrm{TF},z}\left(1 - \bar{x}^2 - \bar{y}^2\right)^{3/2}. \end{aligned} \tag{4.39}$$

Integrating again with respect to $\bar{y}$, we have

$$\begin{aligned} n_{\mathrm{TF}}^{\mathrm{1D}}(\bar{x}) &= \frac{4}{3}\frac{\mu_{\mathrm{TF}}}{g}R_{\mathrm{TF},y}R_{\mathrm{TF},z}\int_{-\sqrt{1-\bar{x}^2}}^{\sqrt{1-\bar{x}^2}} d\bar{y}\ \left(1 - \bar{x}^2 - \bar{y}^2\right)^{3/2} \\ &= \frac{2\pi}{3}\frac{\mu_{\mathrm{TF}}}{g}R_{\mathrm{TF},y}R_{\mathrm{TF},z}\left(1 - \bar{x}^2\right)^2. \end{aligned} \tag{4.40}$$

Thus, in one dimension, the proper functional form to use when fitting the normalized density distribution is

$$n_{\mathrm{TF}}^{\mathrm{1D}}(x) = \frac{2\pi}{3}\frac{\mu_{\mathrm{TF}}}{g}R_{\mathrm{TF},y}R_{\mathrm{TF},z}\left[1 - \left(\frac{x}{R_{\mathrm{TF},x}}\right)^2\right]^2, \tag{4.41}$$

while in two dimensions, the density profile takes the form

$$n_{\mathrm{TF}}^{\mathrm{2D}}(x,y) = \frac{4}{3}\frac{\mu_{\mathrm{TF}}}{g}R_{\mathrm{TF},z}\left[1 - \left(\frac{x}{R_{\mathrm{TF},x}}\right)^2 - \left(\frac{y}{R_{\mathrm{TF},y}}\right)^2\right]^{3/2}. \tag{4.42}$$

Using the functional form 4.41 and the bimodal fitting process previously discussed, we can extract condensate fraction and temperature, both of which are critical to the work

presented in chapter 6.

Chapter 5

Bose-Einstein condensates in optical lattices

With an understanding of some key properties of harmonically-confined Bose-Einstein condensates, we now turn our attention to condensates confined within an optical lattice and discuss the resulting dynamics. We will first discuss the dynamics which occur in static optical lattices, followed by those which take place in driven optical lattices. Note: unless otherwise mentioned, this chapter assumes the s-wave scattering length between atoms is Feshbach-tuned to be zero.

5.1 BECs in static optical lattices

A retro-reflected laser beam creates a standing wave of light whose electric field and thus intensity are periodic in space. The AC Stark effect, in which the energy levels of an atom are shifted by the oscillating electric field of radiation [1], implies that a standing wave of light creates a spatially-periodic potential. If the lattice light is red-detuned far from resonance, i.e. $|\delta| \gg \Gamma$, the nodes (anti-nodes) of the lattice correspond to potential

maxima (minima). In one dimension, the Hamiltonian of a particle in this potential is given by

$$\hat{H} = \frac{\hat{p}^2}{2m} + V_0 \cos^2(k_L \hat{x}) \tag{5.1}$$

or

$$\hat{H} = \frac{\hat{p}^2}{2m} + \frac{V_0}{2}\left[1 + \cos(2k_L \hat{x})\right] \tag{5.2}$$

where $k_L = 2\pi/\lambda = \pi/d$ is the wave vector of a lattice photon with wavelength λ, $d = \lambda/2$ is the lattice constant and the lattice depth V_0 is the peak trap depth of a Gaussian beam [28]:

$$V_0 = -\frac{3\pi c^2}{2\omega_0^3}\left(\frac{\Gamma}{\omega_0 - \omega} + \frac{\Gamma}{\omega_0 + \omega}\right) I_0 \tag{5.3}$$

Here, $\omega = 2\pi c/\lambda$ is the angular frequency of the trapping light, $\omega_0 = 2\pi c/\lambda_0$ is the angular frequency of the cooling transition, Γ is its linewidth, c is the speed of light and $I_0 = 2P/\pi w_0^2$ is the peak intensity of the beam with power P and waist w_0. We typically quote lattice depths in units of recoil energy, which is defined as $E_R = \hbar^2 k_L^2/2m$.

We are often only concerned with the relative energy difference between states, so we can discard the constant offset $V_0/2$ as it shifts the energies of the soon-to-be-found eigenstates equally, leaving

$$\hat{H} = \frac{\hat{p}^2}{2m} + \frac{V_0}{2}\cos(2k_L \hat{x}) \tag{5.4}$$

To find the energy spectrum of this Hamiltonian, first recall the action of $\hat{H}$ on an eigenstate $\varphi(x)$:

$$\hat{H}\varphi(x) = E\varphi(x) \tag{5.5}$$

Inserting the Hamiltonian (5.4), we see that finding the spectrum becomes an eigenvalue

problem as the kinetic and lattice operators do not commute:

$$\left[\frac{\hat{p}^2}{2m} + \frac{V_0}{2}\cos(2k_L\hat{x})\right]\varphi(x) = E\varphi(x) \tag{5.6}$$

Next, we impose the Bloch theorem, which states that solutions to (5.4) can be expressed as [29]

$$\varphi_q^n(x) = e^{iqx}u_q^n(x) \tag{5.7}$$

where $u_q^n(x)$ has the same periodicity of lattice, i.e. $u_q^n(x+d) = u_q^n(x)$, and e^{iqx} is a plane wave of momentum $\hbar q$. The index n denotes the energy band being considered, and these bands will be discussed more in a later section. For now, we can think of these energy bands as being analogous to the energy eigenstates of the quantum harmonic oscillator, in which the energy of a particle is determined by its state index m, i.e. $E_{\text{QHO}}^m = (m+\frac{1}{2})\hbar\omega$. Let us now investigate the effect of acting on (5.7) with the operators of the Hamiltonian. Applying the momentum operator, we have

$$\begin{aligned}
\hat{p}\varphi_q^n(x) &= -i\hbar\partial_x\left[e^{iqx}u_q^n(x)\right] \\
&= \left[-i\hbar(\partial_x e^{iqx})u_q^n(x) - i\hbar(\partial_x u_q^n(x))e^{iqx}\right] \\
&= e^{iqx}\left[\hbar q - i\hbar\partial_x\right]u_q^n(x) \\
&= e^{iqx}\left[\hat{p} + \hbar q\right]u_q^n(x).
\end{aligned} \tag{5.8}$$

A second application of $\hat{p}$ then gives

$$\begin{aligned}
\hat{p}^2\varphi_q^n(x) &= \hat{p}\left(e^{iqx}\left[\hat{p}+\hbar q\right]u_q^n(x)\right) \\
&= \hat{p}\left(e^{iqx}\hat{p}\,u_q^n(x)+\hbar q\,e^{iqx}u_q^n(x)\right) \\
&= \hbar q e^{iqx}\hat{p}u_q^n(x)+e^{iqx}\hat{p}^2u_q^n(x)+\hbar q\left(e^{iqx}\hat{p}\,u_q^n(x)+\hbar q\,e^{iqx}u_q^n(x)\right) \\
&= e^{iqx}\left[\hbar q\hat{p}u_q^n(x)+\hat{p}^2u_q^n(x)+\hbar q\hat{p}u_q^n(x)+\hbar^2q^2u_q^n(x)\right] \\
&= e^{iqx}\left[\hat{p}^2u_q^n(x)+2\hbar q\hat{p}u_q^n(x)+\hbar^2q^2u_q^n(x)\right] \\
&= e^{iqx}\left(\hat{p}+\hbar q\right)^2u_q^n(x),
\end{aligned} \tag{5.9}$$

so that the action of the kinetic energy operator is

$$\left(\frac{\hat{p}^2}{2m}\right)e^{iqx}u_q^n(x) = e^{iqx}\frac{\left(\hat{p}+\hbar q\right)^2}{2m}u_q^n(x) \tag{5.10}$$

using the Bloch ansatz. Next, we repeat this process for the potential energy operator, but because $[e^{iqx},\cos(2k_L\hat{x})]=0$, we can simply move the exponential to the left:

$$\left(\frac{V_0}{2}\cos(2k_L\hat{x})\right)e^{iqx}u_q^n(x) = e^{iqx}\left(\frac{V_0}{2}\cos(2k_L\hat{x})\right)u_q^n(x) \tag{5.11}$$

Application of the Hamiltonian to the Bloch theorem ansatz (5.7) therefore gives

$$\hat{H}\varphi_q^n(x) = e^{iqx}\left[\frac{(\hat{p}+\hbar q)^2}{2m}+\frac{V_0}{2}\cos(2k_L\hat{x})\right]u_q^n(x) = E_n(q)e^{iqx}u_q^n(x) \tag{5.12}$$

where $E_n(q)$ is the band dispersion for the n^{th} Bloch band. Since $E_n(q)$ is independent of x, we can swap its position with e^{iqx} and left-multiply both sides by e^{-iqx} to obtain

$$\hat{H}u_q^n(x) = \left[\frac{(\hat{p}+\hbar q)^2}{2m}+\frac{V_0}{2}\cos(2k_L\hat{x})\right]u_q^n(x) = E_n(q)u_q^n(x). \tag{5.13}$$

This is now the eigenvalue equation we wish to solve, and a basis must be chosen so that the matrix representation of $\hat{H}$ can be found and subsequently diagonalized. The terms of $\hat{H}$ do not commute, so the choice of basis largely boils down to convenience or personal preference. Here, we choose the plane wave, i.e. free-particle or momentum-state, basis:

$$\psi_k(x) = \frac{e^{ikx}}{\sqrt{2\pi}} \tag{5.14}$$

Each $\psi_k(x)$ is, of course, an eigenstate of the momentum operator with momentum $\hbar k$:

$$\begin{aligned} \hat{p}\psi_k(x) &= -i\hbar\frac{\partial}{\partial x}\left(\frac{e^{ikx}}{\sqrt{2\pi}}\right) \\ &= -i^2\hbar k\frac{e^{ikx}}{\sqrt{2\pi}} \\ &= \hbar k\psi_k(x). \end{aligned} \tag{5.15}$$

Defining $\hat{T} = \hat{p}^2/2m$ and $\hat{V} = (V_0/2)\cos(2k_L x)$ as the kinetic and potential operators, respectively, the matrix representations of each can be found using our chosen set basis states:

$$\begin{aligned} \hat{T}_{k'k} = \langle k'|\frac{(\hat{p}+\hbar q)^2}{2m}|k\rangle &= \frac{1}{2\pi}\int_{-\infty}^{\infty} dx\ e^{-ik'x}(\hat{p}+\hbar q)^2 e^{ikx} \\ &= \frac{1}{2\pi}\int_{-\infty}^{\infty} dx\ e^{-ik'x}\left[\frac{\hbar^2(k+q)^2}{2m}\right]e^{ikx} \\ &= \frac{1}{2\pi}\left[\frac{\hbar^2(k+q)^2}{2m}\right]\int_{-\infty}^{\infty} dx\ e^{i(k-k')x} \\ &= \frac{\hbar^2(k+q)^2}{2m}\delta(k-k') \\ &= \frac{\hbar^2(q+2jk_L)^2}{2m}\delta(k-k') \end{aligned} \tag{5.16}$$

$$\begin{aligned}
\hat{V}_{k'k} = \langle k'|\frac{V_0}{2}\cos(2k_L\hat{x})|k\rangle &= \frac{V_0}{4\pi}\int_{-\infty}^{\infty} dx\ e^{-ik'x}\cos(2k_L\hat{x})e^{ikx} \\
&= \frac{V_0}{4\pi}\int_{-\infty}^{\infty} dx\ e^{-ik'x}\left(\frac{e^{2ik_Lx}+e^{-2ik_Lx}}{2}\right)e^{ikx} \\
&= \frac{V_0}{8\pi}\int_{-\infty}^{\infty} dx\ \left[e^{i(k-k'+2k_L)x}+e^{i(k-k'-2k_L)x}\right] \\
&= \frac{V_0}{4}\left[\delta(k-k'+2k_L)+\delta(k-k'-2k_L)\right]
\end{aligned} \tag{5.17}$$

where in both cases we make use of one definition of the Dirac delta function,

$$\delta(k-k') = \frac{1}{2\pi}\int_{-\infty}^{\infty} dx\ e^{i(k-k')x}. \tag{5.18}$$

So, we see that in the plane wave basis $\hat{T}$ is diagonal while $\hat{V}$ only contains off-diagonal entries, giving a matrix representation of $\hat{H}$ which is tridiagonal. Finding the eigenvalues and eigenvectors of $\hat{H}$ will give the energies and Bloch states of the lattice, respectively, at a given quasimomentum q. Let's now derive an explicit form for the matrix to be diagonalized, which will also make clear how to proceed numerically. Any explicit numerical calculations will require truncation of the number of basis states used, and it is important to ensure that the size of the basis $l \gg m$, where we are interested in the first m bands.

$$\hat{T} = \frac{\hbar^2}{2m} \begin{pmatrix} \ddots & 0 & 0 & 0 \\ 0 & (q-2k_L)^2 & 0 & 0 \\ 0 & 0 & q^2 & 0 \\ 0 & 0 & 0 & (q+2k_L)^2 \\ & & & \ddots \end{pmatrix} \tag{5.19}$$

$$\hat{V} = \frac{V_0}{4} \begin{pmatrix} \ddots & 1 & 0 & 0 \\ 1 & 0 & 1 & 0 \\ 0 & 1 & 0 & 1 \\ 0 & 0 & 1 & 0 \\ & & & \ddots \end{pmatrix}. \tag{5.20}$$

Note that both $\hat{T}$ and $\hat{V}$ are $m \times m$ square matrices.

Finding the eigenvalues and eigenvectors of $\hat{H} = \hat{T} + \hat{V}$ using these matrix expressions gives the Bloch states $\{u_q^n(x)\}$ and their associated energies $\{E_n(q)\}$ for a particular quasimomentum q. Repeating this calculation over the entirety of the first Brillouin zone, i.e. for all quasimomentum $q \in [-\pi/d, \pi/d]$, gives the dispersion relations $\{E_n(q)\}$ for the band energies as a function of quasimomentum, and the set of all band dispersions is known as the band structure of the lattice. Note that calculation of the band structure explicitly depends on the lattice depth V_0, so it must be recalculated when considering different depths. There are two important limits to keep in mind which can provide intuition when dealing with band structure. In the limit of an infinitely-deep lattice, the shape of each band tends toward flatness and uniformity across the Brillouin zone as the lattice potential dominates over kinetic energy and "freezes out" atomic motion. In the opposite limit, where the lattice is very weak, the band structure approaches the dispersion of a free particle, with the dispersion "folded inward" or "reflecting from" the edges

of the zone. To see this, consider the calculated band structure for a $1E_R$-deep lattice in the left plot of Figure 5.1, which is shown for the first Brillouin zone of quasimomentum. If we again plot this same band structure but in the extended-zone scheme, as shown in Figure 5.2, we see two key features: firstly, the first Brillouin zone of quasimomentum fully captures the behavior of each band and is thus sufficient to describe the system. Secondly, the extended-zone scheme better illustrates the manifestation of band structure from multiple overlapping free-particle dispersions.

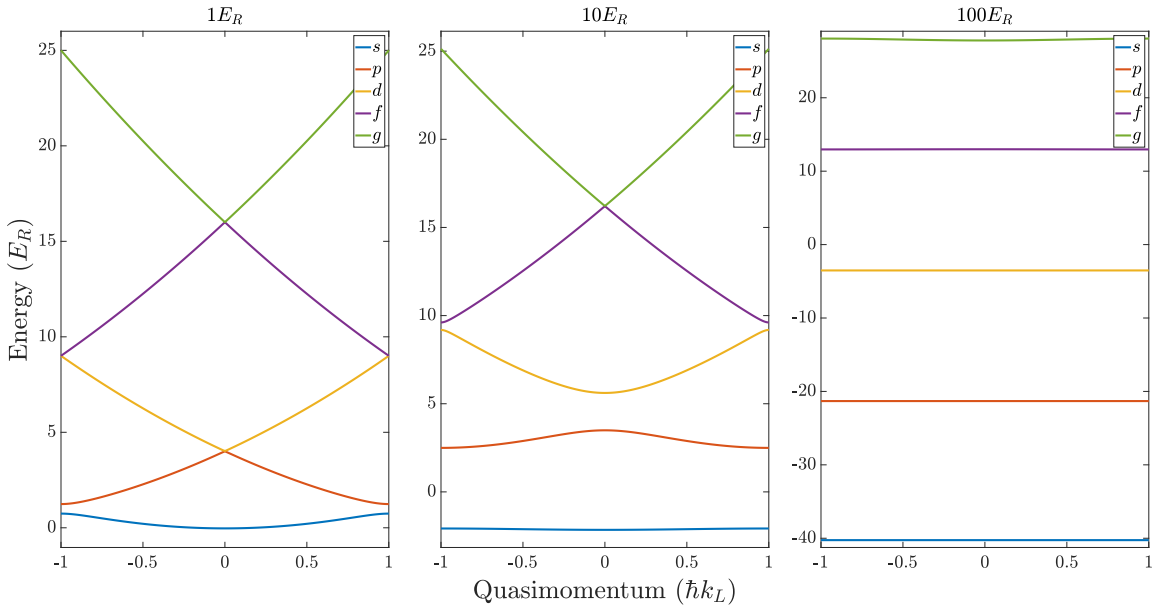

Figure 5.1: Band structures of a static optical lattice for different lattice depths V_0. Left: at shallow lattice depth of $1E_R$, bands resemble overlapping free-particle energy dispersions. Middle: at moderate depth $10E_R$, bands have reduced curvature and gaps between bands are larger. Right: at deep lattice depth of $100E_R$, bands have very little curvature, energy spacing between band pairs are more uniform and bands closely resemble quantum harmonic oscillator eigenstates.

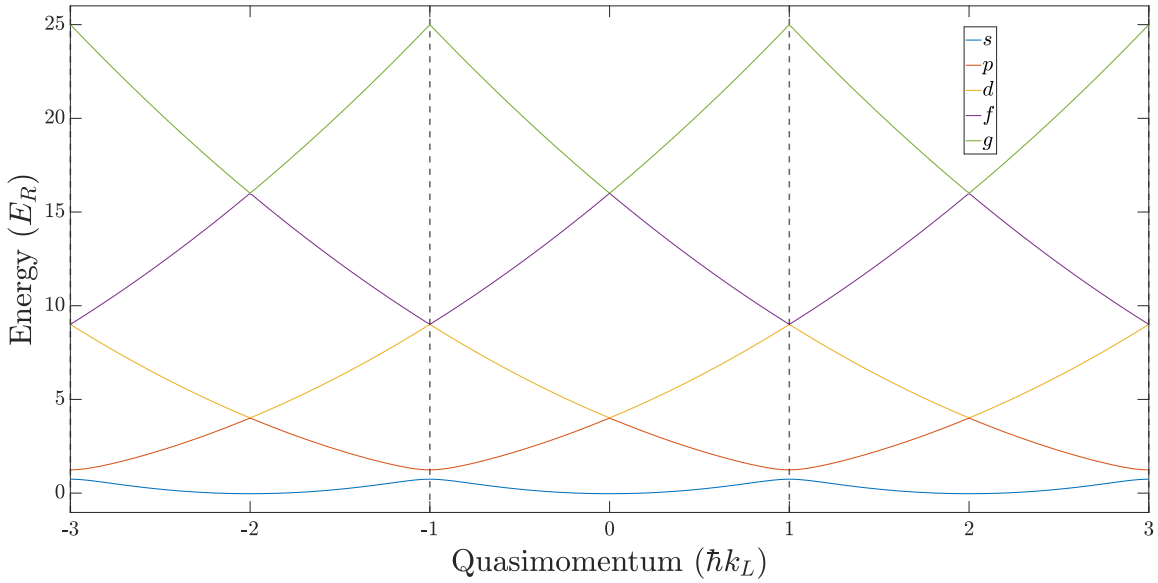

Figure 5.2: Band structure of $1E_R$ static optical lattice in the extended zone scheme. Edges of first Brillouin zone of quasimomentum are indicated with vertical dashed lines.

5.2 Position-space Bloch oscillations

Generically, a quantum particle confined by a spatially periodic potential will undergo Bloch oscillations when a constant external force is applied to the system, with the quasimomentum evolving linearly in time [30]: $q(t) = q(0) + Ft/\hbar$. These oscillations occur in both position and quasimomentum-space, but for many of the species used in cold atom experiments, the atoms are massive enough that the amplitude of position-space oscillations is too small to make observation practical, with the position-space amplitude given by the Wannier-Stark localization length l_{WS} [10]:

$$l_{\mathrm{WS}} = 2J/F = \frac{\Delta_n}{2F}. \tag{5.21}$$

Here, J is the tunneling energy between lattice sites, F is the applied force and $\Delta_n = 4J$ is the bandwidth of the n^{th} band. The oscillation amplitude l_{WS} can be made larger by:

increasing the bandwidth Δ_n (equivalent to increasing the tunneling energy J), lowering the lattice depth, applying a weaker force, or some combination of these. Additionally, since $J \propto 1/m$, the low mass of lithium magnifies the position-space motion, resulting in position-space Bloch oscillations which can be readily observed and characterized [10]. As a point of comparison, for the same applied force and lattice depth, ^{7}Li oscillates with an amplitude 12.4 times larger than ^{87}Rb, which corresponds to the ratio of their atomic masses.

In the case of a lattice potential, the band structure dictates the position-space motion, or equivalently, the position-space trajectory directly maps out the lattice band structure [10]:

$$E_n = \frac{hf_B}{d}x,\ q = \frac{2k_L}{T_B}t \tag{5.22}$$

Additionally, the mean group velocity of the atomic ensemble is determined by the band dispersion $E_n[q(t)]$:

$$\frac{\mathrm{d}\langle x(t)\rangle}{\mathrm{d}t} = \langle v_G(t)\rangle = \frac{1}{\hbar}\frac{\partial E_n(t)}{\partial q}. \tag{5.23}$$

From this, it is clear that if one can engineer the band structure of the lattice, the position-space evolution will also be determined. This critical fact is central to the interferometry scheme we propose in chapter 7.

5.3 BECs in driven optical lattices

Building on the results of the previous section, we now incorporate time-periodic amplitude modulation of the lattice:

$$\hat{H}(t) = \hat{p}^2/2m + \frac{V_0}{2}[1 + \alpha\sin(\omega t)]\cos(2k_L\hat{x}). \tag{5.24}$$

Here, V_0 is the depth of the undriven lattice, α is the relative modulation strength and ω is the angular frequency of the amplitude modulation. Due to the form of the modulation, the continuous time translation symmetry of the static lattice is broken and instead $\hat{H}(t)$ possesses discrete time translation symmetry, i.e., $\hat{H}(t+T) = \hat{H}(t)$ for $T = 2\pi/\omega$. The formalism with which one can study Hamiltonians with temporal periodicity is known as Floquet theory, and further details and more rigorous derivations can be found in [4]. In this section, we focus on the physical implications of time-periodic amplitude modulation of the lattice and the new capabilities this unlocks.

The time-periodic nature of the Hamiltonian results a "folding" of energy into a first quasienergy Brillouin zone where $\varepsilon \in [-\hbar\omega/2, \hbar\omega/2]$, in addition to possessing a first quasimomentum Brillouin zone. Just as quasimomentum is only defined up to an integer multiple of $2\hbar k_L$, quasienergy is only defined up an integer multiple of the drive "photon" energy $\hbar\omega$, where ω is again the angular frequency associated with the modulation.

Following the treatment in [4], any solution to the time-dependent Schrödinger equation can be expanded as

$$|\psi(t)\rangle = \sum_n a_n \, |f_n(t)\rangle \, e^{-i\varepsilon_n t/\hbar}, \tag{5.25}$$

where $\{|f_n(t)\rangle\}$ are the T-periodic Floquet functions, $\{\varepsilon_n\}$ are their associated quasienergies and $\{a_n\}$ are time-independent expansion coefficients. This expression looks like the time evolution of a state governed by a time-independent Hamiltonian but with time-dependent basis states and quasienergies instead of energies. This parallel allows us to define the Floquet Hamiltonian $\hat{G}$ which is independent of time and which can be used to propagate an initial state $|\psi(0)\rangle$ forward in time. Further, the eigenvectors and eigenvalues of $\hat{G}$ correspond to the Floquet states and quasienergies, respectively, of the driven system.

The utility of the computing the stroboscopic Floquet Hamiltonian $\hat{G}$ goes beyond

calculating Floquet states and Floquet-Bloch band structures; it can also be used to perform highly efficient numerical time evolution to obtain the stroboscopic dynamics of a system. While this approach does not capture the so-called micromotion dynamics which occur on sub-cycle timescales, it generally captures the relevant behavior for experiments where the drive frequency is fast compared to the timescale of atomic motion (the Bloch periods we can achieve are on the order of tens of ms). The corresponding unitary time evolution operator is given by

$$\hat{U}(t,0) = \exp\left(-i\hat{G}t/\hbar\right). \tag{5.26}$$

When applied to an initial state $|\psi(t=0)\rangle$, this operator propagates forward in time to t:

$$|\psi(t)\rangle = \hat{U}_t\,|\psi(0)\rangle\,, \tag{5.27}$$

where we have used $\hat{U}_t$ in place $\hat{U}(t,0)$ for notational simplicity. The operator which propagates forward in time by a full period T is known as the stroboscopic unitary time evolution operator, or the Floquet propagator, and is given by

$$\hat{U}(T,0) = \exp\left(-i\hat{G}T/\hbar\right). \tag{5.28}$$

That is, $|\psi(t=T)\rangle = \hat{U}_T\,|\psi(t=0)\rangle$, where we have similarly used $\hat{U}_T$ in place of $\hat{U}(T,0)$ for notational simplicity. Successive applications of $\hat{U}_T$ will thus give the stroboscopic time-evolved state:

$$|\psi(t=NT)\rangle = \hat{U}_T^N\,|\psi(t=0)\rangle\,. \tag{5.29}$$

To propagate forward to a non-integer multiple of the drive period, we can compute $\hat{U}(T,0)$, apply it N times to reach $t=NT$, and then compute $\hat{U}(t,0)$ over some fraction

of a full period to propagate to a desired final time $t_f = NT + t'$:

$$|\psi(t = NT + t')\rangle = \hat{U}_{t'}\, \hat{U}_T^N\, |\psi(t = 0)\rangle\,, \tag{5.30}$$

where $t' < T$.

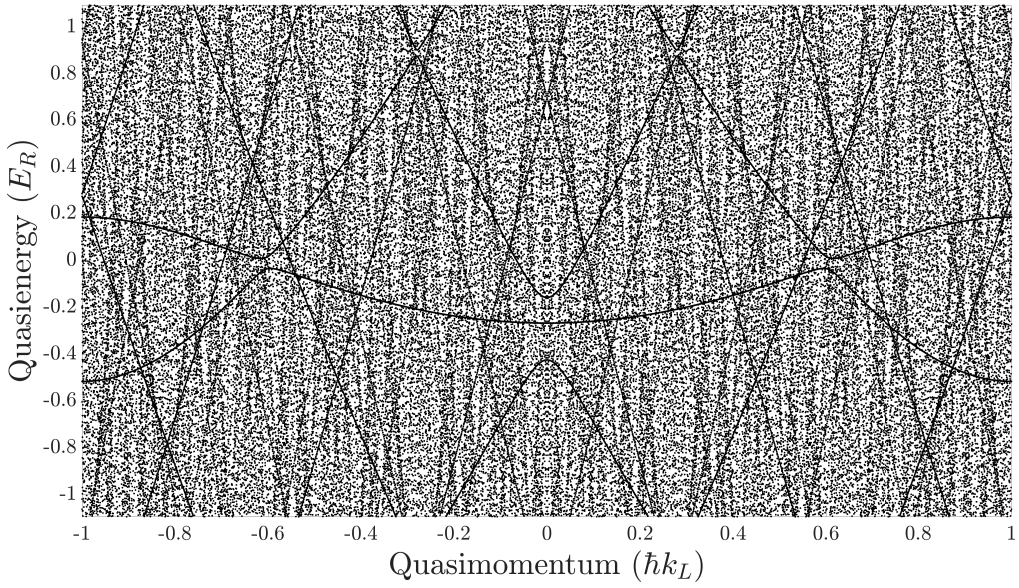

Figure 5.3: Raw spectrum of the stroboscopic Floquet Hamiltonian $\hat{G}$ obtained via numerical diagonalization. Here, $V_0 = 3E_R$, $f = 55$ kHz, $\alpha = 0.1$ and we only consider the first five static Bloch bands. Plane-wave basis is truncated beyond $||p| = 100\hbar k_L\rangle$ but includes $|p = 0\hbar k_L\rangle$, so 51 states are used.

To numerically find the stroboscopic, time-independent Floquet Hamiltonian $\hat{G}$ and its spectrum, we use the following approach:

1. Split the period T of a single drive cycle into N discrete times so that $\Delta t = T/N$ and $t_{i+1} = t_i + \Delta t$, which simply means that time increments by Δt at each step. For simplicity, let $t_1 = 0$.

2. At each time t_i and for a particular quasimomentum q, find $\hat{H}(t_i)$ by constructing the operators $\hat{T}(t_i)$ and $\hat{V}(t_i)$. Note that $\hat{T}$ is the same for all t_i while $\hat{V}$ is different

at each t_i due to the changing lattice depth. Combine these to find the Hamiltonian at time t_i: $\hat{H}(t_i) = \hat{T}(t_i) + \hat{V}(t_i)$.

3. Construct the time evolution operator $\hat{U}_i$ over the small interval of time Δt: $\hat{U}_i := \hat{U}(t_i + \Delta t, t_i) = \exp\left(-i\hat{H}(t_i)\Delta t/\hbar\right)$.

4. After computing each $\hat{U}_i$ for all N points in time, construct the single-cycle Floquet propagator $\hat{U}(T, 0)$ which is given by the product of all N individual propagators: $\hat{U}(T, 0) = \prod_{i=1}^{N} \hat{U}_i = \hat{U}(N\Delta t, (N-1)\Delta t)...\hat{U}(2\Delta t, \Delta t)\hat{U}(\Delta t, 0)$.

5. Writing $\hat{U}(T, 0) = \exp\left(-i\hat{G}T/\hbar\right)$, find the Floquet Hamiltonian using $\hat{G} = (i\hbar/T)\ln\hat{U}(T, 0)$.

6. Find the Floquet states and their associated quasienergies by solving for the eigenvectors and eigenvalues of $\hat{G}$, respectively.

7. Compute the overlap C_{lm} between the Bloch states of the static lattice and the Floquet states of the driven lattice: $C_{lm} = \langle\psi_B^l|\psi_F^m\rangle$, where $|\psi_B^l\rangle$ is the l^{th} Bloch state and $|\psi_F^m\rangle$ is the m^{th} Floquet state. From this, compute the squared overlap $P_{lm} = |C_{lm}|^2$.

8. Order the Floquet states and their associated quasienergies by the squared overlap P_{lm}, where the largest overlap corresponds to the first Floquet band.

9. Repeat these steps over the range of quasimomenta being considered to obtain both the raw Floquet spectrum (Fig. 5.3) as well as the sorted Floquet band spectrum (Fig. 5.4), the latter of which reveals the new, effective band dispersions resulting from the drive.

The code used to calculate Floquet band structures can be found on our GitHub, `https://github.com/weldlabucsb`, and Figure 5.4 illustrates the results of this process. In the left panel, the static Bloch bands are plotted in the first Brillouin zone of

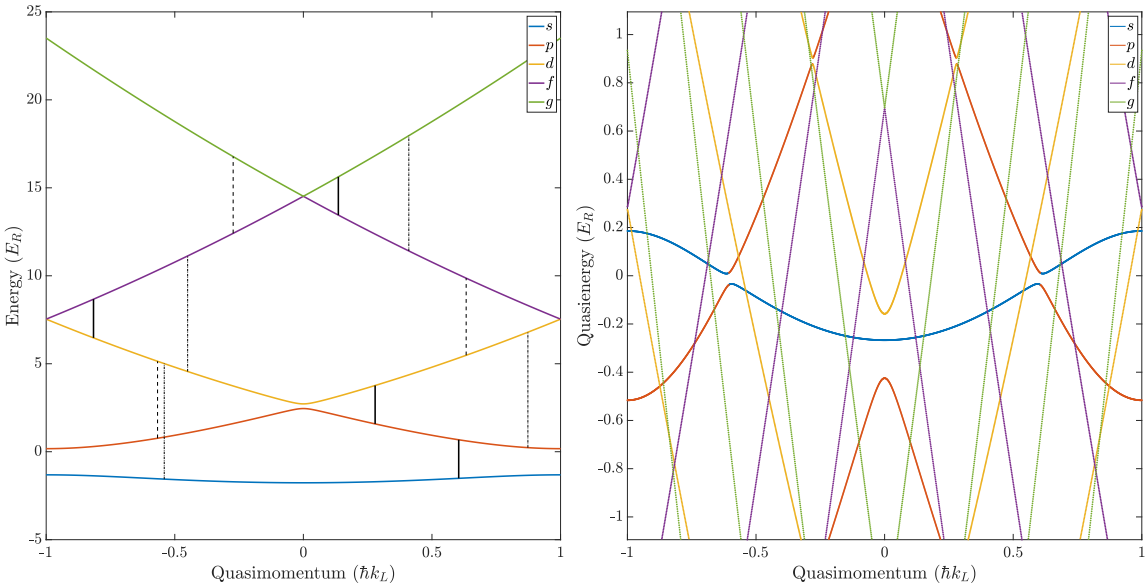

Figure 5.4: Band structures of static and driven lattices at the same primary depth $V_0 = 3E_R$. Left: static Bloch band structure where black lines indicate one, two and three-photon interband couplings (solid, dashed and dot-dashed lines, respectively). Right: Floquet-Bloch band structure of the same stroboscopic Floquet Hamiltonian $\hat{G}$ as in Fig. 5.3, now sorted using the squared overlap P_{lm}. Again, $f = 55$ kHz, $\alpha = 0.1$ and we only consider the first five static Bloch bands. Plane-wave basis is truncated beyond $||p| = 100\hbar k_L\rangle$ for both band structures, so 51 states are used.

quasimomentum, with black lines indicating resonant couplings between static bands. In the right panel, performing the procedure outlined above results in the sorted Floquet-Bloch band structure, and we see that the character of each resulting Floquet-Bloch band has character from multiple different static bands. These Floquet-Bloch bands give rise to an effective band structure and determine the transport properties of traversing atoms, namely the mean group velocity and thus position-space motion. Through this selective "stitching together" of different static bands, early ^{7}Li early experiments in our group were able to map out Floquet-Bloch band structure [10], investigate the relativistic harmonic oscillator [11], and engineer millimeter-scale long-range transport [12]. In chapter 7, we propose a scheme for noise-immune continuously-trapped atom interferometry which harnesses the power of Floquet band engineering.

Chapter 6

Thermodynamic engine with a quantum degenerate working fluid

This chapter is based on and adapted from our published work "Thermodynamic engine with a quantum degenerate working fluid" [5].

6.1 Introduction

Classical thermodynamic engines have been critical to human technology since the industrial revolution. In the past decade, the capabilities of quantum thermodynamic engines have been explored theoretically [31–50], and recent years have seen experimental demonstrations of both quantum and nanoscopic classical engines using single ions [51, 52], nuclear spins [53], cold atoms [54–57], nitrogen-vacancy centers [58], and quantum gases [59, 60]. A natural question is whether quantum phenomena can enhance the performance of a thermodynamic engine [61–63]. Perhaps the simplest experimental approach to this question — the direct comparison of an engine using a classical working fluid to an equivalent one using a quantum degenerate working fluid — has remained

unexplored.

Here, we extend our Floquet work cyclically varying parameters in the Hamiltonian towards quantum realization of a key classical technology and explore the role of quantum degeneracy in the performance of a thermodynamic engine. The magnetic Feshbach resonance accessible in ^{7}Li is a powerful tool which allows us to explore interaction effects in such an engine. Thermodynamic engines typically operate with some coupling to a bath or reservoir, and here we use a condensate coupled to both optical and magnetic fields to create an analogous system where the BEC acts to mediate energy transfer between fields. Concretely, we use a crossed ODT to create a trap which can be compressed and relaxed while using a DC magnetic field to Feshbach-enhance and suppress interparticle scattering. This sequence of trap compression, interaction enhancement, trap relaxation and interaction suppression enables the straightforward investigation of the role of quantum degeneracy in the performance of a thermodynamic engine.

6.2 Theory

We can begin to make a connection between our thermodynamic engine with a quantum degenerate working fluid and classical heat engines by considering the effect of each stroke on the condensate. In the first stroke, the optical trap is compressed while the scattering length is held constant, so the optical field performs positive work on the BEC which increases its internal energy and is analogous to a heating stroke in a classical engine. Following this compression, the strength of the trap is fixed and interparticle scattering is enhanced using a DC magnetic field, which also performs positive work on the condensate and mimics transfer of heat into a working fluid at constant volume. The scattering length is then fixed as the optical trap is relaxed which results in the BEC performing positive work on the optical field. Finally, the optical trap strength is held

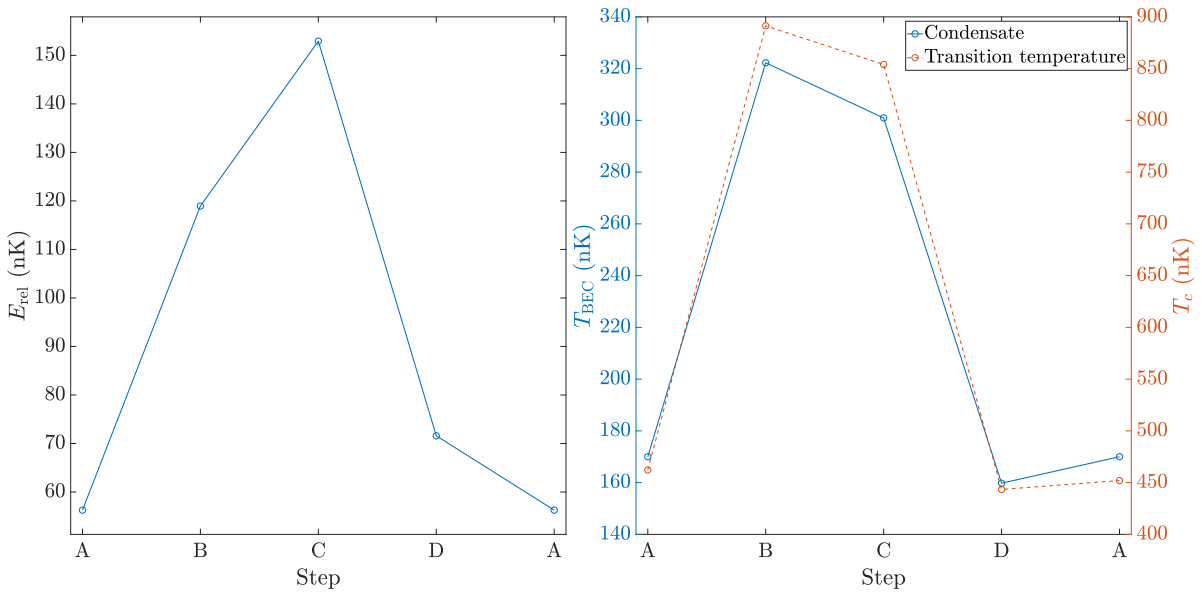

Figure 6.1: Left: analytic predictions of release energy per particle E_{rel} for with entropy fixed over the cycle to its value at Step A. Right: condensate temperature (left axis) and transition temperature T_c (right axis). While the condensate changes in temperature over the cycle, T_c shifts accordingly such that the condensate fraction remains approximately constant. Here, $N = 5 \times 10^5$, $T = 170$ nK, $a_s^A = 100a_0$, $a_s^C = 240a_0$, $\bar{\omega}_A = 2\pi \times 133$ Hz and $\bar{\omega}_B = 2\pi \times 257$ Hz.

constant while interactions are suppressed, where the BEC performs positive work on the magnetic field. In a classical context, the sequence of adiabatic compression, isochoric heating, adiabatic expansion and isochoric cooling realizes an Otto cycle, and in section 6.5.5 we show how our thermodynamic engine maps onto the classical Otto cycle.

A key question is, what does one expect to happen when an interacting condensate is subjected to the cycle described above? While perhaps not the obvious first step, we must establish our assumptions about the cycle as it will inform how we treat it theoretically. The principle assumption is that the cycle is isentropic, a condition which further implies adiabaticity and reversibility. Through the use of the finite-temperature analytical result equation 4.27 from [2], we can work out the expected behavior of the energy over the course of the cycle as shown in the left panel of Figure 6.1. The implication of holding

entropy constant is that, for a given trap frequency $\bar{\omega}$ and scattering length a_s with fixed atom number N, the temperature T of the system is determined at each step, and the behavior of T over the cycle is therefore a central point of interest.

To be concrete, the known values of atom number, scattering length, trap frequency and temperature at step A allow one to calculate the initial entropy per particle $S_A = S(N, a_s^A, \bar{\omega}_A, T_A)/Nk_B$ using equation 4.26. Then, treating atom number as constant over the course of a single cycle and holding entropy constant, the temperature at each step of the cycle can be determined using each trap frequency-scattering length pair. That is, at step i, we solve for the temperature T_i which satisfies

$$\begin{aligned} S_i &= \frac{S(N, a_i, \bar{\omega}_i, T_i)}{Nk_B} = S_A \\ 4\frac{\zeta(4)}{\zeta(3)} t_i^3 &+ 3\eta_i t_i^2 \left(1 - t_i^3\right)^{2/5} = S_A \end{aligned} \tag{6.1}$$

where $t_i = T_i/T_c^0$. The right panel of Figure 6.1 shows the BEC and transition temperatures over the course of the cycle. It is interesting to note that while the condensate exceeds the critical temperature at step A of ~ 470 nK, the critical temperature changes over the cycle as well such that the condensed fraction remains the approximately constant, which is a consequence of holding S constant.

The release energies plotted in Figure 6.1 demonstrate that the changes in energy are not equal and opposite for each pair of strokes altering either trap frequency or scattering length. This indicates a net transfer of energy from magnetic to optical fields. That is, the work performed by the optical field on the $100a_0$ BEC during trap compression stroke AB is not the same as the work done by the $240a_0$ BEC on the optical field during trap relaxation stroke CD, which results in an asymmetry in the cycle when plotting E_{rel} at each step. Similarly, the work done by the magnetic field on the condensate in stroke BC differs from the work done by the condensate on field in stroke DA. Microscopically,

energy is exchanged between the Gaussian trapping beams and the atoms via stimulated absorption and emission of photons into or out of the optical field. The exchange of energy between the magnetic coils and the atoms is instead due to the changing magnetization which occurs when ramping the Feshbach field, which is a consequence of the changing virtual admixture of the closed-channel molecular state. The changing magnetization gives rise to bound currents which vary in time, resulting in an electromotive force. Additionally, this relatively simple calculation confirms that the BEC acts as a working fluid, mediating the transfer of energy between magnetic and optical fields without a net change in energy over the cycle. Further, we can see that performing the cycle in reverse will transfer energy from optical to magnetic fields. Of course, implicit in these calculations is that the BEC wavefunction evolves adiabatically between steps, i.e. it is valid to calculate the release energy at each step separately rather than performing a computationally-expensive time-dependent simulation. With adiabaticity being key to our understanding of the cycle, as well as to the equilibrium fully-interacting numerics developed by Kimberlee Keithley and described in [64], we ensured that a high degree of adiabaticity was maintained in our data sets, except when deliberately exploring the effects of shorter cycle times. We quantify the degree of adiabaticity in the next section.

6.3 Experimental setup

With the theory in hand, we now look at experimental implementation of the cycle. We proceed under the assumption that we have determined the trap frequency $\bar{\omega}_i$ at each step along the cycle, and that we have implemented ramp waveforms which linearize $\bar{\omega}(t)$ and $a_s(t)$, i.e. $\dot{\bar{\omega}}(t) =$ constant and $\dot{a}_s(t) =$ constant along the trap and interaction strokes, respectively. The details of the trap frequency calibration process are given in appendix A.1 while the procedure for linearizing trap and interaction ramps is discussed

in appendix A.2.

6.3.1 Adiabaticity

When designing ramp sequences and choosing ramp rates, we estimate the adiabaticity by comparing the rate of change in trap frequency with an elementary excitation, namely, the quadrupolar "breathing" mode. In the Landau-Zener formalism, the probability of passage between two states is given by [65]

$$\begin{aligned} P_{\mathrm{LZ}} &= e^{-1/\Theta}, \\ \Theta &= \frac{1}{2\pi}\frac{\dot{\omega}_E}{\omega_E^2}. \end{aligned} \tag{6.2}$$

To avoid unwanted excitations, one needs to ensure that the adiabaticity parameter $\Theta \ll 1$. Here, ω_E is the angular frequency associated with the gap in energy between the two states. In the case of a collective quadrupolar excitation, the associated frequency is [66] $\omega_Q = \sqrt{2}\bar{\omega}$ with an associated energy gap $E_Q = \hbar\omega_Q = \sqrt{2}\hbar\bar{\omega}$. Rewriting Θ in terms of $\bar{\omega}$, we have

$$\Theta = \frac{1}{2\pi}\frac{\sqrt{2}\dot{\bar{\omega}}}{2\bar{\omega}^2} = \frac{1}{2\sqrt{2}\pi}\frac{\dot{\bar{\omega}}}{\bar{\omega}^2} \tag{6.3}$$

Something which may not be immediately obvious is that what we have actually solved for is the adiabaticity parameter as a function of time, since $\bar{\omega}$ itself is changing in time during trap compression and relaxation. Thus, when calculating adiabaticity, it is important to consider the largest value of Θ over the course of the trap ramp. In our case, where $\dot{\bar{\omega}}$ is constant during trap compression and relaxation, the largest value of Θ occurs when $\bar{\omega}$ is smallest, i.e. the beginning of trap compression or the end of trap relaxation.

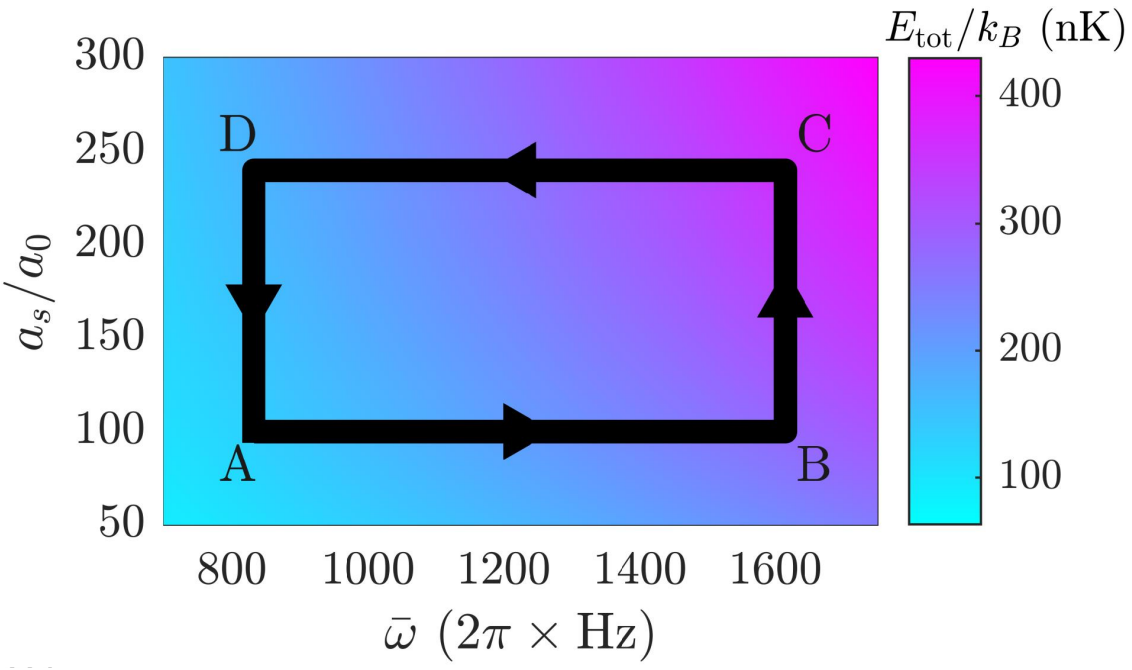

Figure 6.2: Thermodynamic cycle to which the BEC is subjected in a_s-$\bar{\omega}$ space. Color bar indicates total energy per particle E_{tot} at each step.

6.3.2 Experimental conditions for paper data

For all condensate data presented in the paper, the starting point is a $100a_0$ BEC, achieved by first making a high-field, i.e. $240a_0$, BEC and then slowly ramping the field over the course of 200 ms. Everything is then held constant for 600 ms to ensure that any remaining thermalization, loss and equilibration take place before the cycle begins. The geometric mean trap frequency $\bar{\omega}$ is about $2\pi \cdot 133$ Hz. This set of conditions is referred to as step A.

Following step A, the trap frequency $\bar{\omega}$ is ramped linearly to compress the trap using functional form A.12 while the magnetic field, and thus interaction strength, is held constant. This constitutes step B of the cycle. Then, the trap frequency is held constant as the magnetic field ramps to a higher value, resulting in an increase in interaction strength. As with the trap ramp, the field ramp is done so that the scattering length

changes at a constant rate using functional form A.4. The compressed trap and stronger interactions constitute step C. Subsequently, the dipole trap is relaxed, decreasing linearly at a constant rate, and this is step D. Finally, linearly decreasing the scattering length back to the initial value of $100a_0$ completes the cycle, bringing the system back to the conditions at step A. This cycle is shown in Figure 6.2.

For the thermal data presented in the paper, we intentionally reduced efficiency of optical evaporation by tuning the scattering length to $57a_0$ prior to evaporation, resulting in a cloud with a temperature around 1 μK. While it would have been ideal to prepare the thermal cloud at the same trap frequency as the condensate, we found that evaporating further resulted in either significant atom loss for weaker interactions or formation of a condensate for stronger interactions. Thus, to make our BEC-thermal comparison, the best we could do was keep the trap compression ratio the same for each cycle.

For all data presented in the paper [5], there were a number of Cicero and experimental settings that were common to all data sets. Firstly, all images taken from the PCO axis were after 12 ms of free expansion (time of flight), with a saturation parameter $s = I/I_{\text{sat}}$ of about 0.2. To correct for differences between our back-of-the-envelope atomic physics calculations ($\Delta f \approx 1.4\text{MHz/G} \cdot \Delta B$) and the actual resonance frequencies, we scanned the detuning of the imaging light at each scattering length using the MOTC DP VCO. At the optimal detuning, we observed a maximum in atom number and a minimum in the number of fringes surrounding the BEC in our images. This detuning scan vastly improved the quality and visibility of the clouds at steps C and D for all interaction strengths and made calculating E_{rel} more accurate. Additionally, we modified the fringe removal code written by Alec Cao and described in [67] so that we could use all images from a particular day with the same detuning as a single fringe library. This greatly improved the quality and SNR of the fringe-removed images when compared to only using images from a single folder to build the fringe library. We estimated the timescale

of drift in power and alignment of the imaging beam to be on the order of a day, hence only using multiple folders from a single day for fringe removal.

From time-of-flight sequences taken from both the vertical (PCO) and ODT (side Basler) axes, we discovered that we could not actually force cancel the BEC out to 12 ms. Instead, the wing coil currents were adjusted so that the condensate returned to its initial position after a 12 ms TOF which meant that the BEC remained roughly centered with respect to the imaging beam where the intensity is more uniform. The force due to the magnetic field gradient affects the spatial trajectory of the cloud but does not affect the release energy, as the expansion dynamics are dictated by the properties of the optical trap and the s-wave scattering length.

6.4 Data analysis

Understanding the behavior of both the condensed and thermal clouds over the course of the cycle requires us to extract and quantify an observable of interest, namely, the energy of the cloud at each step. The three-dimensional density distribution of a BEC allows us to calculate its kinetic energy, but only in the absence of a trapping potential and only after a finite time of flight. Because we rely on time of flight to map momentum space onto position space, the trap must be turned off so that the cloud can undergo free expansion. The release energy E_{rel}, given by 4.27, is determined only by the kinetic and interaction energies as the optical trap has been switched off resulting in zero potential energy. Imaging a cloud after a sufficiently long time of flight accomplishes two things: firstly, for sufficiently long TOF, all interaction energy associated with a BEC has been converted into kinetic energy, so a measurement of E_{kin} gives the true release energy E_{rel}. This is shown in the next section. Secondly, the mapping of momentum space onto position space achieved during TOF means that E_{rel} can be calculated by summing the

kinetic energies of all particles, using their positions and the time-of-flight to calculate each momentum contribution. In this section, we discuss how to calculate E_{rel} from absorption images.

6.4.1 Scale factor evolution

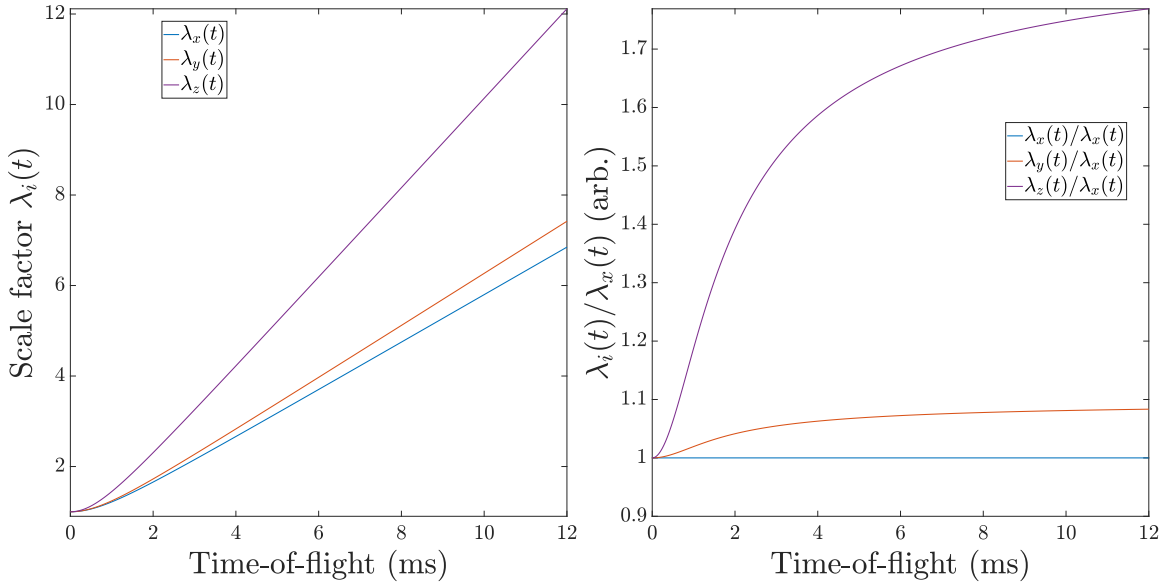

Figure 6.3: Left: scale factor evolution during time of flight where the trap is switched off at $t = 0$, and all scale factors satisfy $\lambda_i(0) = 1$. Right: the same evolution but with each scale factor rescaled by $\lambda_x(t)$ to show the expansion relative to the x-axis. Stronger initial confinement along a particular axis results in a greater degree expansion after the trap is switched off. The parameters of the trap are $\omega_x = 2\pi \times 114.7$ Hz, $\omega_y = 2\pi \times 121$ Hz and $\omega_z = 2\pi \times 166.7$ Hz.

To accurately compute the release energy of a BEC after a TOF, we need the full three-dimensional density distribution. As we will see shortly, this requires us to determine the expansion of the cloud along each axis, something which we cannot obtain from a column-integrated optical density profile. In the hydrodynamic treatment of BECs under the Thomas-Fermi approximation, the time-dependent coordinate of the cloud along

the i^{th} axis can be written as [2]

$$R_{\text{TF},i}(t) = \lambda_i(t) R_{\text{TF},i}(0) \tag{6.4}$$

where $\lambda_i(t)$ is a time-dependent dimensionless parameter known as the scale factor. For a trapped BEC with time-dependent trap frequencies, the scale factors can be obtained by solving

$$\ddot{\lambda}_i = \frac{\omega_i^2(0)}{\lambda_i \lambda_1 \lambda_2 \lambda_3} - \omega_i^2(t)\lambda_i \tag{6.5}$$

where $\omega_i(t)$ is the trap frequency along axis i as a function of time. For our experiments in which the cloud is initially confined and at equilibrium, followed by an abrupt switching off of the trap, the above definition of the scale factors implies that $\lambda_i(0) = 1$, and since the cloud is at rest to begin with, we also have that $\dot{\lambda}_i(0) = 0$. In principle, only the trap frequencies along each axis need to be known to determine the relative expansion between axes. However, when we numerically solved for the scale factors using our known trap frequencies the results were vastly different than the expansion we observed experimentally. This was a key discovery as it revealed how significantly lensing from the residual field curvature affects the cloud during expansion, especially at long times of flight where the BEC has moved appreciably and experiences a less uniform magnetic field. An added challenge in predicting cloud expansion is that our imaging system was focused to optimize for a BEC after 12 to 13 ms of TOF, and because of the nature of our imaging system, it was not feasible to rapidly switch between proper focusing at TOF 0 ms and TOF 12-13 ms. This meant that we were not able to take *in situ*, i.e. TOF 0 ms, images which would have given us the initial Thomas-Fermi radii $\{R_{\text{TF},i}(0)\}$, though our mysterious inability to measure optical densities greater than four would likely have been another hurdle, and the measured radii may not have been accurate. Even if we

had been able to measure the initial radii, it is unclear how useful this would have been without an exact model for the magnetic field profile to incorporate into the formula for scale factor evolution. As is often the case, a direct measurement of the cloud sizes after the full TOF was the best approach.

Once it became clear that the scale factors obtained from simulation were drastically different than what we observed experimentally and could not be used even as approximate values, we retook all of the data, this time imaging on both the PCO and ODT/side Basler axes for each data set. This allowed us to obtain the cloud sizes, and thus the scale factors, along all three axes with which we could extract the release energy of the cloud using Abel inversion, which we discuss now.

6.4.2 The Abel transform

The current lithium imaging system is single-axis, at least per shot. While we can, in principle, take images from both the PCO and side Basler axes, this would add additional complexity to our imaging setup. We typically only take data looking at either the side Basler (ODT) axis or PCO (top) axis, but for this experiment, we found that we needed both the relative and absolute sizes of the BEC along each axis to properly account for the projection of momenta with z-components onto the x-y plane, which is the effective column integration that occurs during absorption imaging.

One can imagine an atom at position $(0,0,z_0)$ in real space at time t_{TOF} is imaged onto the camera at position (0,0), and the kinetic energy of this atom is assessed to be zero when using only the optical density, despite it actually possessing kinetic energy $p^2/2m = (z_0/t_{\mathrm{TOF}})^2/2m$. Thus, it is necessary to regain the spatial information which is lost when performing absorption imaging, which acts as a column integral along z to give the optical density $\mathrm{OD}(x, y)$.

This is where Abel inversion comes into play. It is a method of reconstructing a 3D-radial distribution $f(r)$ which possesses axial symmetry (or can be rescaled such that it is axially symmetric, more on this shortly) from a known or measured 2D-radial distribution $F(\rho)$. To be clear, here r is the 3D radial coordinate while ρ is the 2D radial coordinate, $f(r)$ is the distribution of atoms in 3D and $F(\rho)$ is the distribution of atoms in 2D. The following relations express the Abel transform from f to F and the inverse Abel transform from F to f, respectively [68]:

$$F(\rho) = 2\int_{\rho}^{\infty} \frac{f(r)r}{\sqrt{r^2-\rho^2}}\, dr \tag{6.6}$$

and

$$f(r) = -\frac{1}{\pi}\int_{r}^{\infty} \frac{\mathrm{d}F}{\mathrm{d}\rho}\frac{d\rho}{\sqrt{\rho^2-r^2}}. \tag{6.7}$$

$F(\rho)$ and $f(r)$ must satisfy their respective normalization conditions

$$\int_0^{\infty} 2\pi\rho F(\rho)d\rho = N \tag{6.8}$$

and

$$\int_0^{\infty} 4\pi r^2 f(r)dr = N, \tag{6.9}$$

where N is the total atom number.

So, our goal here is to take the two-dimensional optical density profile obtained from our images, find the radial distribution $F(\rho)$ and use that to obtain the full three-dimensional profile $f(r)$. The first hurdle is that our BEC is not perfectly spherical,

and therefore not circular when projected into the x-y plane during imaging. However, all we require is that the distribution $F(\rho)$ be axially symmetric when rescaled with a suitable choice of scale factors [69]. That is, given an ellipsoidal cloud shape, we need to find the dimensionless scale factors a_x, a_y and a_z, and define $y' = (y/a_y)$ and $z' = (z/a_z)$ so that we can define the cylindrical radius $\rho' = \sqrt{x^2 + y'^2}$ and the spherical radius $r' = \sqrt{x^2 + y'^2 + z'^2}$, where we have we have eliminated a_x by simply scaling the other scale factors in terms of it, i.e. $a_y \to a_y/a_x$, $a_z \to a_z/a_x$ and $a_x \to 1$. This yields the axially-symmetric distribution $F(\rho')$ and we can then perform the inverse Abel transformation to obtain the 3D distribution $f(r')$. Once we obtain the radial distribution in the primed coordinate system, we can use the known relationship between scaled and unscaled coordinates to convert back to the unscaled coordinate system, which gives the proper 3D distribution of atoms in space, from which we can accurately calculate the kinetic energy. Concretely, we perform the following numerical analysis to compute E_{rel} at a single step for a given set of cycle parameters:

1. Side Basler/ODT axis image: compute $a_z/a_x = \sigma_z/\sigma_x$ using the cloud sigmas computed from the Gaussian fits in `doit` (note that `doit` does not know when up is y or z, so here σ_z refers to the extracted σ_y in the `doit` fits. Also note that doit does in fact spit out a value for σ_z for every curve fit, but this should be ignored as the code assumes that σ_z is just some multiplier times σ_x or σ_y, whichever is smaller).

2. PCO image: compute $a_y/a_x = \sigma_y/\sigma_x$ using the cloud sigmas computed from the Gaussian fits in `doit`.

3. Define the cylindrical radius $\rho' = \sqrt{x^2 + (y/a_y)^2} = \sqrt{x^2 + y'^2}$ and compute the radial average of the optical density to obtain $F(\rho')$.

4. Perform the inverse Abel transform 6.7 to obtain the radial distribution $f(r')$.

5. Evaluate the distribution $f(r') = f(\sqrt{x^2 + (y/a_y)^2 + (z/a_z)^2})$ over an unscaled 3D mesh grid to obtain the reconstructed density distribution (see B.1 for details).

6. Now that we have the density $n(\mathbf{r})$, we can finally compute E_{rel}. For an image taken after time-of-flight T, the velocity at position $\mathbf{r}$ is $\mathbf{v} = \mathbf{r}/T$, and we just need to weight the kinetic energy at each point by the density, so the calculation we want to perform is

$$E_{\text{rel}} = \int_0^{\mathbf{r}_0} \frac{1}{2} m v^2 n(\mathbf{r}) d^3\mathbf{r} = \frac{m}{2T^2} \int_0^{\mathbf{r}_0} r^2 n(\mathbf{r}) d^3\mathbf{r}, \tag{6.10}$$

where again we integrate well beyond the point where the density of atoms is on par with the image noise floor.

The details of how we implement this procedure numerically are given in B.1.

It is important to note that it is only at long TOFs that the assumption that all interaction energy has been converted to kinetic energy is valid. In terms of the scale factors λ_i discussed in 6.4.1, the release energy can be written as [70]

$$E_{\text{rel}} = \frac{2\mu_{\text{TF}}}{7} \left(\frac{1}{\lambda_x \lambda_y \lambda_z} + \frac{1}{2} \sum_i \frac{\dot{\lambda}_i^2}{\omega_i^2} \right), \tag{6.11}$$

with

$$E_{\text{kin}} = \frac{\mu_{\text{TF}}}{7} \left(\sum_i \frac{\dot{\lambda}_i^2}{\omega_i^2} \right) \tag{6.12}$$

and

$$E_{\text{int}} = \frac{2\mu_{\text{TF}}}{7} \left(\frac{1}{\lambda_x \lambda_y \lambda_z} \right), \tag{6.13}$$

where μ_{TF} is the chemical potential in the Thomas-Fermi approximation given by 4.12,

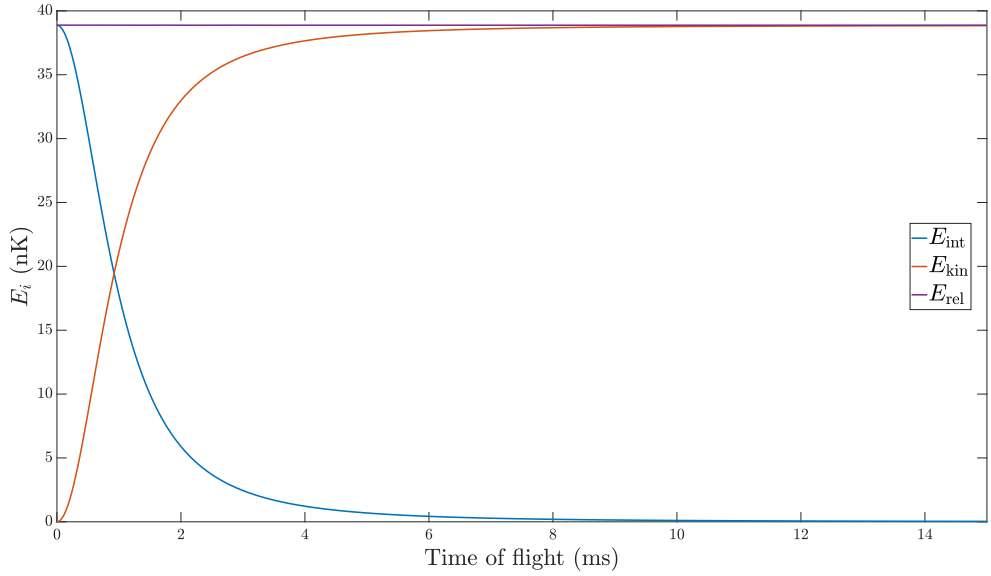

Figure 6.4: Conversion of interaction to kinetic energy during free expansion. Here, $N = 5 \times 10^5$, $\omega_x = 2\pi \times 114.7$ Hz, $\omega_y = 2\pi \times 120.95$ Hz, $\omega_z = 2\pi \times 166.69$ Hz, and $a_s = 100a_0$. By 6.25 ms, $E_{\text{int}}/E_{\text{rel}} < 0.01$ and by 12 ms, $E_{\text{int}}/E_{\text{rel}} < 0.002$. Due to conservation of energy, $E_{\text{rel}} = E_{\text{kin}} + E_{\text{int}}$ is constant during TOF. All energies plotted are per-particle.

and λ_i and ω_i are the scale factor and trap frequency, respectively, along the i^{th} axis. These quantities are plotted as a function of TOF in Figure 6.4.

When calculating E_{rel} from absorption images, we also need to consider the accuracy of atom counting as a function of cloud density. For reasons unknown, our imaging system saturates at optical densities ≥ 4, so we need to image at longer TOFs when the clouds are less dense to obtain accurate atom counts. We quantified this experimentally in Figure 6.5 where we observe a convergence in release energies at all steps with increasing TOF. Based on the results of Figure 6.4, where $E_{\text{rel}} =$ constant, these results may seem counter-intuitive, but the key is that Figure 6.5 plots E_{rel} per particle. So, the fact that E_{rel} at each step approaches an asymptotic value for increasing TOF indicates increasing accuracy in atom counting. That is, the true atom count is only obtained for long TOFs, in our experience, > 10 ms. Thus, taking into account both the conversion of interaction

to kinetic energy and the accuracy of measured atom number, we chose to image after 12 ms of TOF.

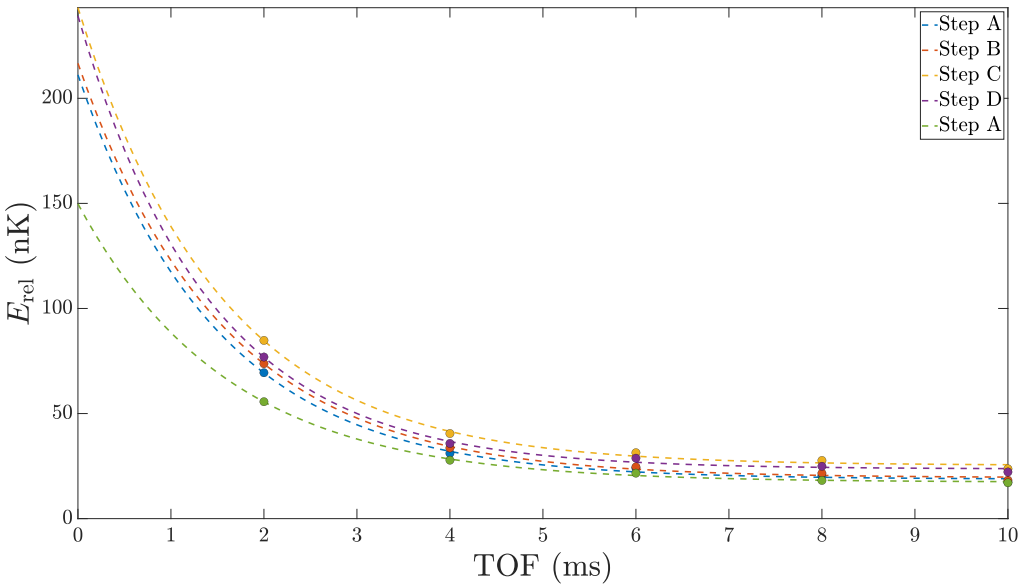

Figure 6.5: Convergence of E_{rel} per particle at each step with increasing TOF, demonstrating the need to image after long TOFs to ensure accurate atom counting.

While in principle one can numerically time-evolve the equations governing the behavior of the scale factors for each axis given in 6.4.1, we found that the cloud sizes and scale factors predicted by this method still did not result in release energies that matched simulations or analytics, though the results were closer than before. This motivated us to take side images of every step for every cycle to obtain accurate scale factors for the cycles we were performing. The final winning formula to get an accurate release energy was to top and side-image every cloud, normalizing the y and z scale factors to the x-size, and then perform the inverse Abel transform and calculate the release energy.

6.5 Engine performance

With an understanding of the data analysis process, we can now look quantitatively at the results of our experimental investigation of a thermodynamic engine using a quantum degenerate working fluid and make a direct comparison to the performance observed using a classical working fluid.

6.5.1 Quantum versus classical working fluid

To establish a quantitative advantage in engine performance when using a quantum degenerate working fluid, we execute the cycle shown in Figure 6.6(a) using a BEC. The color indicates the total energy per particle computed from finite-temperature analytics, and representative absorption images after 12 ms of time-of-flight are shown in the top panel of (b). The middle panel of (b) shows the trap frequency and scattering length ramps over the cycle using the linearization techniques discussed previously. An analogous cycle is performed using a thermal gas, with the same absolute values of scattering length as in (a) but different absolute trap frequencies. However, the compression ratio ν is the same for both the condensed and thermal clouds. The bottom panel of Figure 6.6(b) demonstrates distinctly different behavior for each type of working fluid, where the energy evolution of each gas is normalized by the measured release energy at step A: the thermal gas (squares) evolution is symmetric within error and has a calculated efficiency consistent with zero, as shown in the inset, indicating that the thermal gas does not mediate a transfer of energy between magnetic and optical fields. That is, the work performed on the cloud by the laser field in stroke AB is the same as the work done by the cloud on the field in stroke CD. Additionally, the lack of change in release energy over field ramp strokes BC and DA agrees with our expectation that the gas is behaving classically due to its dilute nature. This results in negligible changes in interaction energy

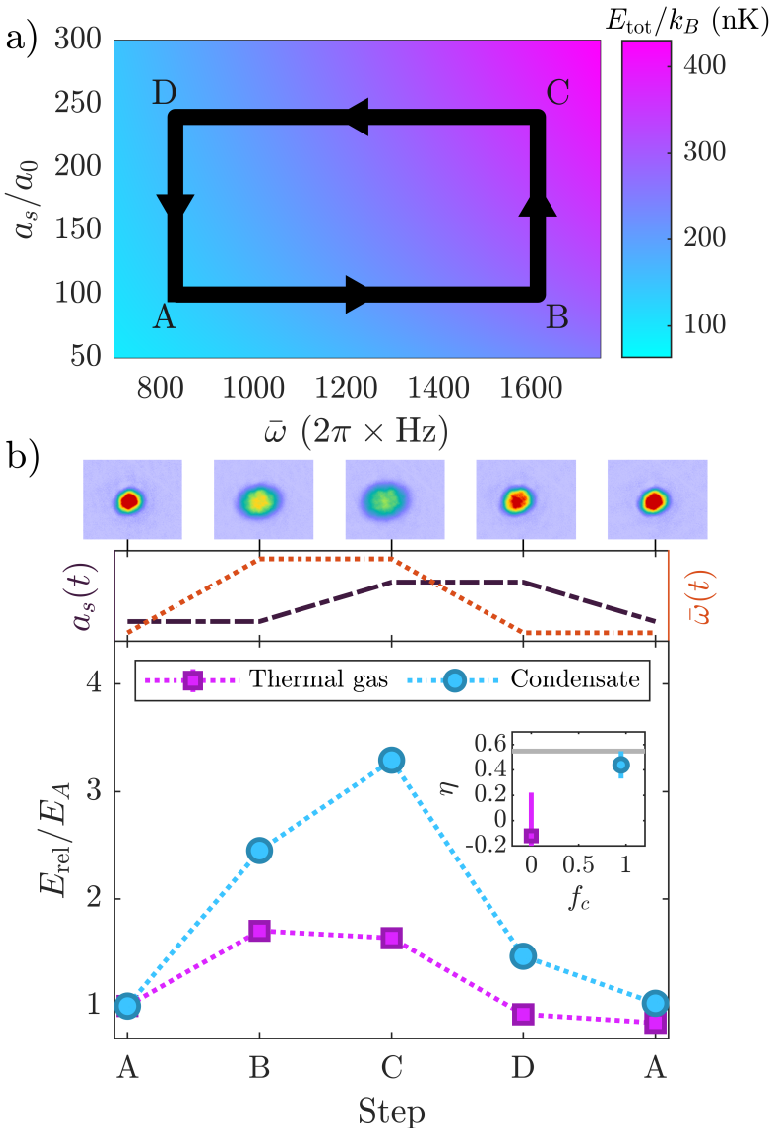

Figure 6.6: Thermodynamic engine with a quantum degenerate working fluid. (a) Engine cycle in a_s-$\bar{\omega}$ space. Color shows total energy per particle. (b) Top: BEC images after 12 ms of expansion at each step. Middle: Evolution of trap frequency (dotted) and scattering length (dot-dashed). Bottom: measured release energies for quantum degenerate (circles) and thermal (squares) working fluids during one engine cycle, normalized by the step A value. Dotted lines connect data points. Inset shows efficiency for each condensate fraction f_c; line indicates theoretical maximum efficiency in the Thomas-Fermi regime. Error bars show standard error.

as the s-wave scattering length is enhanced or suppressed. For the thermal cloud, the extracted condensate fraction f_c is consistent with zero, as expected.

In contrast, the energy evolution of the condensate shows that the change in E_{rel} differs for each stroke. The larger change in E_{rel} in stroke CD (trap relaxation) than stroke AB (trap compression), along with the smaller change between strokes DA (interaction suppression) and BC (interaction enhancement), reveal a net transfer of energy from magnetic to optical fields. The measured efficiency, shown in the inset, is consistent with the value predicted under the Thomas-Fermi approximation. Unlike the thermal gas, the condensate experiences a significant change in energy as the scattering length is ramped via the magnetic field, which can be attributed to the density of the condensate being about 33 times larger than the thermal cloud. This increase in density is a direct consequence of bosonic quantum statistics and it allows the condensate to mediate meaningful energy transfer between two otherwise decoupled fields.

6.5.2 Reversibility and repeatability

To determine whether or not the cycle is isentropic, we next characterize the reversibility by performing the same cycle in the forward (A-B-C-D-A) and reverse (A-D-B-C-A) directions and making an additional comparison to fully-interacting approximation-free numerics, as shown in Figure 6.7(a). We observe that the release energies of the forward and reverse cycles are very similar at each, indicating a high degree of reversibility. Further, our findings demonstrate that reversal of the cycle results in a net energy transfer from optical to magnetic fields, which is opposite to the forward cycle and supports our claim that the condensate acts as a working fluid to mediate energy transfer without meaningful net absorption of energy over a cycle.

We confirm the repeatability of the cycle by performing four cycles in succession, as shown in Figure 6.7(b), and we see a consistent return of the condensate to its initial release energy. Deviations from the simulations shown by the black line are largely a

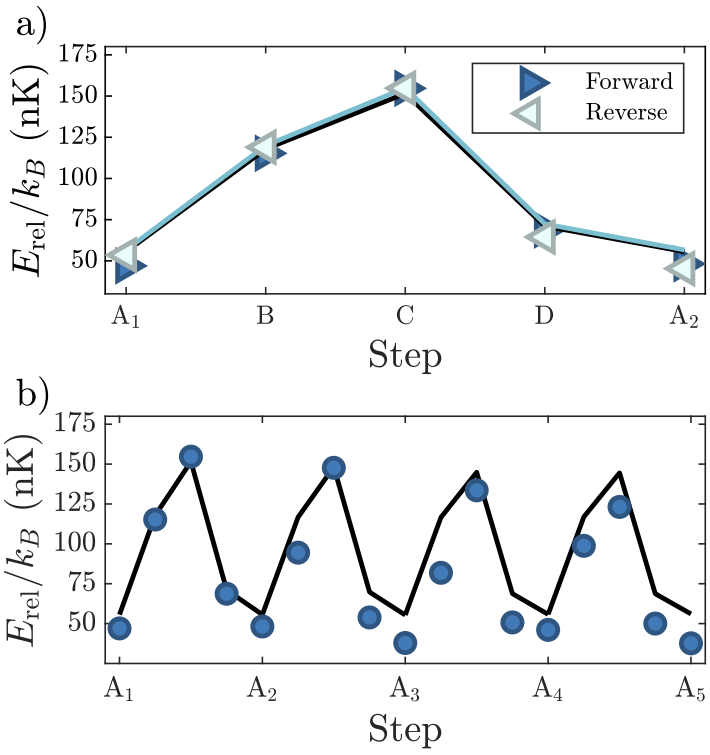

Figure 6.7: Engine reversibility and repeatability. (a): Comparison of the cycle performed in the "forward" (*A*-*B*-*C*-*D*-*A*) and "reverse" (*A*-*D*-*C*-*B*-*A*) directions, indicated by right- and left-pointing markers respectively. Light blue line shows results of analytic calculations (see Eq. 4.27); black line shows results of isentropic fully-interacting numerical simulations in both panels. (b): Measured release energy evolution during four repeated engine cycles. Simulation particle number is set to the mean particle number across each four-step cycle. Error bars are smaller than symbol size.

consequence of three-body loss over the course of the cycle, with heating from the optical trap contributing to a lesser extent.

The last ingredient needed to show that the cycle is highly isentropic is a calculation of the degree of adiabaticity. The most relevant states of our harmonically trapped Bose gas are the ground state and the lowest-lying collective excitation, the quadrupolar "breathing" mode [66]. Applying the Landau-Zener formalism to these states, we calculate the adiabaticity parameter Θ to have a maximum value of about 0.001, which is much smaller than unity where the dynamics become significantly non-adiabatic. Having

shown reversibility, repeatability and adiabaticity, we can characterize the cycle as highly isentropic.

6.5.3 Engine performance: power and efficiency

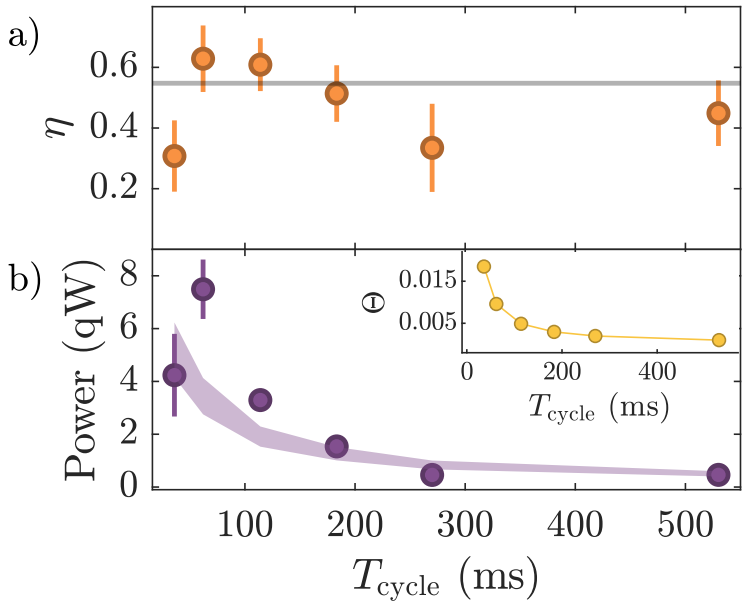

Figure 6.8: Efficiency and power vs. cycle time. (a): Measured energy transfer efficiency η versus cycle time. Line shows theoretical efficiency from Eq. 4.27. (b): Measured engine power, quoted in quectoWatts (10^{-30} Watts), versus cycle time. Shaded region shows the theoretical prediction of Eq. 4.27 for the measured range of atom numbers. The power shown here is taken from release energy measurements; as discussed in the main text, the total power is a factor of 2.5 higher. Inset shows adiabaticity parameter Θ versus cycle time.

To quantify the performance of the engine, we define the power associated with the transfer of energy between magnetic and optical fields as

$$P = -\frac{W_{AB}^{\text{las}} + W_{CD}^{\text{las}}}{T_{\text{cycle}}} \tag{6.14}$$

and the efficiency as

$$\eta = -\frac{W_{AB}^{\text{las}} + W_{CD}^{\text{las}}}{W_{BC}^{\text{mag}}}, \tag{6.15}$$

where $W_{ij}^{\text{las (mag)}}$ is the work done on the BEC by the laser (magnetic) field in stroke ij of the cycle with a total cycle time of T_{cycle}. Concretely, $W_{ij} = E_{\text{rel}}^{j} - E_{\text{rel}}^{i}$.

Intuitively, η can be understood as the amount of work done on the laser field by the condensate when the magnetic field performs a quantity of work W_{BC}^{mag} on the condensate. Similarly, the power P quantifies how much work the condensate performs on the optical field for a given cycle time.

By varying the cycle time, we can investigate the trade-off between power and efficiency, as shown in panels (a) and (b) of Figure 6.8, respectively. Using only the Thomas-Fermi approximation and assuming time independence, we predict a constant efficiency for all cycle times as excitations and dynamics are ignored. At shorter cycle times, we find that the measured efficiency is close to the theoretically predicted value, with heating and one and three-body loss degrading the performance at longer cycle times. For the shortest cycle time, the efficiency drops off sharply due to technical limitations; namely, the inability of our ODT beams to follow their PID set points for very fast ramp times, though we would also be limited by magnet current ramp rate at some point as well.

In panel (b), we compute the power for each cycle time and observe the expected inverse dependence, though for cycle times below 200 ms the power deviates from this trend. At the shortest cycle time, we again see a sharp drop-off in power, again due to technical limitations. The inset in panel (b) shows the maximum value of the adiabaticity parameter Θ for each cycle time, with the largest value being below 0.02.

What is clear from these results is that there exists an optimal range of operating parameters for the engine to achieve a desired balance between power and efficiency. In

section 6.6.1, we discuss how shortcuts to adiabaticity can potentially be used to bypass this trade-off.

6.5.4 Tuning engine performance

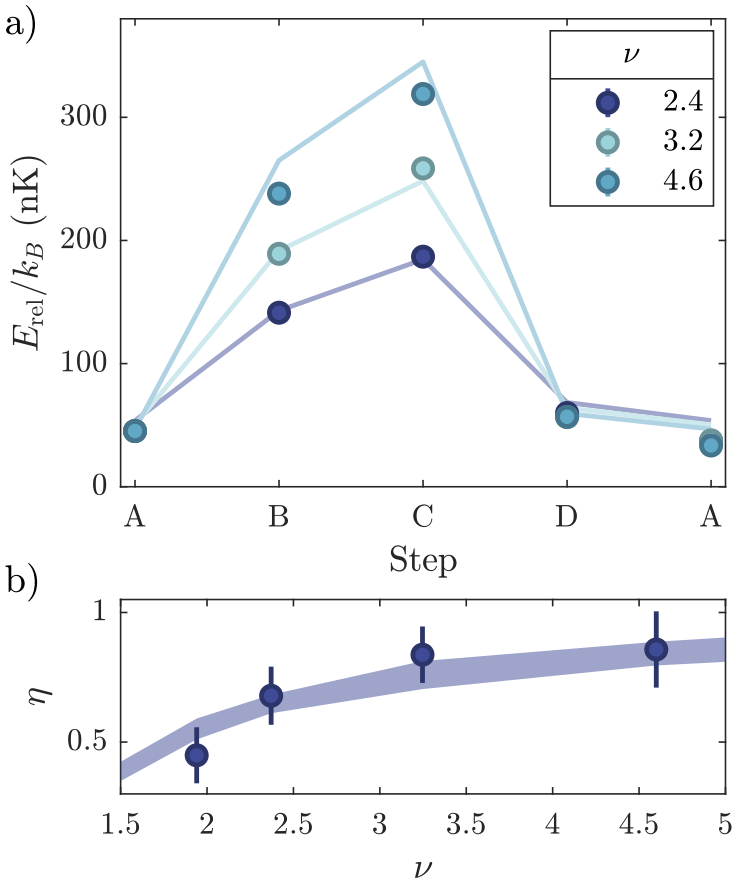

Figure 6.9: Varying compression ratio. (a): Measured release energy evolution over one engine cycle for varying $\nu = \bar{\omega}_B/\bar{\omega}_A$ at a fixed interaction ratio $\kappa = a_s^C/a_s^A = 2.4$. Lines show analytical prediction of Eq. 4.27. (b): Efficiency η as a function of compression ratio. Shaded region shows theoretical prediction of Eq. 6.20 for the measured range of atom numbers.

The efficiency and power of our engine can be tuned using the compression and interaction ratio, respectively. To show this, we again analyze the cycle in the Thomas-Fermi limit, where the total energy per particle is related to the chemical potential via

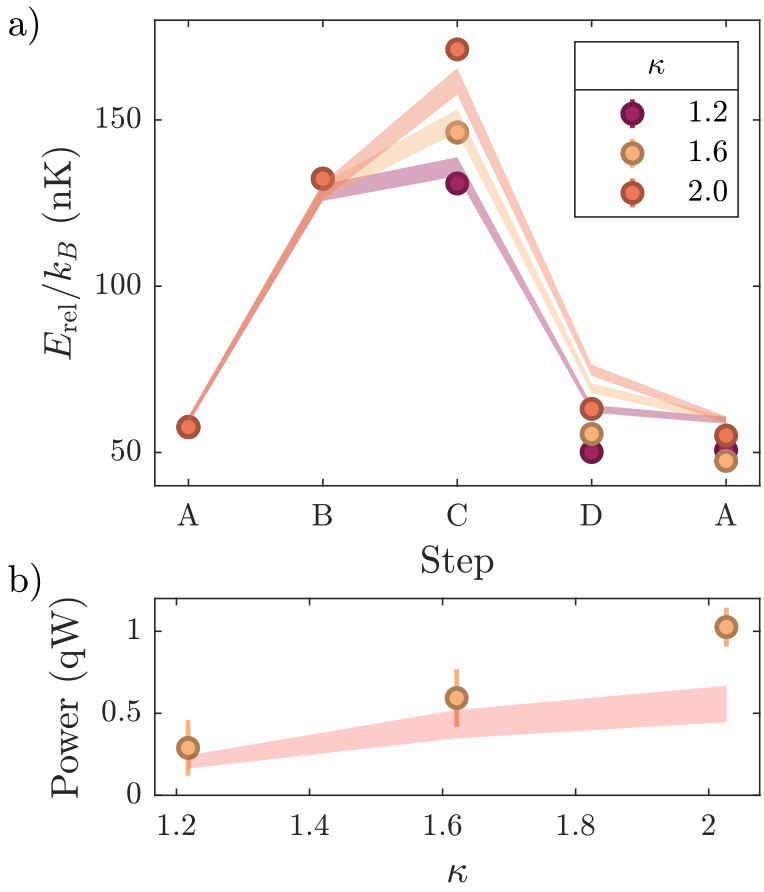

Figure 6.10: Varying interaction strength ratio. (a): Measured release energy evolution over one engine cycle for varying interaction strength ratio $\kappa = a_s^C/a_s^A$ at a fixed compression ratio $\nu = 1.94$. (b): Power output as a function of κ. Shaded regions in both panels are theoretical predictions from Eq. 4.27 for the measured range of atom numbers.

$E_{\mathrm{tot}}/N = (5/7)\mu_{\mathrm{TF}}$. First, we express the Thomas-Fermi chemical potential μ_{TF}, given by 4.12, in terms of constants, scattering length and trap frequency:

$$\begin{aligned}
\mu_{\mathrm{TF}} &= \frac{\hbar\bar{\omega}}{2}\left(\frac{15Na}{a_{\mathrm{HO}}}\right)^{2/5} \\
&= \frac{\hbar\bar{\omega}}{2}(15Na)^{2/5}a_{\mathrm{HO}}^{-2/5} \\
&= \frac{\hbar\bar{\omega}}{2}(15Na)^{2/5}\left(\frac{m\bar{\omega}}{\hbar}\right)^{1/5} \\
&= \frac{\hbar}{2}\left(\frac{m}{\hbar}\right)^{1/5}(15N)^{2/5}\,\bar{\omega}^{6/5}a^{2/5},
\end{aligned} \tag{6.16}$$

so

$$\begin{aligned} E_{\text{tot}} &= \frac{5}{7}\frac{\hbar}{2}\left(\frac{m}{\hbar}\right)^{1/5}(15N)^{2/5}\ \bar{\omega}^{6/5}a^{2/5} \\ &= C\ \bar{\omega}^{6/5}a^{2/5} \end{aligned} \tag{6.17}$$

where $C = (5/7)\frac{\hbar}{2}\left(\frac{m}{\hbar}\right)^{1/5}(15N)^{2/5}$. For a fixed particle number N, C is a constant, which we will assume is valid over the course of a single cycle. We additionally define the interaction ratio $\kappa = a_2/a_1$ and the compression ratio $\nu = \bar{\omega}_2/\bar{\omega}_1$. If we normalize the energy at subsequent steps by the energy at step A, we find that $E_A = 1$, $E_B = \nu^{6/5}$, $E_C = \nu^{6/5}\kappa^{2/5}$ and $E_D = \kappa^{2/5}$. Then,

$$\begin{aligned} W_{AB}^{\text{las}} &= \nu^{6/5} - 1 \\ W_{BC}^{\text{mag}} &= \nu^{6/5}\kappa^{2/5} - \nu^{6/5} = \nu^{6/5}(\kappa^{2/5} - 1) \\ W_{CD}^{\text{las}} &= \kappa^{2/5} - \nu^{6/5}\kappa^{2/5} = \kappa^{2/5}(1 - \nu^{6/5}) \end{aligned} \tag{6.18}$$

In terms of κ and ν, the power can be written as

$$\begin{aligned} P &= -\frac{(\nu^{6/5} - 1) + \kappa^{2/5}(1 - \nu^{6/5})}{T_{\text{cycle}}}E_A \\ &= \frac{(\nu^{6/5} - 1)(\kappa^{2/5} - 1)}{T_{\text{cycle}}}E_A \end{aligned} \tag{6.19}$$

Similarly, the efficiency can be written as

$$\begin{aligned} \eta &= -\frac{(\nu^{6/5} - 1) + \kappa^{2/5}(1 - \nu^{6/5})}{\nu^{6/5}(\kappa^{2/5} - 1)} \\ &= \frac{(\nu^{6/5} - 1)(\kappa^{2/5} - 1)}{\nu^{6/5}(\kappa^{2/5} - 1)} \\ &= 1 - \nu^{-6/5} \end{aligned} \tag{6.20}$$

So, the efficiency is completely determined by the compression ratio alone, at least in

the Thomas-Fermi limit. Thus, just as in a gasoline engine [71], one can increase the efficiency of energy transfer across the cycle by tuning the compression ratio. We also see that the dependence of power upon interaction and compression ratios gives us the ability to further optimize engine performance, and ν and κ can be tuned separately to achieve optimal efficiency and power.

The enhancement in efficiency from stronger trap compression is quantified in Figure 6.9 where panel (a) shows energy evolution for three representative cycles with different values of ν at a fixed value of κ. There is a clear and consistent trend where only the release energies of steps B and C change meaningfully, leading to an overall increase in efficiency for larger compression ratios. In panel (b), we show the measured efficiencies for all four compression ratios and observe an increase in η consistent with analytic predictions. Consistent with our Thomas-Fermi analysis, we see that the compression ratio is a key parameter of the cycle which can be used to tune the efficiency.

We perform a similar analysis by fixing the compression ratio ν and varying κ, as shown in Figure 6.10. Again, panel (a) shows energy evolution for different interaction ratios, with the more pronounced deviations from analytics at the final two steps likely due to three-body loss. The power calculated for each value of κ is shown in panel (b), where we clearly see an increase in power as interaction ratio increases and where perhaps a beyond-mean-field effect accounts for the unexpectedly large power output for $\kappa = 2$. While not a perfect match to the results of our Thomas-Fermi analysis, we do find that the power increases monotonically with κ and it is clear that the ability to tune the interaction strength ratio via Feshbach resonance is what allows for enhanced energy transfer from magnetic to optical fields.

In this work, we have created and fully characterized a novel thermodynamic engine with a quantum degenerate working fluid, and the results of this section demonstrate that power output can be enhanced independently of both boosts to efficiency achieved

through stronger trap compression and shorter cycle times.

6.5.5 Relation to the classical Otto cycle

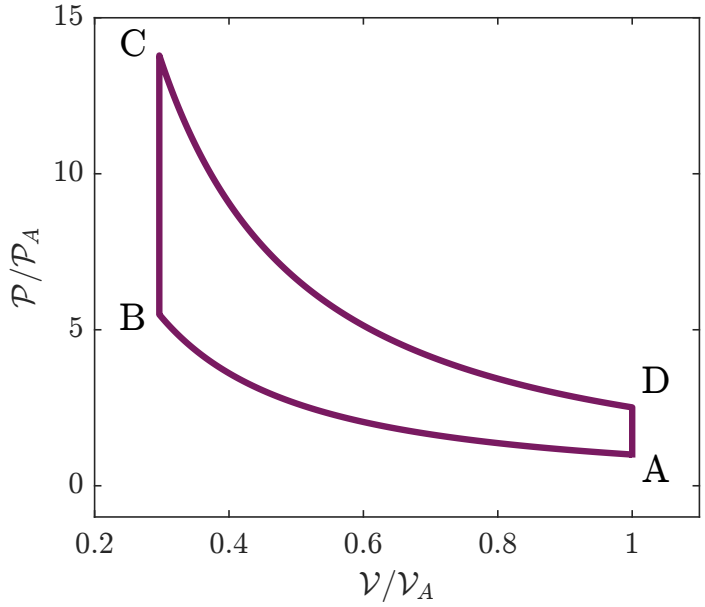

Figure 6.11: $\mathcal{PV}$ diagram for the thermodynamic engine. $\mathcal{V}_A$ and $\mathcal{P}_A$ are the harmonic volume and pressure evaluated at step A of the engine cycle. Here $\kappa = 10$ and $\nu = 1.5$.

We can demonstrate the relevance of our thermodynamic engine in the context of classical heat engines by making a direct analogy to the Otto cycle. A classical Otto cycle consists of four strokes [71]: adiabatic compression, isochoric heating, adiabatic expansion and isochoric cooling. In our cycle, adiabatic compression and expansion are replaced by adiabatic trap compression and expansion, respectively, at a fixed scattering length while isochoric heating and cooling are replaced by enhancement and suppression of interparticle scattering, respectively, at a fixed compression strength. Qualitatively, these cycles appear quite similar and we solidify the connection between them by showing how our cycle strokes directly map onto those of the classical Otto cycle.

This connection to the classical Otto cycle can be made more concrete following the approach in [72–74]. Unlike a gas confined by rigid walls, the condensate interacts with

the optical potential at all spatial positions $\mathbf{r}$ through the single-body term $U_{\text{ext}}(\mathbf{r})$. As a consequence, the volume and pressure of a BEC are understood differently than those governing the behavior of a classical gas or fluid in a rigid container. The proper thermodynamic quantities are the generalized extensive mechanical variables known as the "harmonic volume" and "harmonic pressure", with harmonic pressure being the conjugate variable to harmonic volume. The harmonic volume is defined as $\mathcal{V} = (\hbar\bar{\omega})^{-3}$ while harmonic volume is given by $\mathcal{P} = -\frac{\partial E_{\text{TF}}}{\partial \mathcal{V}}\Big|_N$. In terms of $\mathcal{V}$, we can write the total energy in the Thomas-Fermi limit as

$$\begin{aligned} E_{\text{TF}} &= \frac{5}{7} N \mu_{\text{TF}} \\ &= \frac{5}{7} N \frac{\hbar\omega}{2} \left(\frac{15 N a_s}{a_{\text{HO}}} \right)^{2/5} \\ &= \frac{5}{7} \frac{15^{2/5}}{2} m^{1/2} N \left(\frac{N a_s}{\hbar \mathcal{V}} \right)^{2/5} \end{aligned} \tag{6.21}$$

From this, we can find the harmonic pressure:

$$\mathcal{P} = -\frac{\partial E_{\text{TF}}}{\partial \mathcal{V}}\Big|_N = \frac{15^{2/5}}{7} m^{1/2} N \left(\frac{N a_s}{\hbar} \right)^{2/5} \mathcal{V}^{-7/5}. \tag{6.22}$$

With these definitions, we can then rewrite the total energy as

$$E_{\text{TF}} = \frac{5}{2} \mathcal{P} \mathcal{V}, \tag{6.23}$$

or, using the relationship $E_{\text{TF}} = (5/7) N \mu_{\text{TF}}$,

$$\mathcal{P} \mathcal{V} = \frac{2}{7} N \mu_{\text{TF}}. \tag{6.24}$$

Here, μ_{TF} plays the role of an "effective temperature" but we note that it is unrelated to

thermal equilibrium. In our cycle, strokes with constant μ_{TF} are analogous to isothermal strokes in a classical engine.

As in the classical Otto cycle, the first step of our cycle is isentropic adiabatic compression, where the trap frequency increases from $\bar{\omega}_A$ to $\bar{\omega}_B = \nu\bar{\omega}_A$ while the scattering length is held constant. From the definitions of $\mathcal{P}$ and $\mathcal{V}$, we can see that both quantities change under trap compression and this stroke is thus an adiabat in $\mathcal{PV}$ space, defined by $\mathcal{PV}^{7/5} = \text{constant}$. The second stroke enhancing interactions from a_s^B to $a_s^C = \kappa a_s^B$ only changes $\mathcal{P}$ and can thus be thought of as an "isochoric" process in which the harmonic volume remains fixed, mimicking the heating stroke of the Otto cycle. The remaining steps of the cycle follow the same reasoning above, and Figure 6.11 shows a quantitative $\mathcal{PV}$ diagram of the cycle.

Having established this analogy, the efficiency can be written as

$$\eta = 1 - \left(\frac{\mathcal{V}_B}{\mathcal{V}_A}\right)^{\gamma-1} = 1 - \left(\frac{\bar{\omega}_A}{\bar{\omega}_B}\right)^{3(\gamma-1)} = 1 - \nu^{-3(\gamma-1)} \tag{6.25}$$

which is the same as the result previously derived for an adiabatic exponent of $\gamma = 7/5$. Similarly, the efficiency of the classical Otto cycle is also determined solely by the compression ratio [71]:

$$\eta_{\mathrm{Otto}} = 1 - \nu^{1-\gamma} \tag{6.26}$$

where γ is the specific heat ratio.

6.6 Future directions

There are a number of exciting extensions to our work which are accessible to us with our current experimental setup. In a true heat engine, quantum or classical, the working fluid is coupled to hot and cold reservoirs. In the context of our thermodynamic engine,

a quantum Otto cycle can be realized if the condensate can be controllably heated and cooled. Heating the BEC is easy enough to do via trap shaking or illumination with (near-)resonant light, but to heat in a controlled manner is fairly challenging. Cooling could be accomplished through partial optical evaporation, though this results in particle loss and would limit the repeatability of the cycle.

In my opinion, the most promising prospect for realization of a quantum Otto cycle is actually the potassium experiment, which aims to create arrays of BECs trapped in optical tweezers. We can imagine three tweezers containing BECs which have undergone varying degrees of optical evaporation. The least and most evaporated clouds would serve as the hot and cold reservoirs, respectively, with the remaining cloud acting as the working fluid. Due to the programmable nature of the tweezer array, the working fluid could be brought into and out of contact with each reservoir to realize a true quantum Otto cycle.

The remainder of this section discusses a very promising future direction in detail: the use of shortcuts to adiabaticity to enhance engine performance.

6.6.1 Shortcuts to adiabaticity

One particularly interesting future direction for BEC thermodynamics on the lithium machine is the use of shortcuts to adiabaticity (STAs) to increase the power generated by the engine by decreasing the cycle time relative to a cycle which is fully adiabatic. Without the use of STAs, decreasing cycle time inevitably leads to the breakdown of adiabaticity and results in undesirable and performance-degrading excitations. STAs aim to more rapidly evolve an initial state to a desired target state while also minimizing or avoiding unwanted excitations in the process by optimizing how the control parameters of the Hamiltonian (e.g. trap frequency and scattering length) vary in time. It should be

noted that adiabaticity is not guaranteed nor is it necessarily maintained during the STA ramp protocol. The derivations shown here are reproduced from [75] which follows [76,77].

For the purposes of our cycle, we first seek the functional forms of the time-dependent trap frequencies $\{\omega_i(t)\}$ which provide a shortcut to adiabaticity at a fixed scattering length. Before deriving anything, though, we can intuit some properties of an STA compression (or relaxation) waveform from our discussion of scale factors in section 6.4.1. Namely, we know that the cloud should be at rest, i.e. not expanding, at both the initial and final trap frequencies (beginning and end of ramp, respectively). Further, the rate of expansion should also be zero at these points, so our desired STA waveform must ensure that the first and second derivatives of the scale factor along each axis are zero. We can use these boundary conditions to derive the desired waveform.

Starting from the Gross-Pitaevskii equation for a BEC in an anisotropic trap,

$$i\hbar\partial_t\Psi = \left[-\frac{\hbar^2\nabla^2}{2m} + \frac{1}{2}m(\omega_x^2x^2 + \omega_y^2y^2 + \omega_z^2z^2) + g|\Psi|^2\right]\Psi, \tag{6.27}$$

we replace the wave function with a spatial scaling function $\rho_i = i/b_i(t)$ and insert the ansatz

$$\Psi = \exp\left(-\sum_i i^2\alpha_i^2(t) - \beta_i(t)\right)\Phi(\mathbf{r},t). \tag{6.28}$$

From this, we obtain the auxiliary equation

$$\begin{aligned} i\hbar\frac{\partial\Phi}{\partial t} &= \sum_i\left(\frac{1}{2}m\omega_i^2 + i\hbar\dot{\alpha}_i - \frac{2\hbar^2}{m}\alpha_i^2\right)b_i^2\rho_i^2\Phi + \frac{g}{b_xb_yb_z}|\Phi|^2\Phi \\ &= \frac{1}{2}m\sum_i\left(\omega_i(t)^2b_i^2 + \ddot{b}_ib_i\right)\rho_i^2\Phi + \frac{g}{b_xb_yb_z}|\Phi|^2\Phi, \end{aligned} \tag{6.29}$$

where

$$\begin{aligned} \alpha_i &= -\frac{im}{2\hbar}\frac{\dot{b}_i}{b_i} \\ \beta_i &= \frac{1}{2}\ln b_i, \end{aligned} \tag{6.30}$$

and $e^{-\sum_i\left(\alpha_i+\alpha_i^*\right)i^2-\sum_i\left(\beta_i+\beta_i^*\right)} = (b_x b_y b_z)^{-1}$. Additionally, the kinetic energy term has been neglected due to the Thomas-Fermi approximation. The solutions satisfying this equation are given by

$$\ddot{b}_i + \omega_i^2 b_i = \frac{\omega_i^2(0)}{b_i^2 b_j b_k}. \tag{6.31}$$

A fifth-order polynomial of the form

$$b_i(t) = b_i(0) + [b_i(T) - b_i(0)]\left(10s^3 - 15s^4 + 6s^5\right) \tag{6.32}$$

with $s = t/T$ satisfies the following boundary conditions:

$$\begin{aligned} b_i(0) &= 1 \\ b_i(T) &= \left(\frac{\omega_{f,j}\ \omega_{f,k}}{\omega_{0,j}\ \omega_{0,k}}\right)^{1/5}\left(\frac{\omega_{0,i}}{\omega_{f,i}}\right)^{4/5} \\ \dot{b}_i(0) &= \dot{b}_i(T) = \ddot{b}_i(0) = \ddot{b}_i(T) = 0. \end{aligned} \tag{6.33}$$

Since each $b_i(t)$ is just the scale factor along each axis, these boundary conditions follow the same reasoning as in section 6.4.1. That is, the rate of expansion of the cloud $\dot{b}_i$ along the i^{th} axis should be zero at the beginning and end of the ramp, as should the "acceleration" of the expansion $\ddot{b}_i$. By definition, $b_i(0) = 1$ and the degree of compression or expansion of the cloud at time T is governed by the initial and final trap frequencies.

While it is numerically straightforward to make T small, experimental complications can arise when it becomes too small, which results in an STA ramp which requires one

or more of the trap frequencies to become negative for some amount of time during the ramp. Implementation of such a ramp would require the ability to blue-detune I THINK? the trapping beams to create an anti-trapping potential which is currently not possible on the lithium experiment. Thus, the lower bound on the ramp time T is dictated by our requirement that $\omega_i(t) \geq 0$ for all times t.

We now wish to find the form functional form of $g(t)$ which provides a shortcut to adiabaticity for a fixed anisotropic trap in the Thomas-Fermi limit. Following the treatment in [77], we start with the Thomas-Fermi ansatz

$$\Psi(r,t) = \sqrt{\frac{15}{8\pi a_x a_y a_z}\left(1 - \frac{x^2}{a_x^2} - \frac{y^2}{a_y^2} - \frac{z^2}{a_z^2}\right)} \times e^{i\left(c_x^2 x^2 + c_y^2 y^2 + c_z^2 z^2\right)}, \tag{6.34}$$

where a_i and c_i are time-dependent width and chirp parameters of the wavefunction, respectively. At time T, the Thomas-Fermi radius along the i^{th} axis is WHY

$$R_i^T := R_i(t = T) = R_i^0 \dot{a}_i(T), \tag{6.35}$$

where R_i^0 is the Thomas-Fermi radius at $t = 0$. In the Thomas-Fermi limit, the rate of expansion along each axis is the same which implies that

$$\begin{aligned} \frac{R_x^T}{R_x^0} &= \frac{R_y^T}{R_y^0} = \frac{R_z^T}{R_z^0} \\ \implies \frac{R_x^0 \dot{a}_x(T)}{R_x^0} &= \frac{R_y^0 \dot{a}_y(T)}{R_y^0} = \frac{R_z^0 \dot{a}_z(T)}{R_z^0} \\ \implies \dot{a}_x(T) &= \dot{a}_y(T) = \dot{a}_z(T) = b(T), \end{aligned} \tag{6.36}$$

and that

$$\dot{a}_x(0) = \dot{a}_y(0) = \dot{a}_z(0) = b(0). \tag{6.37}$$

The parameter $b(t)$ must then be related to the width parameters $a_i(t)$ by $b(t) = \omega_i a_i(t)$

to satisfy these boundary conditions. This leads to the equation of motion

$$\ddot{b}b\left(\frac{1}{\omega_x^2}+\frac{1}{\omega_y^2}+\frac{1}{\omega_z^2}\right)+3b^2=\frac{35\ln 2(\omega_x^2+\omega_y^2+\omega_z^2)}{2b^2}+\frac{45\omega_x\omega_y\omega_z}{4\pi b^3}g \tag{6.38}$$

which yields the expression for $g(t)$ upon rearrangement:

$$g(t)=\frac{12\pi b^5+4\pi b^4\ddot{b}\left(\frac{1}{\omega_x^2}+\frac{1}{\omega_y^2}+\frac{1}{\omega_z^2}\right)-70\pi(\ln 2)b(\omega_x^2+\omega_y^2+\omega_z^2)}{45\omega_x\omega_y\omega_z}. \tag{6.39}$$

We can use the same polynomial form 6.32 along with the following boundary conditions to find $b(t)$, and from that, $g(t)$:

$$3b(0)^4=\frac{35\ln 2(\omega_x^2+\omega_y^2+\omega_z^2)}{2}+\frac{45\omega_x\omega_y\omega_z}{4\pi b(0)}g(0) \tag{6.40}$$

and

$$3b(T)^4=\frac{35\ln 2(\omega_x^2+\omega_y^2+\omega_z^2)}{2}+\frac{45\omega_x\omega_y\omega_z}{4\pi b(T)}g(T). \tag{6.41}$$

For sufficiently small T, $g(t)$ will become negative just as $\omega_i(t)$ did, but this is perhaps less of an issue as the scattering length can be Feshbach-tuned to a negative value. It is more likely that such a short ramp would be limited by the rate at which we can change our magnetic field due to the inductance of the magnets themselves.

6.7 Conclusion

In this chapter, we have realized a thermodynamic engine with a quantum degenerate working fluid and demonstrated quantum enhancement through direct comparison to the performance of a thermal gas. We have characterized adiabaticity, repeatability and reversibility of the cycle, showing it to be isentropic and justifying the use of equilibrium

simulations, which are in quantitative agreement with experimental results. Efficiency and power have been quantified as a function of cycle time, and we have shown that efficiency and power can be tuned independently with compression and interaction ratios, respectively. We have also shown the connection between our thermodynamic engine and a classical Otto cycle through an appropriate mapping using generalized extensive thermodynamic variables. An exciting extension of our work is the use of shortcuts to adiabaticity to decrease cycle time and increase power output while maintaining efficiency.

Chapter 7

Towards continuously-trapped atom interferometery in magic Floquet-Bloch bands

7.1 Introduction

We have shown in chapter 5 that periodic driving of an optical lattice serves as a powerful tool for engineering the dynamics and transport properties of a Bose-Einstein condensate. In this chapter, we will explore how Floquet band engineering may enable the creation of noise-immune large spacetime-area atom interferometers which are continuously trapped. Many state-of-the-art interferometers operate by dropping or launching clouds of atoms into free-fall to avoid systematic phase shifts from trapping potentials. One challenge of the free-fall approach is that the sensitivity of the interferometer depends on the spacetime area enclosed by the loop [78], which can only be increased in a free-fall experiment by increasing the size of the vacuum chamber. In order to increase sensitivity, drop towers up to 100 meters tall have been and are being built so

that the free-fall time is increased. The MAGIS-100 experiment under construction at Fermilab and the *Fallturm Bremen* tower at the University of Bremen are two notable examples. Obviously, such large interferometers are very expensive and never portable. At an even greater cost, atom interferometers have been launched into space and sent to the International Space Station to operate in a microgravity environment to reach longer fall times. In contrast, continuously-trapped atom interferometry offers the possibility of large spacetime area loops without the need for huge drop towers or rockets. For this reason, there is great appeal in finding and developing an approach to making a trapped atom interferometer that has a large space-time area and is also robust to noise in the trapping potential.

In this chapter, we propose a scheme for a tunable, continuously-trapped atom interferometer with the capability of achieving space-time areas which are large compared to those accessible to tabletop free-fall experiments. It is instructive to consider the ingredients needed to make an optical interferometer, which can be simply broken down into three components: trajectories, beam splitters and mirrors. For a coherent light source, such as a laser, a beam-splitter-mirror-beam-splitter configuration creates an interferometer, with the beams in each arm traversing different paths and interfering upon recombination at the second beam splitter. As we saw in chapter 5, the position-space trajectory of atoms confined in an optical lattice is determined by the band structure of the lattice itself. We have also seen that synthesizing Floquet-Bloch band structures using periodic driving allows the trajectory to be engineered. The scheme we propose exploits this mapping between band structure and position-space motion, and harnesses the power of Floquet band engineering to create partially avoided crossings in the band structure which act as beam splitters, which are tunable using drive strength. Following the same principles, we can create mirrors in the band structure using modulation which creates fully avoided crossings. If the splitting and mirror processes do not destroy coher-

Optical interferometer	**Continuously-trapped atom interferometer**
50:50 beam splitter cube	Partially avoided crossing between Floquet-Bloch bands
Physical mirror	Fully-avoided crossing or turning point in band structure
50:50 cube to recombine	partially avoided crossing between Floquet-Bloch bands

Table 7.1: Components of a simple optical interferometer and their counterparts in a Floquet-Bloch atom interferometer.

ence, atoms interfere upon recombination, exactly analogous to the behavior in an optical interferometer. Critically, since the real-space motion of a BEC is dictated by the band structure through which it traverses [10–12], we can control the extent of spatial separation between clouds and the duration for which they remain apart. These are the fundamental ingredients we require to realize a large space-time area continuously-trapped atom interferometer. However, to overcome the challenges associated with continuously trapped schemes, we also need to develop techniques which will enhance the robustness of our interferometer to noise and fluctuations in the trapping potential.

In this vein, we draw inspiration from magic-wavelength optical lattice clock experiments where immunity to noise in the trapping potential is achieved using a particular wavelength which produces a symmetric AC Stark for both ground and excited states. The result is that the resonant frequency between these states remains unchanged in spite of fluctuations in laser intensity. An extension of this concept in the context of atom interferometers was proposed and realized by [79] in 2020. For interferometric loops composed of static Bloch bands, they identified the conditions necessary for first-order noise immunity and demonstrated enhanced robustness to fluctuations in the trapping potential at so-called magic lattice depths. Here, we extend and generalize their idea to Floquet-Bloch band interferometers and detail the process of identifying parameters to achieve first-order insensitivity noise in the lattice beam intensity. First, though, we will explore how to realize the individual components comprising a basic Mach-Zehnder-like atom interferometer, as summarized in Table 7.1.

7.2 Drive-tunable beam splitters and mirrors

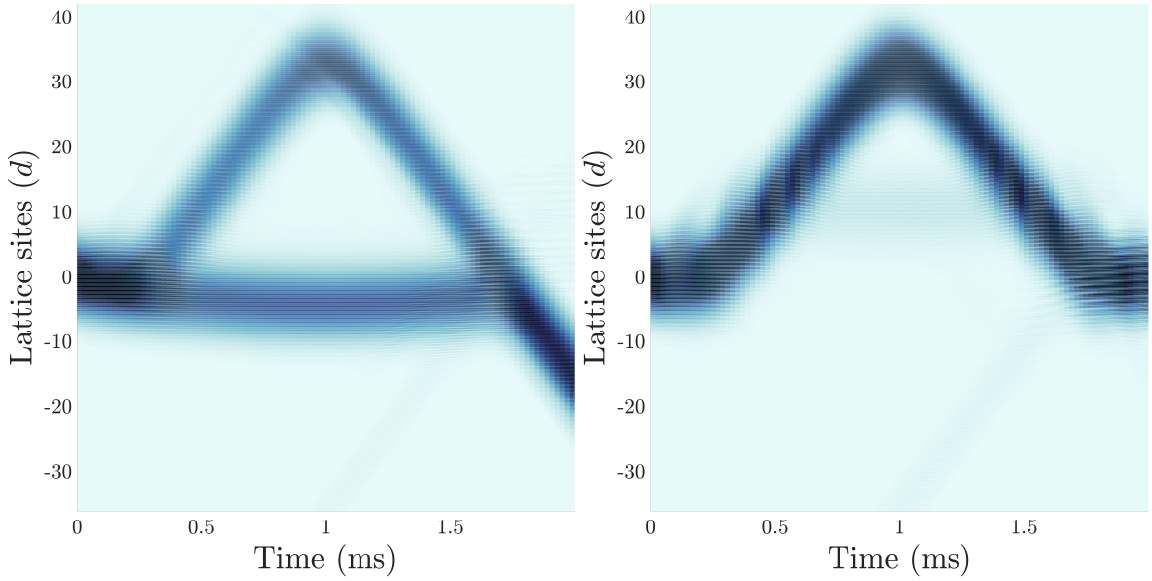

Figure 7.1: Floquet engineering of 50:50 beam splitters (left) and mirrors (right) in Floquet-Bloch bands. For both simulations, the cloud is initialized at $q_0 = 0.8\hbar k_L$ and the loop spans $q \in [0.85, 1.15]\hbar k_L$ at lattice depth $V_0 = 9.103E_R$ with Bloch period $T_B = 10$ ms and drive frequency $f = 150.765$ kHz. For the beam splitters, $\alpha = 0.0373$ while $\alpha = 0.1$ for the mirrors. The faint jets of atoms which shoot off are a result of a higher band transition for the particular parameters chosen. Residual field curvature is ignored in these simulations.

Following directly from chapter 5, we are now interested in how we can use Floquet band engineering to realize each of the key ingredients needed for an atom interferometer. Central to our scheme is the mapping between band dispersion and the position-space motion of the condensate. We have seen in chapter 5 that lattice depth, applied force, modulation frequency and modulation strength determine the real-space trajectory of a BEC, and in this way we can synthesize nearly arbitrary trajectories encompassing large space-time areas. From our previous work exploring Floquet-engineered trajectories [12], Figures 7.2 and 7.3 demonstrate synthesis of two very different trajectories. Both results confirm that the position-space motion of the condensate is determined by the dispersion

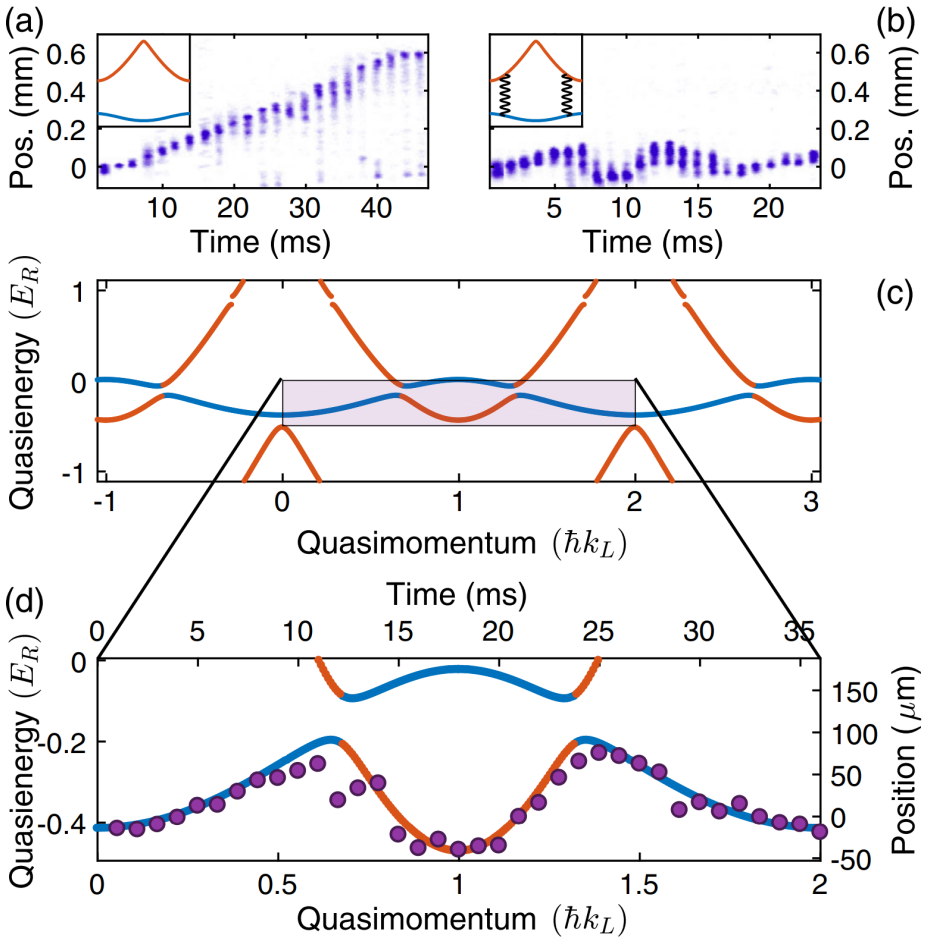

Figure 7.2: Synthesizing trajectories using Floquet band engineering. (a) Atoms evolving in a static lattice with depth of $3.6E_R$ for applied force corresponding to a Bloch frequency of 28.9 Hz. Inset shows calculated lattice band structure. (b) Position-space evolution in an s-p Floquet-Bloch band resulting from periodic modulation at $f = 56$ kHz, $\alpha = 0.25$ and $V_0 = 3.6E_R$. Inset shows same band structure as in (a) but with squiggly lines indicating locations of resonant couplings. (c) Calculated quasienergy spectrum in the extended zone scheme for the s-p hybrid band in (b). Color corresponds to the static band with maximal probability overlap with the Floquet state according to the band colors in (a). Shaded region corresponds to the mapped part of the Floquet band in (d). (d) Comparison of the real-space evolution in (b) to the Floquet spectrum in (c) according to the mapping of equation 5.22 with no fit parameters. Measurement uncertainty is smaller than plotted points. The atomic motion images the Floquet-Bloch band dispersion. Figure and caption adapted from [12].

relation of the Floquet-Bloch band which it occupies, and this capability is the first critical component in our scheme.

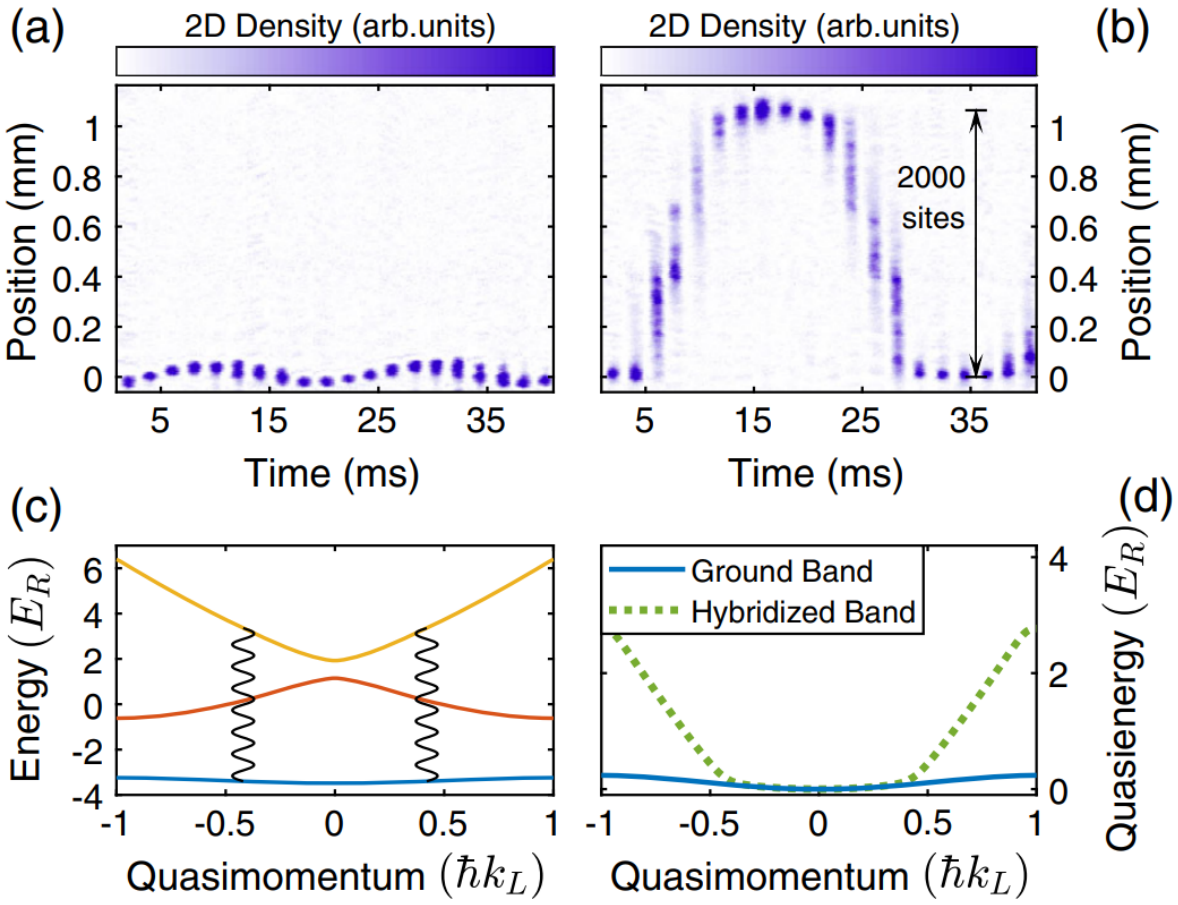

Figure 7.3: Rapid long-range transport in a Floquet-Bloch band. (a) Time sequence of images of a condensate in the ground band of a $5.4E_R$-deep lattice undergoing 48 Hz Bloch oscillations. (b) Time sequence of images of a condensate in an *s*-*d* hybridized Floquet-Bloch band created via amplitude modulation with $f = 170$ kHz and $\alpha = 0.2$, with the same initial force as in (a). Note the rapid cyclic high-fidelity transport across the trap. (c) Unmodified band structure. Vertical rippled lines indicate band coupling at the hybridizing quasimomentum for this modulation frequency. (d) Calculated dispersion of the unmodified ground band (solid line) and hybridized Floquet-Bloch band (dashed line). Figure and caption reproduced from [12].

The second key component needed is a matter wave beam splitter. The approach we take here is to exploit the avoided crossings which arise in the Floquet-Bloch band structure of a periodically driven lattice, though the avoided crossings inherent in the band structure of a static lattice can also be used; it should be noted, however, that the latter variety of avoided crossings lack the flexibility and tunability of those present

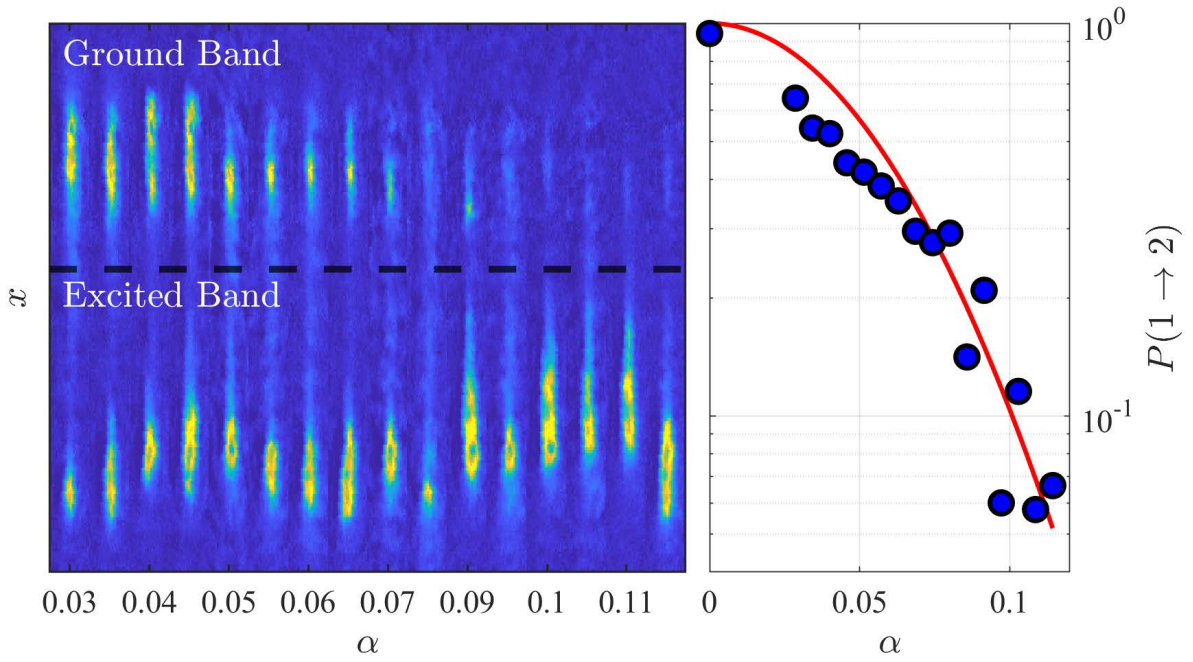

Figure 7.4: Experimental realization of tunable Floquet-Bloch beam splitter. We measure Landau-Zener interband tunneling with position-space Floquet-Bloch oscillations for varying drive strength α. The drive resonantly couples the two lowest bands. Left: absorption images taken after half of a Bloch period; population above (below) dashed line is in ground (excited) band. Right: measured relative population in ground band (blue circles) plotted against prediction of 7.1 (red curve) with no fit parameters. Here, $V_0 = 3.5E_R$, $T_B = 27.8$ ms and $\omega = 2\pi \times 55$ kHz. Reproduced from [13].

in Floquet-Bloch band structure. For each avoided crossing in a Floquet-Bloch band structure, there is an associated energy gap Δ_n between the upper and lower Floquet bands, labeled as n and $n-1$, respectively, which depends on the modulation strength α. In the Landau-Zener formalism, the probability of a particle traversing the crossing from the lower to upper Floquet band is given by [13]

$$P_{\mathrm{LZ}} = \exp\left[-\frac{\pi^2}{2}\frac{\Delta_n^2}{h f_B \frac{\partial}{\partial q}|E_n(q) - E_{n-1}(q)|}\right], \tag{7.1}$$

where f_B is the Bloch frequency, Δ_n is the gap between bands n and $n-1$, $E_n(q)$ and

$E_{n-1}(q)$ are their respective band dispersion relations and $\partial_q|E_n(q) - E_{n-1}(q)|$ quantifies the band curvature and is evaluated at $q = q^*$, the location of the avoided crossing. For smaller gap sizes, faster Bloch oscillations (larger Bloch frequencies) or "sharper" or "pointier" avoided crossings, the probability of traversal to the higher Floquet band increases. On the other hand, for larger gap sizes, slower Bloch oscillations (smaller Bloch frequencies) or "smoother" or "flatter" avoided crossings, the traversal probability is reduced. Taken together with our ability to Floquet-engineer the size of the gap using only the drive amplitude, the practical implication is that we can always find a set of modulation and force parameters so that the avoided crossing of interest results in an approximately 50:50 population split between the upper and lower Floquet bands, creating a matter-wave "beam splitter". Using a similar procedure, we can also find the modulation strength required to make a crossing fully avoided, which acts like a matter-wave "mirror". Figure 7.1 demonstrates how both beam splitters and mirrors can be synthesized by tuning only the drive strength α.

In Fall of 2019 we experimentally demonstrated this ability to tune the population split through an avoided crossing and it was a key part of our publication exploring a new method for probing non-exponential decay [13]. In the left panel of Figure 7.4, a sequence of absorption images is shown after the same hold time for different values of α and we see that the population split between bands can be tuned using only modulation strength, with a nearly full population transfer occurring for $\alpha \geq 0.09$. A quantitative analysis of these images is shown in the right panel of Figure 7.4, where the measured relative population in the ground band is plotted as a function of drive strength against the Landau-Zener prediction 7.1, showing good agreement. This demonstrates our ability to synthesize avoided crossings and tune the drive strength to create matter wave beam splitters and mirrors.

There are two choices when it comes to implementing a mirror in Floquet-Bloch

band structure. The first and simplest option is to use the symmetry of the lattice band structure itself as the mirror. This approach will work for loops which begin and end at the same absolute value of quasimomentum. A loop centered around either the zone center or zone edge guarantees that the (quasi)energy, and thus the real-space position, will return to its value at the beginning of the loop due to the symmetry of the band structure about the zone center or zone edge. The result is that both position and absolute value of quasimomentum return to their values at the beginning of the loop, which is critical in making a closed interferometer loop.

The second and more flexible way to implement a mirror is to modulate at a second frequency, different than the one used to couple two bands and create the beam splitters, to create an additional avoided crossing. Then, the modulation strength can be tuned so that the crossing is maximally avoided for the populations in each Floquet band. If we wish to mimic the π-pulses present in many atom interferometry schemes, we would instead tune the drive strength to make these crossings fully traversed. With these tools in hand, we now focus on understanding the accrual of relative phase between populations traversing different bands.

7.3 Designing interferometric loops

Floquet engineering of the effective lattice band structure via periodic driving enables flexible synthesis of loops which could serve as the basis for an atom interferometer. A suitable choice of drive frequency couples desired bands together, and the drive amplitude determines the gap between these Floquet bands and thus the degree to which these crossings are avoided. Additionally, the applied field gradient can be tuned to change the force on the atoms which, in turn, determines the Bloch period and spacetime area enclosed by the loop. Lattice depth, drive frequency, drive amplitude and applied force

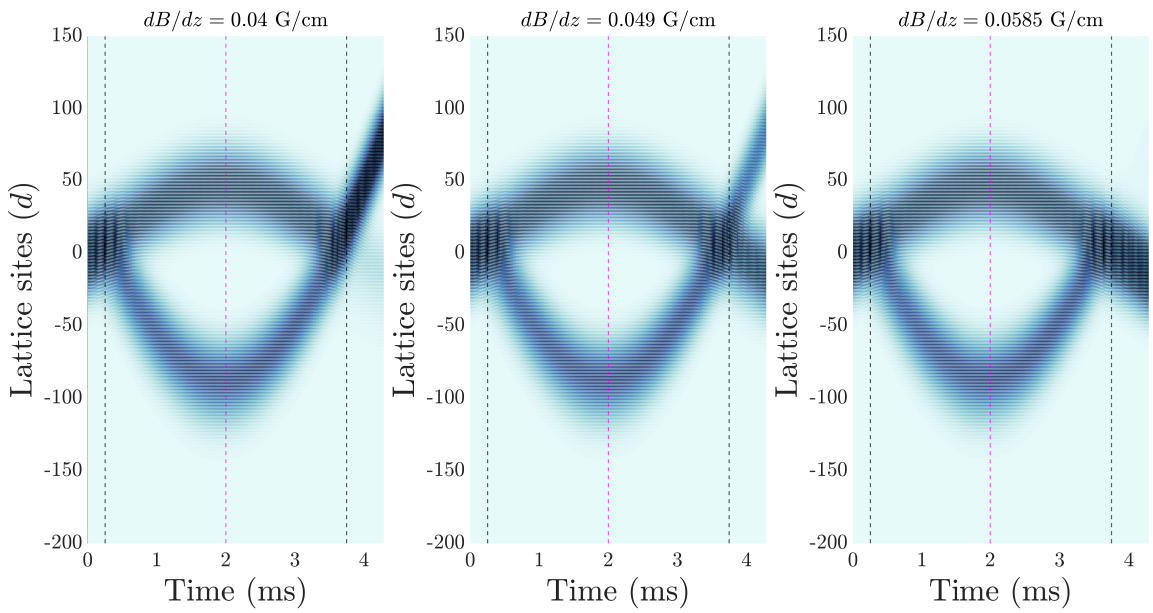

Figure 7.5: Evolution of a non-interacting BEC in an s-p interferometer loop for different applied field gradients when atoms are spatially separated. For all simulations, $V_0 = 3.32E_R$, $f = 54.792$ kHz, $\alpha = 0.0697$ and $T_B = 10$ ms. Bands are coupled at $q = 0.65\hbar k_L$ and $q = 1.35\hbar k_L$, indicated by black dashed lines. Magenta dashed lines show location of zone edge. Clouds are initialized at $q_0 = 0.6\hbar k_L$ with a spatial width of $\sigma_x = 50k_L^{-1}$ and field gradient is pulsed on between coupling points (black dashed lines) for a total duration of 3.5 ms. Lattice modulation is continuous (as opposed to pulsed) over the entirety of the loop. Field curvature is ignored for these simulations.

can all be tuned to achieve a desired loop configuration and spacetime area. The Landau-Zener probability implicitly depends on all of these parameters meaning that a certain Landau-Zener passage probability can be maintained by adjusting these parameters to compensate for a change in one of them.

Having demonstrated drive-tunable beam splitters and mirrors, we can now consider recombination of the clouds which closes the loop and is where interference between output band population occurs due to a difference in relative phase. The simplest interferometric loop we can consider is one involving only the s and p-bands, as we initialize the condensate in the s-band. If we modulate the lattice at a single frequency and with constant drive amplitude such that the cloud is split 50:50 through the first avoided cross-

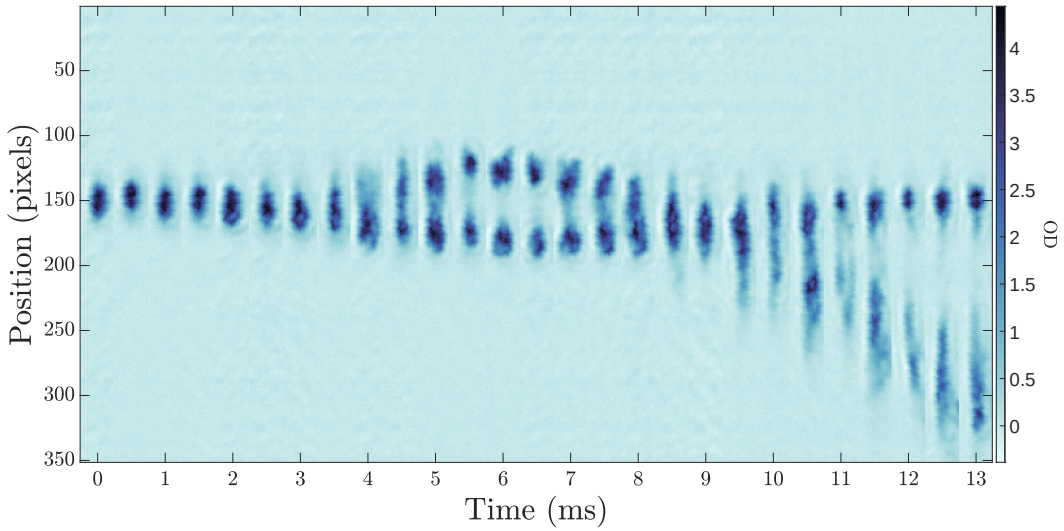

Figure 7.6: Experimental proof-of-concept of an s-p loop. Clear fringes are not observed, though structure in the output density is tantalizing. Image is constructed from a sequence of absorption images for different hold times in the lattice. Here, $V_0 \simeq 3E_R$, $f = 55$ kHz, $\alpha = 0.067$, $T_B \simeq 12.8$ ms and modulation is continuous.

ing, we have what we need for a basic loop. When using a single modulation frequency, the loop will only close if it symmetric about $q = 0$ or $q = \pm\hbar k_L$ as we are relying on the band structure of the lattice to act as the mirror to remove the complexity of adding an additional drive frequency. This is a fairly straightforward loop to simulate, and Figure 7.5 shows the results of a non-interacting 1D simulation with continuous modulation of the lattice; that is, the modulation is on for the entirety of the simulation and is not pulsed on or off. Here, the relative power in the output ports of an optical interferometer is replaced by the relative fraction of atoms in the output Floquet bands after recombination. This demonstrates that it is indeed possible to use Floquet-Bloch bands to create interferometric loops and that the underlying idea is sound; namely, that a cloud can be coherently split and recombined using our scheme, in principle allowing for the observation of interference.

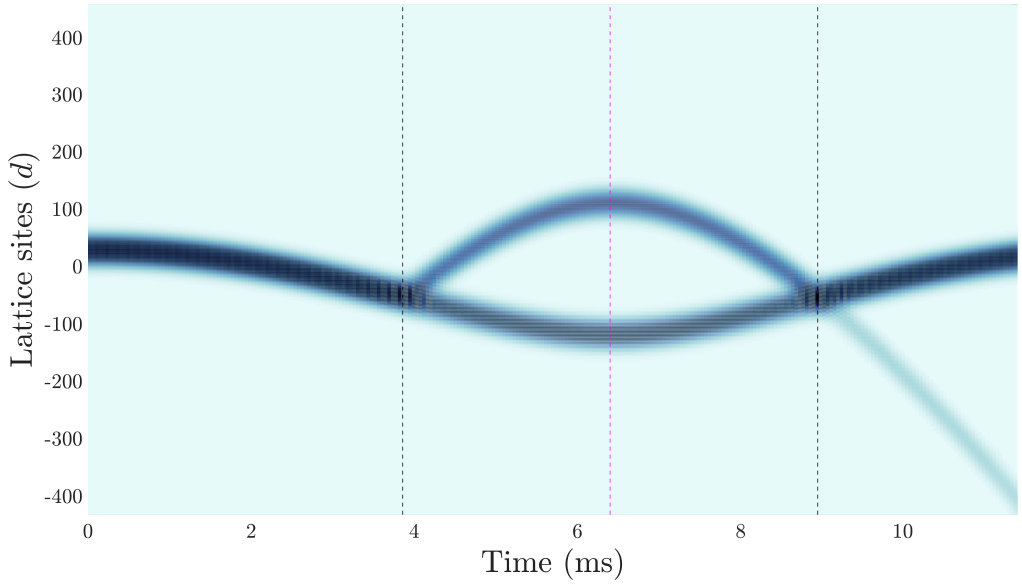

Figure 7.7: Simulated s-p loop with similar parameters to Fig. 7.6: $V_0 = 2.975E_R$, $f = 55$ kHz, $\alpha = 0.067$, $T_B = 12.8$ ms and modulation is continuous. At exactly $3E_R$, no population is visible in lower output Floquet band, so depth is set to $2.975E_R$ for better visual comparison with Fig. 7.6. Cloud is initialized at $q_0 = 0\hbar k_L$ with Gaussian spatial width $\sigma_x = 50k_L^{-1}$ and couplings between s and p-bands occur at $0.603\hbar k_L$ and $1.397\hbar k_L$. Residual field curvature is ignored here.

If this continuously-trapped atom interferometer is to be useful, we need to be able to measure something with it which requires that the quantity of interest directly affect the relative phase between clouds. Forces are often quantities of interest in sensing and navigation, so we now perform a similar simulation, this time applying a force pulse between beam splitters. As shown in Figure 7.8, if we look at the population in each band as a function of the applied force, we observe "fringes" or "oscillations" in each population as the relative phase varies from zero to 2π, modulo the Stückelberg phase, with the particular value of the phase determined by the magnitude of the applied force. This confirms that our interferometer scheme can indeed be used to measure forces and anything else which asymmetrically shifts the energies of the clouds.

To see if the simulations our expectations, we can make a back-of-the-envelope esti-

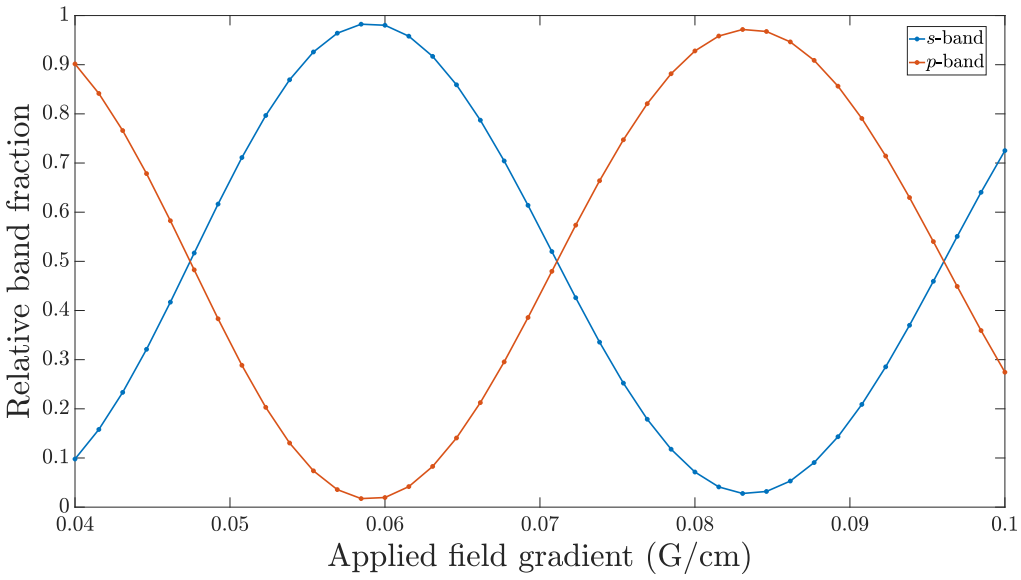

Figure 7.8: Varying applied force pulse for an s-p loop with the same parameters as in Fig. 7.5, demonstrating the high degree of sensitivity possible with our scheme. Force is generated via magnetic field gradient and is applied between beam splitters. Here, $V_0 = 3.32E_R$, $f = 54.792$ kHz, $\alpha = 0.0697$ and $T_B = 10$ ms. Bands are coupled at $q = 0.65\hbar k_L$ and $q = 1.35\hbar k_L$, clouds are initialized at $q_0 = 0.6\hbar k_L$ with a spatial width of $\sigma_x = 50k_L^{-1}$, and field gradient is pulsed on between s-p coupling points for a total duration of 3.5 ms. Lattice modulation is continuous (as opposed to pulsed) over the entirety of the loop. Residual field curvature is ignored.

mate of the relative phase which we expect to accrue. Starting with the high-field Zeeman shift

$$E_{\text{Zeeman}} = \mu_B g_J m_J B(x), \tag{7.2}$$

the corresponding force is

$$F_{\text{mag}} = -\mu_B g_J m_J \frac{\partial B}{\partial x}. \tag{7.3}$$

For the ${}^2S_{\frac{1}{2}}$ state in ^{7}Li, $g_J \sim 2$ and $m_J = 1/2$, so

$$F_{\text{mag}} = -\mu_B \frac{\partial B}{\partial x}. \tag{7.4}$$

Thus, in addition to the relative phase which accumulates due to differing band energies

which we discuss in the next section, we expect the force from the field gradient to result in an energy difference between band populations of approximately

$$\begin{aligned} \Delta E_{\text{mag}} &= F_{\text{mag}} \Delta x \\ &= -\mu_B \frac{\partial B}{\partial x} \Delta x. \end{aligned} \tag{7.5}$$

Then, if the relative phase difference is given by

$$e^{-i\Delta\phi} = e^{-i\Delta E_{\text{mag}} T/\hbar}, \tag{7.6}$$

we have that $\Delta\phi = \Delta E_{\text{mag}} T/\hbar$, or $\Delta\phi/(2\pi) = \Delta E_{\text{mag}} T/h$, where T is the duration of the loop. Now, let's use this to estimate the value of the field gradient which corresponds to 2π of relative phase difference. Assuming $\Delta x = 50d$, where d is the lattice constant, taking the loop time to be $T = 5$ ms, and using the absolute value of ΔE_{mag} we have

$$\begin{aligned} |\Delta E_{\text{mag}}| T/h &= 1 \\ \mu_B \frac{\partial B}{\partial x} \Delta x &= \frac{h}{T} \\ \frac{\partial B}{\partial x} &= \frac{h}{\mu_B T \Delta x}, \end{aligned} \tag{7.7}$$

from which we find that $\frac{\partial B}{\partial x} \approx 0.054$ G/cm. In other words, a full 2π radians should wind if the field gradient is scanned from zero to 0.054 G/cm. This rough estimate of the force sensitivity is remarkably consistent with the results shown in Figure 7.8, in which the phase winds by 2π as the field gradient is varied over a similar range.

A key advantage of our scheme is that there is no fundamental limitation on the duration of time that the populations can be kept separated. Splitting and recombination are a direct result of lattice modulation, which means that recombination can be delayed by switching off the modulation after the first beam splitter. In this scenario, the Floquet-

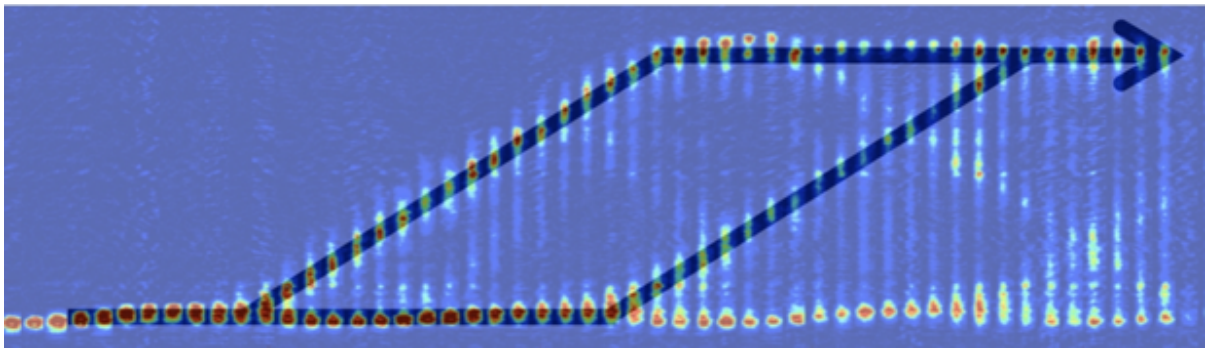

Figure 7.9: Experimental proof-of-concept of a large spacetime area s-d loop with continuous lattice modulation. Dark lines are a guide to the eye to draw an analogy with a Mach-Zehnder interferometer. Populations in both the lower and upper bands Bloch oscillate while the upper band population also undergoes simple harmonic motion in the magnetic potential. A portion of this population traverses the s-d avoided crossing back to the s-band and remains Bloch oscillating on the opposite side of the potential.

Bloch bands are projected back onto the Bloch bands of the static lattice and each cloud evolves according to the static band dispersion relations until the modulation is switched back and recombination occurs. Here, we are implicitly assuming that the projection of Floquet-Bloch bands onto Bloch bands is close to unity. Our experience with both experiment and simulations suggests that this assumption is valid for $\alpha \leq 0.2$, though it depends on avoiding resonant coupling when the modulation is switched on. Considering again the simple s-p loop described above, if we switch off the modulation after the population splits, the upper Floquet band population is mapped onto the p-band of the static lattice while the lower Floquet band population is mapped onto the s-band. Since the position-space trajectories are dictated by the band dispersions, the populations remain spatially separated until the modulation is turned back on and recombination occurs. This allows us to achieve long hold times which are limited by heating from the lattice beam and our ability to cool our magnets, rather than the force of gravity.

We can additionally synthesize loops enclosing large spatial areas, as shown in Figure 7.9. The lattice is continuously modulated to couple s to d, and d-band atoms follow a

trajectory determined by its steep curvature, resulting in long-ranged transport, similar to [12]. The dynamics in Figure 7.9 are a combination of Bloch oscillations and harmonic motion, with the latter due to the potential from the residual field curvature. The population of atoms which avoids the crossing remains in the ground band and undergoes Bloch oscillations with relatively small spatial amplitude (lower portion of Figure 7.9). On the other hand, atoms excited into the d-band traverse the harmonic potential and undergo simple harmonic motion, reaching the turning point on the opposite side of the potential. Since the driving is continuous, these atoms also traverse the s-d avoided crossing at the turning point and some transition back to the s-band, where they subsequently Bloch oscillate on the opposite side of the potential. This accounts for the atoms which remain even after the turning point is reached (upper portion of Figure 7.9). Our experiment demonstrates the large spatial areas that can be realized using Floquet band engineering. In principle, the large spacetime areas accessible through band engineering make it possible to design a highly sensitive interferometer which is relatively compact and which does not require tall drop towers or a microgravity environment to make precision measurements.

7.4 Phase accumulation between band populations

Having demonstrated that Floquet-Bloch bands can be used to engineer the basic ingredients of an interferometer, it is important to now consider how traversal of different bands manifests itself quantum mechanically; that is, we want to determine how the relative phase difference accumulates for populations in different bands. A rather generic expression for the phase is given by

$$\Delta\phi = \frac{1}{\hbar}\int_{t_1}^{t_2} \left[E_j(t) - E_i(t)\right]\ dt. \tag{7.8}$$

For the purposes of calculation, it is often easier to think in terms of quasimomentum, so we use the sloppy math trick of writing $dt = \frac{\mathrm{d}t}{\mathrm{d}q} dq$, recalling that quasimomentum changes by $2\hbar k_L$ over a single Bloch period T_B, and approximating $\frac{\mathrm{d}t}{\mathrm{d}q} \approx \Delta t/\Delta q = T_B/(2\hbar k_L)$, which allows us to rewrite the phase as

$$\Delta\phi = \frac{T_B}{2\hbar} \int_{q_1}^{q_2} \left[E_j(q) - E_i(q)\right] \, dq, \tag{7.9}$$

where the factor of $\hbar k_L$ has been absorbed into the integral to make dq dimensionless. For the same reason, we scale $E_i(q)$ and $E_j(q)$ by the recoil energy E_R to obtain

$$\Delta\phi = \frac{E_R T_B}{2\hbar} \int_{q_1}^{q_2} \left[E_j(q) - E_i(q)\right] \, dq \tag{7.10}$$

or

$$\frac{\phi_S}{2\pi} := \frac{\Delta\phi}{2\pi} = \frac{E_R T_B}{2h} \int_{q_1}^{q_2} \left[E_j(q) - E_i(q)\right] \, dq = \frac{f_R T_B}{2} \int_{q_1}^{q_2} \left[E_j(q) - E_i(q)\right] \, dq \tag{7.11}$$

where $f_R = 25.2$ kHz is the recoil frequency of ^{7}Li in a 1064 nm optical lattice and it is implied that the band dispersions are now in units of E_R. This quantity is known as the Stückelberg phase and is denoted by ϕ_S [80, 81].

The rapid accumulation of the phase ϕ_S has made trapped atom interferometry quite challenging. Specifically, fluctuations in lattice intensity give rise to fluctuations in the lattice depth δV_0. In turn, these depth fluctuations change the Stückelberg phase, which is especially problematic for large spacetime-area continuously-trapped loops where the detrimental effects of noise in the trapping potential are magnified by the duration of the loop. As an quantitative example, consider an interferometric loop composed of the s and p bands, coupled very close to the zone edges, so that the hold time is roughly one full Bloch period. At a depth of $V_0 = 5E_R$ and with a Bloch period of $T_B = 10$ ms, which are

experimentally reasonable parameters, we find that $\phi_S/(2\pi) \simeq 418$. The fact that $\phi_S/2\pi$ is on the order of 10^2 carries significant technical implications when attempting to realize a trapped atom interferometer experimentally. One the one hand, this is what gives our scheme its sensitivity, but on the other, the scale of ϕ_S indicates strong sensitivity to lattice depth fluctuations. Suppose, for example, that we are varying the strength of a force applied when the atoms have split and wish to observe the effect on the band populations after the second beam splitter. Suppose also that we vary the magnitude of the applied force so that an additional relative phase between zero and 2π is accrued between band populations. To be able to resolve a "fringe" in band population as a function of applied force, the variation of ϕ_S must be small compared to 2π, and from our previous calculation, this means that ϕ_S must vary by less than 1%. If it does not, we have no hope of observing a fringe, as fluctuations in ϕ_S, primarily due to fluctuations in lattice intensity, will completely wash out the signal. This provides strong motivation for us to find a set of conditions which mitigate the effects of noise and variation in the lattice potential.

7.5 Magic lattice depths

As previously mentioned, two of the key factors which have made continuously-trapped atom interferometry challenging are noise and fluctuations in the confining potential. Our aim in this section is to develop a technique which allows us to design loops which are immune to lattice depth fluctuations to first order. That is, we want to synthesize hybrid Floquet-Bloch bands whose differential phase shift is first-order insensitive to variations in lattice depth. This concept of a so-called "magic lattice" is an extension of the work in [79], and more generally of magic optical traps, where the methodology is developed for atom interferometers in static Bloch bands. Here, we generalize their result

to the case of a driven lattice and theoretically demonstrate the enhanced robustness to noise.

Our goal is to determine the conditions for which the integrated energy difference between two bands varies only slightly for an experimentally relevant range of lattice depths. This range of depths is determined by our estimates of the intensity noise on the optical lattice. To find magic lattice depths, the first step is to choose two static bands which will comprise the interferometric loop. Next, we need to consider the range of quasimomenta encompassed by the loop. For an undriven lattice, this may be much or all of the first Brillouin zone if one is relying on avoided crossings inherent in the static band structure to act as beam splitters. However, we have seen that introducing lattice modulation allows us to create loops which contain a smaller range of quasimomenta. The quantity of interest is the mean energy difference between the bands over the relevant range of quasimomenta at a given lattice depth V_0:

$$\rho^{ij}(V_0) = \langle \Delta E_{ij}(V_0) \rangle = \int_{q_1}^{q_2} \left[E_i(q, V_0) - E_j(q, V_0) \right] \, dq, \tag{7.12}$$

where i and j are the band indices and q is quasimomentum. The lattice depth V_0 is written as an argument to emphasize that the dispersion relations for each band change with lattice depth. Here we assume that all energies and lattice depths are in units of E_R and quasimomentum is in units of $\hbar k_L$. Physically, from $\rho^{ij}(V_0)$ we can calculate the relative phase difference accrued between two populations traversing different bands i and j over the quasimomentum range $[q_1, q_2]$. This is the same as the Stückelberg phase ϕ_S, given by 7.11, which we can now rewrite in terms of $\rho^{ij}(V_0)$:

$$\frac{\phi_S^{ij}(V_0)}{2\pi} = \frac{f_R T_B}{2} \rho^{ij}(V_0). \tag{7.13}$$

Our goal is to find the conditions which make this phase insensitive to lattice depth fluctuations to first order, i.e. $\frac{\mathrm{d}\phi_S^{ij}}{\mathrm{d}V_0} = 0$. All dependence of $\phi_S^{ij}(V_0)$ upon lattice depth is contained within $\rho^{ij}(V_0)$, so the magic lattice depth which yields the desired insensitivity can be found by extremizing $\rho^{ij}(V_0)$ numerically:

$$\frac{\mathrm{d}\rho^{ij}(V_0)}{\mathrm{d}V_0} = 0. \tag{7.14}$$

Solving this equation gives the magic lattice depth V_0^* for the particular loop under consideration. Keep in mind that V_0^* is only magic for a specific pair of bands which are coupled at a particular quasimomentum; any change in modulation frequency, and thus the location of the coupling between bands, or the bands which comprise the loop will result in a different magic lattice depth. The physical implication of conducting an experiment at a magic depth is first-order insensitivity of the interferometer to fluctuations in the lattice depth itself, which may arise from changes in optical power, lattice beam alignment and more. That is, for small fluctuations in the lattice depth δV_0, the resulting change in ρ is $\delta\rho = \delta V_0(\mathrm{d}\rho/\mathrm{d}V_0) \simeq 0$. Correspondingly, $\delta\phi_S = \delta V_0(\mathrm{d}\phi_S/\mathrm{d}V_0) \simeq 0$, which achieves the desired noise immunity.

Following [79], we begin by going through the process of identifying magic lattice depths for a loop comprised of two Bloch bands of a static lattice. Let us consider loops composed only of s-band and another band, where the avoided crossings at the zone edges act as beam splitters for each loop. Thus, the limits of integration in equation 7.12 should be $-\hbar k_L$ to $\hbar k_L$, or -1 to 1 when undimensionalized, to encompass the entirety of the first Brillouin zone. Then, we can iterate over different values of the lattice depth V_0 to find the form of $\rho^{ij}(V_0)$, which we can numerically differentiate to find the magic depth V_0^* for each pair of bands. The results of this calculation are shown in Figure 7.10. The left panel, which shows the mean energy of each band as a function of depth, reveals

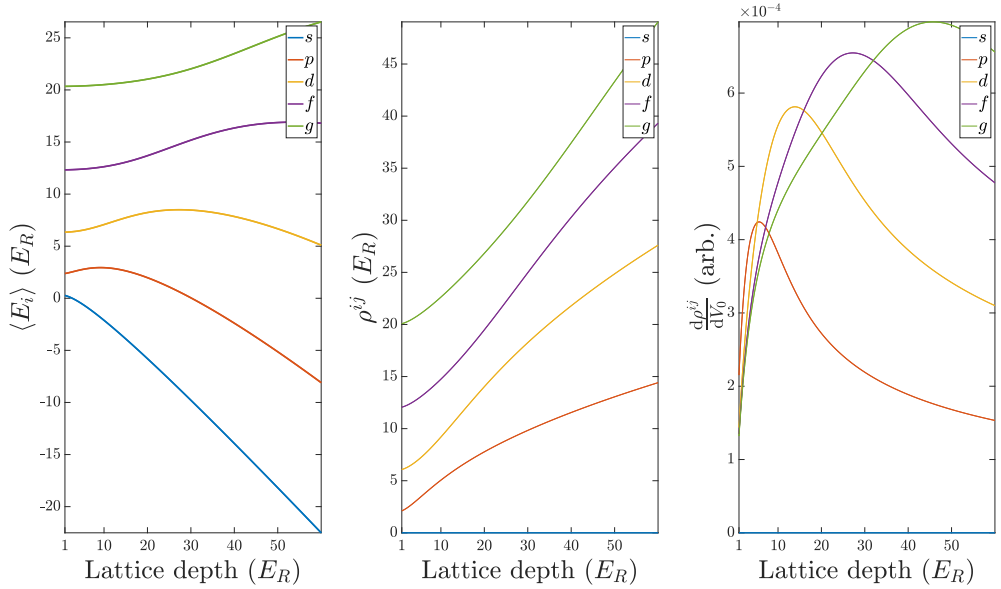

Fig. 7.10: Calculating magic static lattice depths for $q \in [-1, 1]\hbar k_L$. (a) Mean energy of each static band. (b) Mean energy difference between each band and the s-band ($i = 1$), $\rho^{1j}(V_0)$, all of which increase monotonically with lattice depth. The lack of local extrema indicate the absence of magic depths. (c) $\frac{\mathrm{d}\rho^{1j}}{\mathrm{d}V_0}$, which confirms the absence of magic depths as none of the curves reach zero, aside from the trivial case of an s-s loop. This is one demonstration of the fact that magic depths do not exist for any two-band loops where one is the s-band.

a critical piece of information: due to its monotonically decreasing energy, no magic depth exists for two-band loops which contain the s-band. This is further illustrated in the middle panel, where all $\rho^{ij}(V_0)$ are calculated with respect to the s-band. The only extrema present in these curves occur at the boundaries and do not correspond to magic lattice depths, which is shown concretely in the right panel where $\frac{\mathrm{d}\rho^{ij}}{\mathrm{d}V_0}$ is plotted for each pair of bands. None of these curves have a derivative of zero and thus no noise-immune loop can be made when using the s-band. Physically, this key result can be understood as a consequence of level repulsion in second-order perturbation theory between the s-band and all higher lying bands. This results in the monotonic decrease of the mean energy of the s-band for increasing lattice depth, and is discussed further in [79].

Given the lack of magic depths for loops containing the s-band, we repeat the calcu-

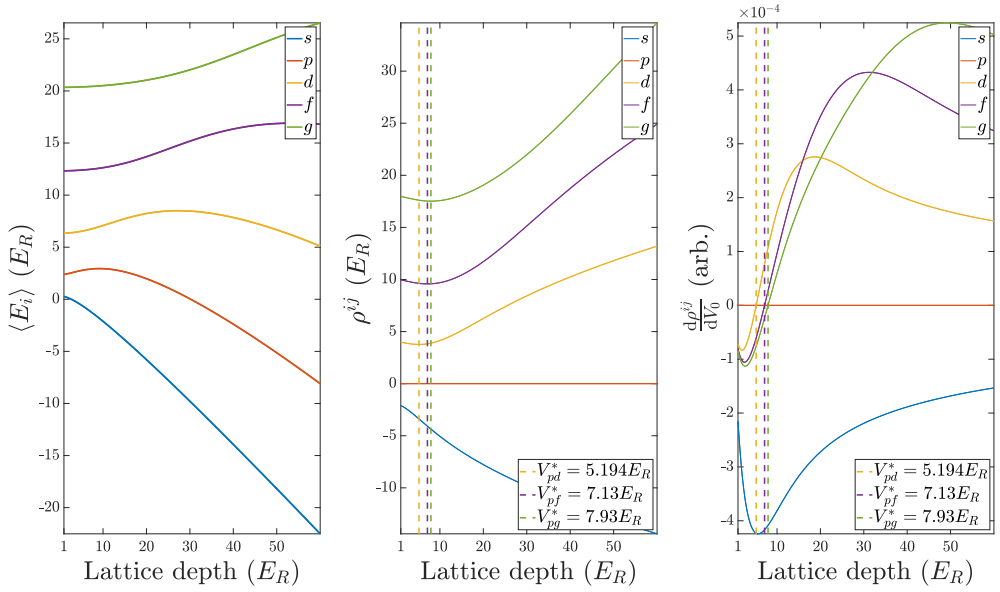

Fig. 7.11: Calculating magic static lattice depths for $q \in [-1, 1]\hbar k_L$. (a) Mean energy of each static band. (b) Mean energy difference between each band and the p-band ($i = 2$), $\rho^{2j}(V_0)$, where dashed lines indicate locations of minima. (c) $\frac{d\rho^{2j}}{dV_0}$ where dashed lines again indicate the locations of magic lattice depths (wherever the derivative is zero). Legends give the magic depths V^*_{2j} for each band pair.

lation above, this time calculating $\rho^{ij}(V_0)$ with respect to the mean energy of the p-band ($i = 2$), as shown in Figure 7.11. The mean band energies in the left panel are the same as those in the left panel of Figure 7.10, but the behavior of $\rho^{2j}(V_0)$ shown in the middle panel is dramatically different. While no local extremum in $\rho^{2j}(V_0)$ exists for the s-p loop ($j = 1$), all other band pairs have clear local minima with corresponding zero derivatives indicated in the right panel, revealing the locations of the magic depths. This same process to identify magic depths can be applied to loops spanning a smaller range of quasimomenta, which is relevant for Bloch band loops where the avoided crossings are not at the zone edges, for Floquet-Bloch band loops where the span in quasimomentum is dictated by the drive frequency, and even hybrid bands comprising multiple segments of different static bands.

In general, the process of identifying magic lattice depths becomes significantly more

involved when considering an amplitude-modulated optical lattice, as both modulation frequency and modulation strength determine the effective band structure and thus $\rho^{ij}(V_0)$, which should really be written $\rho^{ij}(V_0, \omega, \alpha)$ to reflect this fact. As α increases, the resulting Floquet bands deviate more strongly from static Bloch bands and it becomes increasingly problematic to treat the Floquet bands as portions of multiple Bloch bands "stitched" together. For experiments requiring strong driving, care must taken to account for this discrepancy and $\rho^{ij}(V_0, \omega, \alpha)$ will need to be calculated using Floquet bands rather Bloch bands, which adds complexity when finding a magic depth. However, the Floquet-Bloch loops which we have explored numerically and experimentally typically require $\alpha \leq 0.2$ to create 50:50 beam splitters, which allows us to treat these loops as portions of different static bands "stitched" together. In this way, magic depths for Floquet-Bloch loops can be found using a procedure nearly identical to the one described for static bands.

When finding magic depths for Floquet-Bloch loops, the key difference is that the range of quasimomenta is determined by the drive frequency, or frequencies, as the case may be. The lower bound of integration q_1 corresponds to the location of the first avoided crossing which splits the population while the upper bound q_2 indicates where recombination occurs. For a single drive frequency, the loop must be symmetric around either the zone center or zone edge to ensure it is closed, which means $q \in [-q^*, q^*]$ where q^* is the point at which the bands are coupled by the drive. As an example, consider a loop with two bands coupled at $q = 0.85\hbar k_L$ which, by symmetry, implies another coupling at $q = 1.15\hbar k_L$. The value of $q > \hbar k_L$ reflects the fact that we are now thinking about the loop in the extended zone scheme, but it is equivalent to treat the loop as beginning at $q = 0.85\hbar k_L$, Bragg scattering at $q = \hbar k_L$ and closing at $q = -0.85\hbar k_L$. It is often simpler to calculate $\rho^{ij}(V_0)$ in the extended zone scheme, and this is the approach we take here. With this narrower range of quasimomentum, we then perform the same

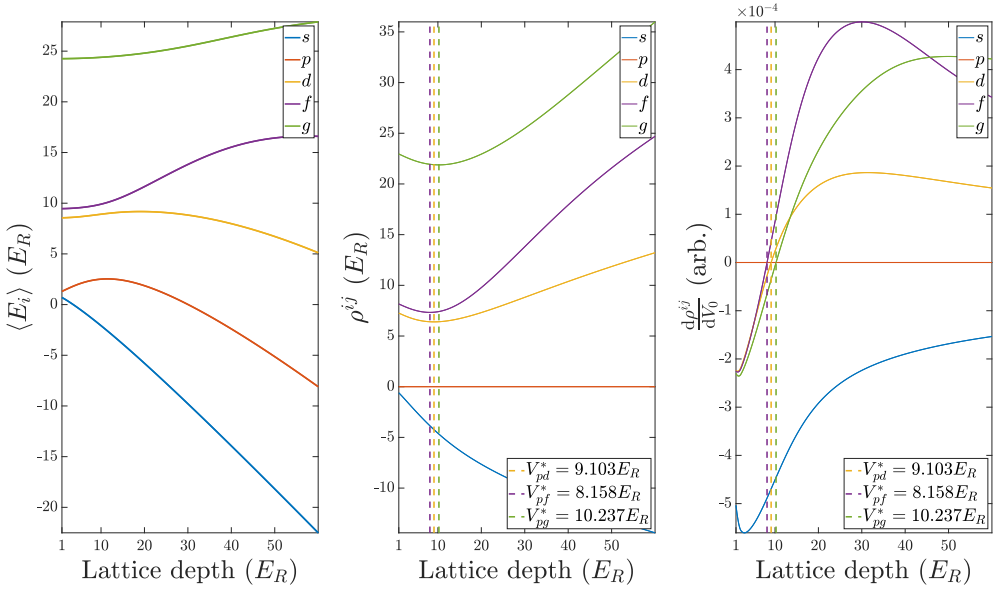

Fig. 7.12: Calculating magic lattice depths for a Floquet-Bloch loop spanning $q \in [0.85, 1.15]\hbar k_L$. (a) Mean energy of each static band. (b) Mean energy difference between each band and the p-band ($i = 2$), $\rho^{2j}(V_0)$, where dashed lines indicate locations of minima. (c) $\frac{d\rho^{2j}}{dV_0}$ where dashed lines again indicate the locations of magic lattice depths (wherever the derivative is zero). Legends give the magic depths V^*_{2j} for each band pair.

calculations that we did before with static bands, the results of which are shown in Figure 7.12. Again, the left panel shows the mean energy of each band over the range $q \in [0.85, 1.15]\hbar k_L$ with the mean energy of the s-band still monotonically decreasing with lattice depth. In the middle panel, we again compute $\rho^{ij}(V_0)$ with respect to the mean energy of the p-band and observe local minima, and thus magic depths, for all band pairs not containing s. In the right panel, differentiation of $\rho^{ij}(V_0)$ reveals the locations of the magic depths, just as before. This calculation is computationally inexpensive and allows for rapid identification of magic lattice depths for Floquet-Bloch loops.

The above calculations ignore a number of other factors which may be relevant when finding a magic lattice depth. As previously stated, we are making the assumption that the Floquet bands are well-approximated by combinations of Bloch bands. Addition-

ally, we have ignored higher order "multi-photon" interband transitions which become increasingly important as drive strength increases. Lastly, we have assumed that the entirety of the relative phase accrued between bands is due only to the differences in band energies, but other contributions to phase exist and need to be taken into account, such as the relative phase acquired during splitting and recombination. Also, due to the residual field curvature of our Feshbach magnets, the Hamiltonian of the system needs to be modified to account for this contribution, which we model as a harmonic potential:

$$\hat{H}(t) = \hat{p}^2/2m + V_0[1 + \alpha \sin(\omega t)] \cos^2(k_L \hat{x}) + \frac{1}{2} m \omega_{\text{cf}}^2 (\hat{x} - x_0)^2, \tag{7.15}$$

where ω_{cf} is the angular trap frequency due to the field curvature and x_0 is the trap center. The physical implication of this term is that our atoms actually experience a spatially-dependent force and thus have spatially-dependent Bloch frequencies, which is a potential problem for loops with large spatial separation between band populations. It is possible that this difference in Bloch frequency between band populations can prevent a loop from closing, as one population can reach its initial quasimomentum sooner than the other, and a loop can only close if both populations return to the same point in both quasimomentum and space at the same time. I have not personally observed loops failing to close in simulation, but we should remain cognizant of this possibility in future experiments. One factor which may be working in our favor is the finite (quasi)momentum width of the BEC, which may allow portions of each band population to recombine and interfere despite the presence of the curvature term.

The field gradient applied across our atomic sample to generate a uniform force and induce Bloch oscillations typically dominates over the force from residual field curvature, but if we want to model our system to the fullest extent possible in one dimension, we

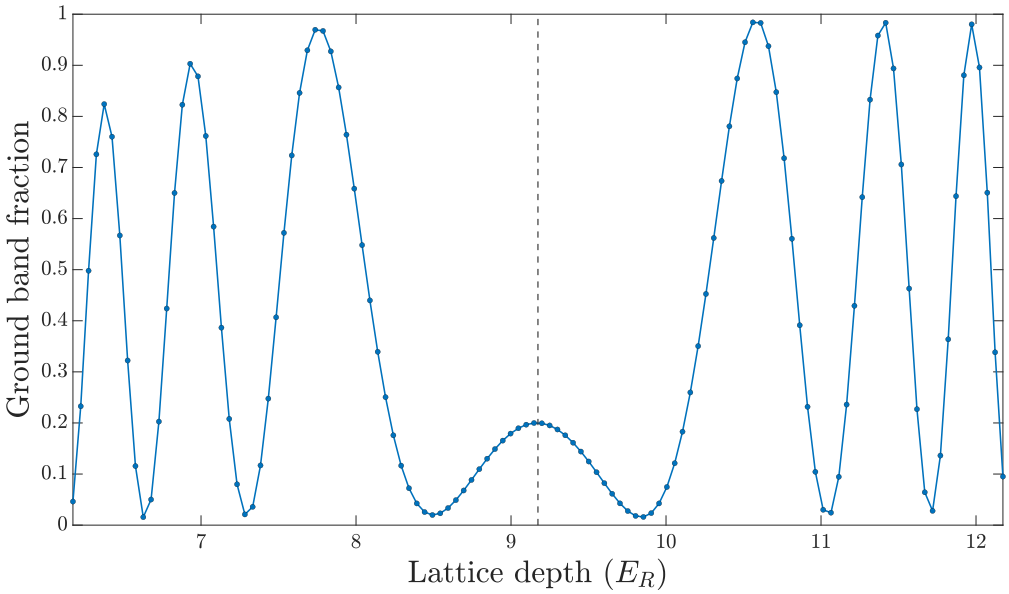

Figure 7.13: Simulated behavior of p-d Floquet-Bloch interferometer loop output versus lattice depth. For all depths, $f = 151.939$ kHz and $T_B = 7.5$ ms. At magic depth $V_0^* = 9.174E_R$ (vertical dashed line), $\alpha = 0.0434$, but for all other depths V_0^i, drive strength is rescaled via $\alpha^i = \alpha(V_0^i/V_0^*)$ to maintain roughly 50:50 population split. System is initialized at $q_0 = 0.75\hbar k_L$ with spatial width $\sigma_x = 25k_L^{-1}$ and p-d couplings occur at $q_1 = 0.8605\hbar k_L$ and $q_2 = 1.1395\hbar k_L$. In the neighborhood of magic depth $V_0^* = 9.174E_R$, ground band fraction responds weakly to changes in depth. This demonstrates first-order insensitivity of the loop to lattice intensity noise at V_0^* and indicates increased robustness. Residual field curvature is ignored and no force is pulsed; only the static force required to induce Floquet-Bloch oscillations is present.

include both terms in the Hamiltonian:

$$\hat{H}(t) = \hat{p}^2/2m + V_0[1 + \alpha \sin(\omega t)] \cos^2(k_L \hat{x}) + \frac{1}{2} m \omega_{\text{cf}}^2 (\hat{x} - x_0)^2 + F\hat{x}. \tag{7.16}$$

This is the Hamiltonian we use when performing numerical evolution of the time-dependent Schrödinger equation (TDSE), which is necessary to confirm the magic lattice depths predicted using the static band treatment. These numerical methods are discussed further in B.2. Once we have identified the approximate magic V_0^* depth using static bands, we can then perform multiple TDSE simulations for a range of depths centered around V_0^* and plot the band populations in the output arms as a function of depth. As with $\rho^{ij}(V_0)$, we are looking for local extrema in the ground and excited band populations, and an example calculation is shown in Figure 7.13 for a p-d loop. Around the magic depth of $9.174E_R$, the ground band population changes very little with lattice depth, in stark contrast to the surrounding behavior where small changes in depth result in drastic changes in population. Using TDSE to find magic depths is significantly more computationally expensive and time intensive than the static band approach, so a preliminary calculation of V_0^* using the latter method is recommended. For example, calculating the magic depth for the parameters in Figure 7.13 takes about 7 seconds, while the TDSE simulations can take a total time exceeding 20 minutes depending on the resolution of the space and time meshes.

Another useful visual can be constructed to verify that a particular lattice depth is magic. We can perform the same TDSE simulations described above around V_0^*, again looking at the populations in the output ports. This time, however, we also vary the magnitude of a force applied after the clouds split for each depth, which generates a fringe when plotting band fraction versus force. Plotting band population against applied force for all depths results in a series of fringes, and around a magic depth, the

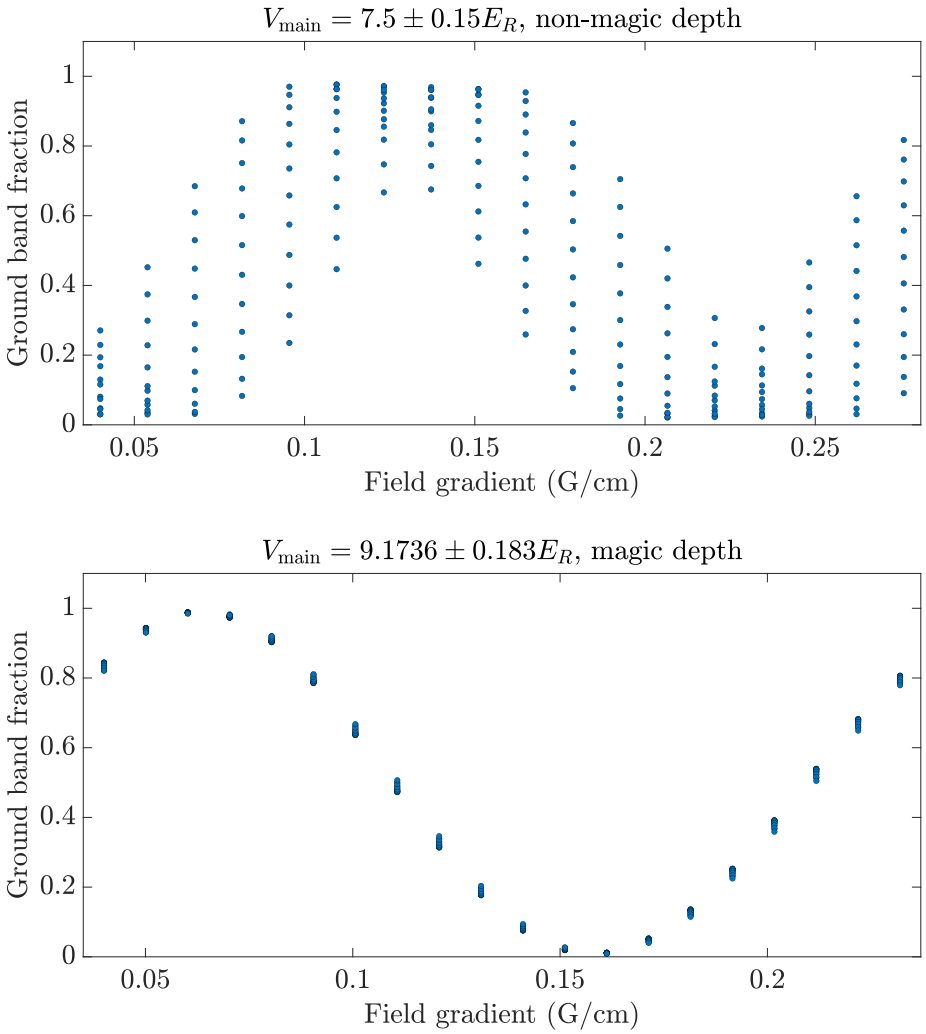

Fig. 7.14: Simulated *p*-*d* interferometer performance when varying an applied force. For each value of force, lattice depth is varied by ±2% about main lattice depth. Top: at non-magic depth $V_{\text{main}} = 7.5E_R$, slight changes in depth result in drastically different ground band fractions at the same applied force and largely wash out the signal. Bottom: at magic lattice depth $V_{\text{main}} = 9.174E_R$, fringe visibility in the ground band is maintained despite variations in depth. For non-magic loop, $V_{\text{main}} = 7.5E_R$, $f = 152.431$ kHz, $\alpha = 0.0536$ and α is rescaled for other depths via $\alpha^i = \alpha(V_0^i/V_{\text{main}})$ to roughly maintain 50:50 population split. For magic loop, $V_{\text{main}} = 9.174E_R$, $f = 151.939$ kHz, $\alpha = 0.0434$ and α is again rescaled as depth is varied. For both loops, $T_B = 7.5$ ms, system is initialized at $q_0 = 0.75\hbar k_L$ with spatial width $\sigma_x = 25k_L^{-1}$, *p*-*d* couplings occur at $q_1 = 0.8605\hbar k_L$ and $q_2 = 1.1395\hbar k_L$, and force is pulsed for 1.05 ms. Residual field curvature is ignored.

distribution of these fringes should "collapse", i.e. bunch up together, illustrating that the output of the loop remains relatively unchanged for small changes in lattice depth. A direct comparison of this "fringe collapse" behavior is shown in Figure 7.14 for magic and non-magic depths. For the non-magic loop, the signal is washed out and very sensitive to small changes in lattice depth. In stark contrast, the magic loop produces a much cleaner signal which remains robust to deviations in lattice depth, illustrating the power of operating an interferometer at magic lattice depth.

Further refinements can, of course, be made to the simulation to better predict the dynamics of the condensate in experiment. We have assumed so far that our one-dimensional simulations are valid even though the BECs we create exist in three dimensions. Due to a lack of strong transverse confinement, a 1D treatment is likely an oversimplification, and any dynamics which occur in directions transverse to the lattice are not accounted for. Additionally, assigning a fixed value of lattice depth to the entire cloud does not reflect the fact that we use a Gaussian beam to create our lattice. The Gaussian beam profile and spatial extent of the cloud result in a lattice depth which is actually a function of position and has different values for different portions of the cloud. Neither transverse dynamics nor position-dependent lattice depth have been investigated by our group so far in the context of Floquet-Bloch interferometers, so an obvious next step is to generalize the simulations to at least two dimensions so that these elements can be incorporated, with a full 3D simulation being the ultimate goal. Based on the run time of simulations in 1D, it is my recommendation that higher dimensional simulations be designed and developed to run on either local or cluster GPUs which outperform CPU-based simulations by orders of magnitude.

With the tools we have developed, we now have the ability to find magic depths for Floquet-Bloch loops and perform numerical simulations to predict and understand the dynamics. Both of these tools also help to narrow down the high-dimensional parameter

space spanned by drive frequency, drive strength, lattice depth, range of quasimomenta, Bloch frequency, and which bands comprise the loop, which is an otherwise overwhelming parameter space to explore. Let us now look at a concrete example of the steps and thought process behind designing a proof-of-concept noise-immune loop.

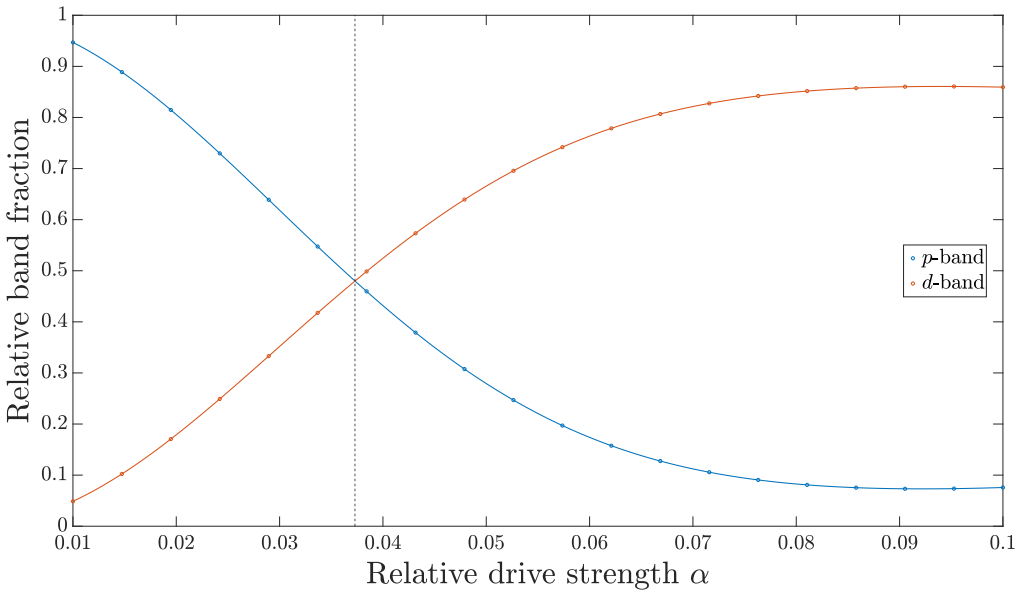

Fig. 7.15: Relative band fractions after first beam splitter in a magic p-d loop for varying relative drive strength α. An equal relative population split is achieved for $\alpha = 0.0373$ (dashed vertical line). The loop spans $q \in [0.85, 1.15]\hbar k_L$ at magic depth $V_0 = 9.103E_R$ with Bloch period $T_B = 10$ ms and drive frequency $f = 150.765$ kHz. Residual field curvature is ignored in these simulations.

Our experimental efforts so far have been quite ambitious, in retrospect. Relatively long Bloch periods, which give rise to large spatial separations between band populations, are certainly the end goal, but our initial efforts should be focused on realizing a minimally sensitive Floquet-Bloch atom interferometer in the least complicated way possible. Concretely, this means that we want to make a loop which spans a very small range of quasimomenta and has as short a duration as possible. The former can be achieved by choosing the modulation frequency so that the coupling between the desired bands is either very close to the zone center or the zone edge, or by using a second modula-

tion frequency to create a mirror. We also want to avoid higher band transitions and multi-photon resonances, as they will disrupt the desired two-band coupling. Further, we want ϕ_S to be as small as possible so that we have the best chance of resolving actual interference, which implies that the two bands in question should be close in energy over the range of quasimomentum we are considering. Depending on the particular pair of bands and the parity of each, this means that we want to make a small loop either around $q = 0$ or $q = \pm\hbar k_L$, depending on the parity. Additionally, since the dispersion of each band dictates the position-space motion of the atoms, the first experiment should utilize the lower bands which are less "steep" and which will not result in significant separation of the band populations after splitting occurs. We know that no magic depths exist for loops containing the ground band, so a *p*-*d* loop is an excellent place to start.

A key technical limitation of our apparatus is our wing coil setup, which generates a magnetic field gradient to exert a force on the atoms and induce Bloch oscillations. The magnitude of the force sets an upper bound on the Bloch frequencies (or lower bound on the Bloch periods) that we can reach. We have been able to achieve something like a 10 ms Bloch period in the past, so our shortest Bloch period will be similar to that. If our loop spans $q \in [0.85, 1.15]\hbar k_L$ in quasimomentum, it will take about $(1.15 - 0.85)\hbar k_L \cdot \frac{T_B}{2\hbar k_L} = 0.3\hbar k_L \cdot \frac{10\text{ ms}}{2\hbar k_L} = 1.5$ ms for the loop to close. We can, of course, choose a modulation frequency which results in a narrower span of quasimomentum, though we are not yet sure how small it can be made before things like the Fourier-limited width of the transition or the momentum width of the BEC become an issue.

For our *p*-*d* loop with band couplings at $|q^*| = \pm 0.85\hbar k_L$, we found the magic depth to be $V_0 = 9.103E_R$, which requires a drive frequency of $f = 150.765$ kHz, and let's assume we can achieve a Bloch period of $T_B = 10$ ms. The drive strength α needs to be chosen so that each avoided crossing acts as a 50:50 beam splitter. So far, I have found it easiest to find the corresponding value of α by performing simulations of the loop for

different values of drive strength, interpolating the results, and identifying the value of α which gives a 50:50 split after the first beam splitter. This is a rather slow method of solving for the drive strength due to the computation time, and it is quite possible that there is a more straightforward method in the literature. Note, however, that we can include relevant terms like the curve field potential in our simulations which may give us a more accurate value for α. In principle, though, if one can find the functional form describing how the gap size Δ of the avoided crossing varies with α, equation 7.1 can be inverted to solve for α without needing to do any lengthy simulations.

In Figure 7.15, the relative band fractions after the first beam splitter are plotted for different values of relative drive strength α, revealing an equal split in population for $\alpha = 0.0373$. Due to higher band transitions, there is not a point where both relative band fractions are exactly fifty percent of the initial population, but the relevant factor is that the drive strength result in the same proportion of atoms in each Floquet band, which corresponds to the point where the band fractions cross over each other, indicated by the vertical dashed line.

We have now determined all relevant parameters to create a magic *p*-*d* loop, and this process can be repeated to identify parameters for other magic loops. To summarize this process:

1. Choose the range of quasimomenta that the loop will span.

2. Choose which bands will comprise the loop.

3. Identify the approximate magic lattice depth using static band calculations.

4. Determine the drive frequency or frequencies needed to create the loop at the magic depth.

5. Plot the static band structure at the magic depth and identify any interband transi-

tions which result from driving at the necessary frequency or frequencies. Look for problematic and unwanted single and multi-photon transitions which occur inside the loop area. Revise the range of quasimomenta and repeat the above steps if the loop is not viable.

6. Choose an experimentally accessible Bloch period and perform simulations to determine the drive strengths needed to create 50:50 beam splitters and mirrors for the given depth and drive frequencies.

7. With the magic loop parameters in hand, further simulations can be done to determine force sensitivity or investigate other properties of the loop, and of course this set of parameters can be used to attempt an experimental realization.

7.6 Interaction effects on interferometer performance

Unlike many atom interferometers which utilize cold but not condensed clouds, the Bose-enhanced density of a condensate, along with the spatial confinement generated by the lattice, means that interparticle scattering cannot be neglected as interaction effects dramatically change the dynamics. The broad Feshbach resonance in ^{7}Li with an accessible zero crossing is a critical component in our scheme so that any interaction-based performance degradation can be mitigated.

To begin probing the impact of finite scattering length on interferometer performance, we can add a mean-field interaction term into the simulation with an effective one-dimensional interaction strength, given by [82]

$$g_{1\mathrm{D}} = N\frac{g}{2\pi a_\perp^2}, \tag{7.17}$$

where $a_\perp = \sqrt{\hbar/m\omega_\perp}$ is the harmonic oscillator length transverse to the lattice and

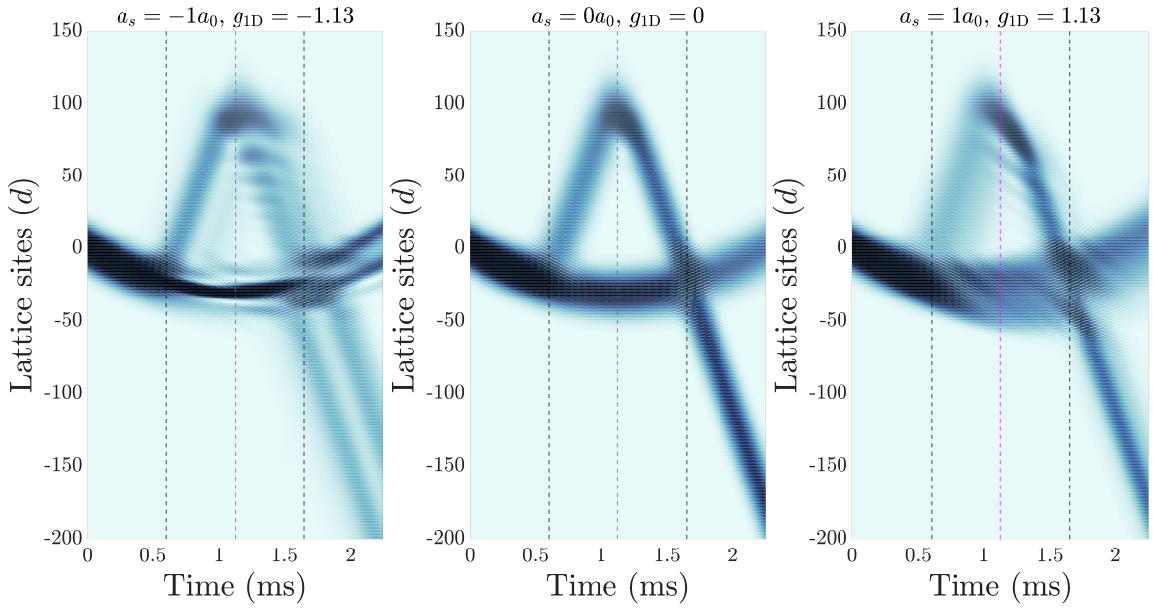

Fig. 7.16: Magic p-d interferometer degradation due to interaction effects. Left: for attractive interactions ($a_s = -1a_0$, $g_{1D} = -1.33$), we observe striations and "branching" in the cloud. Middle: for a non-interacting sample ($a_s = 0a_0$, $g_{1D} = 0$), the evolution follows the behavior predicted for a single particle in a modulated optical lattice. Right: for repulsive interactions ($a_s = +1a_0$, $g_{1D} = 1.33$), we observe broadening and "smearing" of the cloud over time. Around the zero crossing at 543.6 G, the slope is about $0.071a_0$/G, so an error of $\pm$ 14.1 G on the magnetic field would result in $a_s = \pm 1a_0$. For all interaction strengths, $V_0 = 9.174E_R$, $f = 151.939$ kHz, $\alpha = 0.0434$, and $T_B = 7.5$ ms. p and d-bands are coupled at 0.8605 and 1.1395 $\hbar k_L$ and cloud is initialized at $q_0 = 0.7\hbar k_L$ with Gaussian spatial width $\sigma_x = 25k_L^{-1}$. The one-dimensional interaction strength g_{1D} is calculated from 7.17 for $N = 10^5$ atoms and is rescaled via $g'_{1D} = g_{1D}E_R/k_L$ for consistency with the scaling used in simulation. Subplot titles give the rescaled values of g_{1D}.

N is the total atom number. This expression for g_{1D} is valid for potentials of the form $U(\mathbf{r}) = (1/2)m\omega_\perp^2(x^2+y^2)+V(z)$, where $V(z)$ is a generic potential in the axial direction, and assumes that the wave function is normalized to unity. The form of $U(\mathbf{r})$ aligns well with the potential generated by our 1D optical lattice, where the transverse confinement in x and y is approximately harmonic and the potential in z is periodic. Figure 7.16 shows the impact of interactions, where we observe the expected splitting and recombination of the cloud for a truly non-interacting sample, a "smearing out" of the cloud over

time for repulsive interactions, and a "branching off" of different portions of the cloud for attractive interactions. Additionally, due to the increased confinement of the BEC at higher lattice depths, the impact of finite scattering length is magnified and results in increased sensitivity to deviations away from zero scattering length. We have only scratched the surface with these simulations due to their one-dimensional nature and the assumptions implicit in the effective coupling constant $g_{1\mathrm{D}}$. A full three-dimensional GPE simulation would capture the dynamics in both the lattice and transverse directions and would not rely on approximations for the coupling constant, and this is likely a necessity if we want to understand and predict the behavior of the interferometer for a given set of parameters. However, even our one-dimensional simulation makes it very clear that any deviation in the s-wave scattering length away from $0a_0$ will result in drastically different dynamics over the course of the loop and make interpretation of the output confusing to interpret at best, and useless at worst. Clearly, great care must be taken to ensure that a non-interacting BEC is initialized and maintained when loading into a lattice and attempting to make a loop.

The detrimental effects of finite scattering length observed in our simulation have led us to strongly suspect that our "non-interacting" interferometry data from 2022 was actually at a finite interaction strength due to an incorrect choice of Feshbach field. An alternative or additional explanation is that the current control from our high-current supplies is insufficient, resulting in poor field control which could vary over the course of a single run, between shots, or both. This could explain why even our simplest modulated lattice experiments have always had features for which we could not account and the often inconsistent behavior observed shot-to-shot. Achieving much greater field stability through better current supplies augmented with active field stabilization electronics and current supply feedback will be critical for the success of this experiment.

7.7 Future directions and next steps

Choosing drive parameters to create a loop is quite challenging, as a number of factors require consideration, many of which are listed at the end of this chapter. Here, we focus our attention on the aspects which we have found to be addressable through experiments or numerics, namely, the impact of interaction effects and achieving first-order insensitivity to intensity noise. We explore these in the following sections, starting with the latter.

Realizing a continuously-trapped atom interferometer has proven to be quite challenging, but I am optimistic that by starting with very tiny loops which are less affected by imperfections in our experiment, we can begin collecting data which we understand and matches well to theory. My sense is, as soon as we are able to make a tiny interferometer, our subsequent experimental understanding and output will be explosive. In this section, I include a brief discussion on the future directions of the experiment followed by some ideas which have been discussed before as potentially useful in realizing our atom interferometer.

Suppose we were able to make magic depth interferometers today, what would we do with them? The ultimate goal of this project has always been to build a comparatively compact interferometer that can be used for sensing, and detection of an externally applied force with our scheme would be a great step in that direction. A small coil (or set of coils) could be mounted to the lattice axis, i.e. East-West, bucket windows and used to generate a very small magnetic field gradient which would exert a corresponding force on the atoms. Realistically, anything which asymmetrically shifts the energies of the two clouds could be used as the "field" for our interferometer. Perhaps the plug beam could be pulsed on during the loop which will shift the energies of the nearer atoms more than the further ones. Movable green beam barriers may also achieved the desired effect.

If we are unsuccessful in our attempts to make a tiny loop, we have some ideas for what to try next. We could try to make the loop with zero applied magnetic field, which would solve the issue of the residual field curvature but this might result in strange behavior due to the attractive background scattering length of $-24.5a_0$ for the $|1,1\rangle$ state. As we showed previously, interactions of any kind are detrimental to interferometer performance, but operating at zero field and low density could be worth a shot. There is also the possibility of modifying our lattice setup so that instead of a single-beam retro-reflected lattice, we use two counter-propagating beams and chirp the frequency to induce large accelerations, which would allow us to decrease the duration of the interferometer by at least an order of magnitude. One project which is already in the works and may be necessary for this experiment is the creation of transverse lattices. The confinement provided by these beams may freeze out transverse dynamics or excitations and make our system effectively one-dimensional, though it will also demand better control of our magnetic field so that our cloud is truly non-interacting, due to the increased density of the cloud. Along these lines, it is worth noting that the stronger confinement present at larger lattice depths magnifies the negative effects of finite scattering lengths, so we may wish to operate at shallower lattice depths to minimize this effect to the extent possible. To mitigate the effects of lattice beam inhomogeneity, it may also be desirable to make the beam larger with the appropriate optics. Though a larger beam requires more optical power to achieve the same lattice depth as a smaller beam, we should have more than enough power using our Azurlight laser and potentially waveplate rotators to divert more power into the lattice beam path after optical evaporation. At the time of writing, the lattice beam has been expanded for exactly these reasons which should be beneficial. Another feature of the ALS which may prove useful is the active noise reduction system (ANRS), which is supposed to drastically reduce the intensity noise of the beam. We have not yet characterized this feature, but if it works as advertised, it

could be a game-changer.

7.8 Conclusion

In this chapter, we have demonstrated the ability to synthesize drive-tunable beam splitters and mirrors via periodic amplitude modulation of the lattice. We have shown that our continuously-trapped atom interferometer scheme using Floquet-Bloch bands can in principle be used for sensing, and we have developed theoretical and numerical methods to identify lattice depths at which first-order noise immunity occurs. Further, we have demonstrated the detrimental effects of interactions on interferometer performance, which emphasizes the need for better magnetic field control. Lastly, we have discussed and recommended the next steps in realizing our interferometer, with some concluding thoughts about possible things to try which may lead to experimental success.

Appendix A

Experimental notes

A.1 Trap frequency calibration

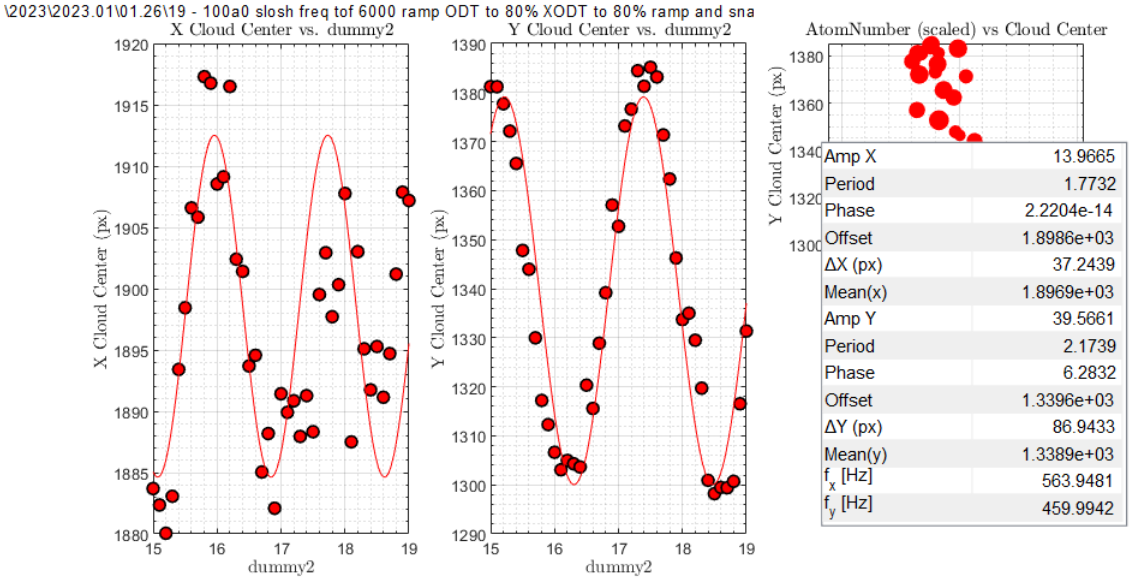

Figure A.1: An example trap frequency slosh measurement using the procedure described below. Here, we are measuring the trap frequency along the y-axis from the ODT beam. The XODT beam is not moved away and then snapped back, so the the x-axis data is not of interest here.

For the thermodynamic engine work presented in chapter 6 and for future work along those lines, we must be able to determine the trap frequency $\bar{\omega}$, in part because any movement or realignment of the ODT beams or changes in optical power and power balance between beams will also change the trap frequency. Further, we of course want to be able to set the trap frequency to achieve desired levels of compression, and we need the value of $\bar{\omega}$ for the purposes of comparison to analytics and simulations. It can also be

useful to gain intuition into how things should behave in an experiment, as many useful properties, such as the Thomas-Fermi radius, depend on $\bar{\omega}$. In this section, we detail how to perform trap frequency calibration to determine the axial trap frequencies $\{\omega_i\}$ and thus the geometric mean trap frequency $\bar{\omega}$.

Over the years, we have tried a number schemes to measure the trap frequencies along the various axes, with the underlying connection between all of them being that a fast change is made to one of the ODT beams and the resulting dynamics are observed and the frequency of oscillation of the BEC is observed and measured, giving the trap frequency of the beam which was perturbed. The best method we have found so far involves a slow ramp which changes the position of either the ODT or XODT beam followed by a snap of that beam back to its initial position, with the idea being that the cloud will be able to follow during the initial slow ramp and will not oscillate, but once the beam is "snapped" back diabatically, the cloud will slosh around just as a particle in a harmonic potential would when initialized away from the potential minimum. To better isolate the motion along each beam axis , we have found it beneficial to ramp the power higher in the non-snapped beam to suppress motion orthogonal to the main sloshing direction. Note that snapping, e.g., ODT will result in sloshing along the axial direction of the XODT beam. The general sequence for taking a trap frequency measurement is as follows:

1. After optical evaporation, ramp the powers in both ODT and XODT over the course of 10 ms. For the non-snapped beam (not the trap frequency you're trying to measure), ramp the power to somewhere around 50% of its maximum value. Ramp the beam to be snapped to the power level at which you want to measure the trap frequency.

2. Hold the powers constant while slowly moving the position of the snapped beam. Typically, we do this using a Cicero analog output and the Siglent AWGs. Depending on the maximum frequency deviation set on the Siglent, you'll want to make sure you ramp slowly enough. As a point of reference, a frequency deviation of BLANK should be done in BLANK ms, and corresponds to a shift in position of BLANK. The relevant timescale here is roughly given by $t_Q = 1/f_Q$, where $f_Q = \omega_Q/2\pi = \sqrt{2}\bar{\omega}/2\pi$, $\bar{\omega}$ is the geometric mean angular trap frequency of the dipole trap and ω_Q is the angular frequency of the quadrupolar collective excitation mode.

3. Rapidly move the beam back to its initial position by ramping the voltage from Cicero back to -7 V which will turn off the frequency modulation. If the beam is moved diabatically, the cloud will not be able to follow the trap minimum, leaving the BEC with potential energy which induces sloshing/oscillations along the beam which was displaced.

4. Hold everything constant while taking runs at varying hold times to observe the oscillatory motion and measure the oscillation, and thus trap, frequency. The best

measurements of trap frequency are typically obtained by sampling at least three full periods with roughly seven points per period.

5. Repeat this procedure as needed for both ODT and XODT at the desired power levels/PID set points.

A.2 Linearizing trap and interaction ramps

A key experimental realization was that we needed to change the ODT and field ramps in Cicero such that the resulting trap frequency and interaction ramps were linear in time. Not only is trap frequency non-linear in optical power, but in addition, the ODT power is controlled via a voltage sent from Cicero. Using measured trap frequencies and the fact that trap frequency goes as the square root of optical power, we engineered ramps for ODT and XODT which resulted in the geometric mean trap frequency changing at a rate of $\dot{\bar{\omega}} = 2\pi \cdot 1$ Hz/ms. This ramp rate was maintained for all data in the paper, i.e. for ramps to lower trap frequencies the ramp time was less and similarly for ramps to higher trap frequencies.

For the interaction ramps, we needed to account for the fact that Cicero is used to set the output of the current supplies which roughly sets the magnetic field at the atoms using known conversion factors, namely 50 Amps/Volt and about 1.72 Gauss/Amp (depends on which set of coils is being considered). However, due to the functional form of the scattering length near the Feshbach resonance, the resulting scattering length is highly non-linear:

$$a(B) = a_{\mathrm{BG}}\left(1 - \frac{\Delta}{B - B_0}\right) \tag{A.1}$$

where $a_{\mathrm{BG}} = -24.5a_0$, $\Delta = -192.3$ G, and $B_0 = 736.8$ G. Similarly, we wanted $\dot{a} = 1\ a_0$/ms to maintain a roughly constant adiabaticity parameter. Again, smaller or larger scattering lengths were reached by ramping for less or more time. To find the functional form of the ramp, we can insert $ct + d$ in place of $a(B)$ and solve for $B(t)$:

$$ct + d = a_{\mathrm{BG}}\left(1 - \frac{\Delta}{B(t) - B_0}\right) \tag{A.2}$$

$$B(t) = \frac{a_{\mathrm{BG}}\Delta}{a_{\mathrm{BG}} - ct - d} + B_0 \tag{A.3}$$

Noting that $B(t) = \alpha\beta V(t)$ where α is amps per volt, β is Gauss per amp and $V(t)$ is the voltage from Cicero, we find that

$$V(t) = \frac{1}{\alpha\beta}\left(\frac{a_{\mathrm{BG}}\Delta}{a_{\mathrm{BG}} - ct - d} + B_0\right) \tag{A.4}$$

The initial offset d is set by the starting scattering length which was $100a_0$ for the data

presented in the paper. Additionally, the Feshbach field voltage in Cicero corresponding to the resonance is 8.68 V (empirically measured), which does not align with the predicted value of 8.567 V obtained from $B_0/(\alpha\beta)$. This is potentially due to an imperfect Helmholtz coil configuration, error on the current-to-field conversion factors, an incorrectly set curve field, or some combination of these. For the data presented in the paper, the linearized field ramp waveforms were obtained using the measured resonance voltage of 8.68 V.

We can follow a similar procedure to linearize the ramp of the geometric mean trap frequency $\bar{\omega}$. The radial trap frequency of a dipole beam goes as the square root of optical power for far off-resonant light:

$$\omega_r = \sqrt{\frac{4U_0}{mw_0^2}} \tag{A.5}$$

Here, $U_0 = U(r = 0, z = 0)$ is the peak trap depth at the focus and w_0 is the beam waist at the focus. The peak trap depth U_0 is related to the optical power via [28]

$$U_0 = \left(\frac{3\pi c^2}{2\omega^3}\right)\left(\frac{2P}{\pi w_0^2}\right)\left(\frac{\Gamma}{\omega_0 - \omega} + \frac{\Gamma}{\omega_0 + \omega}\right), \tag{A.6}$$

where we have not made the rotating wave approximation since the detuning $\Delta = \omega_0 - \omega = 2\pi c(1/\lambda_0 - 1/\lambda)$ is on the order of Γ, and λ_0 and λ refer to the cycling and trapping wavelengths, respectively.

While in principle we know all parameters entering into the expression for U_0, the most direct way to determine trap frequency is to measure it using a trapped BEC and a technique like amplitude modulation spectroscopy or sloshing.

The trap frequency in the z-direction is approximately given by the quadrature sum of the x and y frequencies, $\omega_z = \sqrt{\omega_x^2 + \omega_y^2}$, since the angle between the axes of our ODT beams is about 90° . From separate measurements of ω_x and ω_y, the geometric mean trap frequency is then

$$\begin{aligned} \bar{\omega} &= (\omega_x \omega_y \omega_z)^{1/3} \\ &= \left(\omega_x \omega_y \sqrt{\omega_x^2 + \omega_y^2}\right)^{1/3} \end{aligned} \tag{A.7}$$

For $\omega_x \approx \omega_y$, the expression for $\bar{\omega}$ simplifies to $\bar{\omega} = 2^{1/6}\omega_x$. Without this simplification, linearizing $\omega_x(t)$ and $\omega_y(t)$ gives $\bar{\omega}(t)$ a functional form which is not perfectly linear, but for the measured trap frequencies and selected ramp rate $\bar{\omega}(t)$ is very well approximated by a line. From numerical explorations, $\bar{\omega}(t)$ is highly linear unless $\omega_x(t)$ and $\omega_y(t)$ have significantly different ramp rates and/or initial values.

In our trap frequency calibration analysis, we fit the data with a function of the form $a_1\sqrt{x + a_2} + a_3$ and determine the values of the a_i, and this is done separately for both ODT and XODT. In this function, x is the PID set point from Cicero for whichever

beam is being considered. The offset a_2 is used to counteract the integral error which accumulates even when the ODT AOMs are off, which is due to a non-zero signal on the ODT photodiodes despite a set point of zero. Without a_2, the beams either spike past or lag behind their set points at the beginning of the ODT ramp.

The optical power in each ODT beam is proportional to its set point, so we can replace the power $P(t)$ with the set point voltage $V_{\mathrm{PID}}(t)$ times some proportionality constant:

$$\omega(t) = A\sqrt{V_{\mathrm{PID}}(t) + B}. \tag{A.8}$$

Then, we insert the desired linear form for $\omega(t)$ and rearrange:

$$\begin{aligned} ct + d &= A\sqrt{V_{\mathrm{PID}}(t) + B} \\ V_{\mathrm{PID}}(t) &= \left(\frac{ct+d}{A}\right)^2 - B. \end{aligned} \tag{A.9}$$

The values of A and B are determined by the initial and final values of V_{PID}, which are determined in turn by the initial and final trap frequencies. That is, if $V_{\mathrm{PID}}(0)$ gives a trap frequency of ω_1 and $V_{\mathrm{PID}}(t_f)$ gives ω_2 for a ramp time t_f, we have the following boundary conditions:

$$\begin{aligned} V_{\mathrm{PID}}(0) &= \left(\frac{d}{A}\right)^2 - B \\ V_{\mathrm{PID}}(t_f) &= \left(\frac{ct_f+d}{A}\right)^2 - B. \end{aligned} \tag{A.10}$$

The solutions to this system of equations are

$$\begin{aligned} A &= \left[\frac{ct_f(2d+ct_f)}{V_2 - V_1}\right]^{1/2} \\ B &= \frac{-(d+ct_f)^2 V_1 + d^2 V_2}{ct(2d+ct)} \end{aligned} \tag{A.11}$$

which then give the functional form of the linearized trap ramp:

$$V_{\mathrm{PID}}(t) = \frac{-[(t-t_f)(2d+c(t+t_f))]V_1 + t(2d+ct)V_2}{t_f(2d+ct_f)} \tag{A.12}$$

The ramp rate c was chosen to be $2\pi \cdot 1$ Hz/ms for both beams to ensure a high degree of adiabaticity and the initial trap frequencies d were $2\pi \cdot 116$ Hz and $2\pi \cdot 120$ Hz for ODT and XODT, respectively.

A.3 Notes on imaging

To switch between imaging of large clouds at lower magnetic fields and the condensate at much higher field, we employ a de-magnification telescope whose lenses are on flip mounts. With the lenses flipped down (beam does not pass through telescope), the imaging beam is an appropriate size for the condensate. On the other hand, flipping the lenses up makes the beam much larger (covers most of the camera sensor) and allows much larger clouds to be imaged properly. However, larger beams give more scattered light and thus fringes, so there is a balance to be struck.

When taking images with the PCO, imaging light is flashed for a duration $t_{\text{image}} = 5\ \mu$s with the minimum exposure time of 10 μs set in the PCO software. Exposure auto should be disabled, shutter mode should be global reset release, trigger mode should be enabled and trigger function should be "external exposure start".

When taking images with either the side or side bucket Basler, t_{image} should be set to 60 μs CHECK in Cicero with an exposure time of 70 μs set in the Basler Pylon software. Additionally, the quality of the images can be greatly improved if the amount of imaging light is maximized, so minimizing the attenuation from either the IMC DP VVA (low-field imaging) or HF IMC DP VVA (high-field imaging) is recommended. Further, the shutter mode should be global reset release. Note that imaging low-field clouds before evapD is not possible due to the time it takes the MOT flip mirrors to flip up and allow for optical access from the East.

To image at fields different than $240a_0$, one can use either the Breit-Rabi formula or estimate the change in frequency using 1.4 MHz/Gauss at high magnetic fields where the slope in imaging frequency is approximately linear. To really pinpoint the imaging frequency, a scan of the detuning of the MOTC DP VCO is recommended which should show a maximum in atom number for some value of detuning. NOTE: the relatively long path length between the MOTC DP and input of the MOTC TA (MOGC) means that the TA is only properly seeded for values of the detuning within a certain range. We have unintentionally operated at a MOTC DP VCO detuning which unseeded MOGC, so it is critical to determine the acceptable range of detunings by looking at the power of the MOGC output as the detuning is varied. If needed, the frequency of the HF IMC DP VCO can be adjusted to reach a desired imaging frequency to compensate for limitations in the MOTC DP VCO detuning.

A.4 Force cancellation

Minimizing the presence of forces arising from magnetic field gradients is of critical importance in our BEC experiments. To see this, consider the first-order Zeeman shift in energy of an atomic hyperfine state with nuclear spin I, total electronic angular momentum J, and corresponding quantum numbers m_I and m_J, respectivley, due to a strong magnetic field $B(\mathbf{r})$ [1]:

$$\Delta E = g_J m_J \mu_B B(\mathbf{r}) + A m_I m_J, \tag{A.13}$$

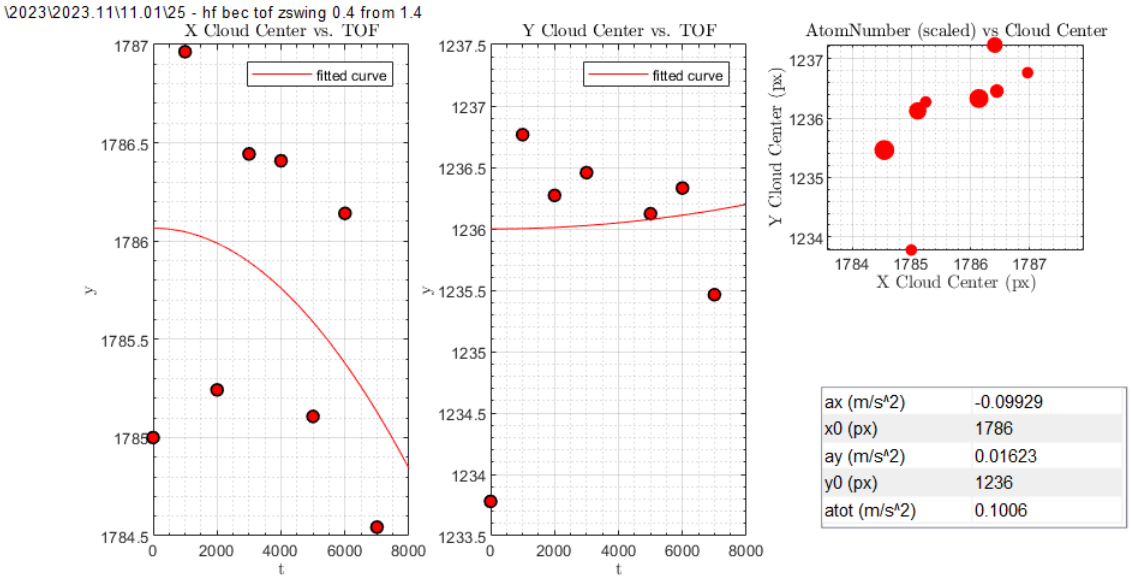

Figure A.2: Example data from a force cancellation run with a $240a_0$ BEC, showing an good degree of force cancellation. The cloud centers along each axis are plotted against TOF, and parabolic fits extract the accelerations along each axis. In addition to the accelerations from the fits, the maximum change in position along each axis should be taken into account in case the fitting is bad. Typically, we can keep the maximum change in position along each axis to five pixels or less.

Here, g_J is the Landé g-factor, μ_B is the Bohr magneton and A is the hyperfine structure constant. From $\mathbf{F}(\mathbf{r}) = -\nabla U(\mathbf{r})$, we see that $\mathbf{F}(\mathbf{r}) = -g_J m_J \mu_B \nabla B(\mathbf{r})$. The first point to emphasize is that one must apply a constant magnetic field gradient to exert a constant force. The second point to note is that all magnetic fields with non-zero higher derivatives, e.g. $\nabla^2 B \neq 0$, will also result in a force on the atoms. We believe that these higher-order derivatives, stemming from residual field curvature, are what cause the significant downward ($-\hat{\mathbf{z}}$) acceleration of our clouds when the Feshbach field is generated.

Most of our experiments rely on the mapping between momentum and position space through time of flight, so it is important to minimize unwanted forces on the BEC so that the linear mapping between momentum and position is preserved. Force cancellation is our primary method of mitigating these forces, and it is achieved using two sets of "wing" coils (because they look like angel wings?) which allow us to force cancel along the lattice and slower axes; we do not currently have the ability to force cancel in the vertical direction. However, we have had discussions of implementing a circuit which would allow us to switch between current supplies so that the vertical shims, which are currently used for D1 pumping, could be used to force cancel the vertical direction, though the distance of these coils from the chamber and their relatively low gauge wire may require significant amounts of current. It is unclear if this would be a significant issue given that our BEC experiments to-date have been around a second, at most.

The force cancellation procedure is relatively straightforward. First, a diagnostic TOF sequence is taken, and if the degree of force cancellation is unknown, it is a good idea to do this with a standard high-field $240a_0$ condensate (the procedure can be repeated for weaker and non-interacting clouds once the high-field BEC is force canceled). From this sequence of images, we extract the cloud position along each axis as a function of TOF. Perfect force cancellation would correspond to no movement of the cloud along any axis. Note: the force calibration curves for the wing coils in the "Lithium Useful Info" binder are only valid if the PCO images are rotated before analysis so that the lattice axis is in the y-direction. The rotation angle θ which meets this requirement is about -9.2° counter-clockwise. From the diagnostic TOF and with the correct rotation angle, the accelerations along the transverse and slower axes are given. Then, using the wing coil calibration curves, we can estimate the amount by which the current in each set of the wing coils needs to change. While ideally each set of wing coils would only produce a force along one axis, there is some degree of cross-talk between the coils, so some iteration is required to get good force cancellation. Typically, at lower TOFs (roughly 10 ms and below), we are able to constrain the magnitude of the acceleration along each axis to be less than 0.5 m/s^2. Figure A.2 shows an example of the cloud center movement with good force cancellation.

As a final note, the currents in each set of coils required to achieve force cancellation will change over time as movement of the ODT beams changes the position, and thus the force environment, in which the BEC is born. So, we should check force cancellation whenever the ODT beams move or are suspected to have moved, at the very least, but checking every month or so even if the beams haven't moved is probably a good idea.

A.5 Lattice alignment

Coarse alignment of the lattice requires a BEC to which the lattice beam can be aligned and optimized with Kapitza-Dirac diffraction. The BEC should be imaged from the side bucket Basler (lattice) axis to obtain the cloud center position, and in general it is good practice to take three to ten repeats to make sure the center position is accurate. Then, with the lattice beam at very low power (probably only enable the preamp on the ALS), one can override the MOT flip mirrors so that the lattice beam can enter and exit the chamber and reach the side bucket Basler. If the lattice is completely misaligned, the first step is to roughly center the beam on the pre-chamber focusing lens on the East side. Then, the picomotors for the lattice being aligned can be adjusted to center the beam on the BEC center position on the side bucket Basler. From here, the retro-reflected beam alignment can be optimized by first adjusting the retro mirror so that there is light all the way back to the isolator for the 1064 nm laser, and then putting a power meter at one of the rejection ports of the PAVOS isolator (there are multiple) and doing a finer optimization of the retro mirror to maximize the rejected power (any increase in the rejected power will only be due to better retro-alignment of the lattice beam). This procedure should result in a lattice which is relatively close to being properly aligned,

and the fine adjustments to the retro beam can be made using Kapitza-Dirac diffraction, which is discussed in the next section. The lattice alignment process should not need to be repeated for the non-interacting BEC if force cancellation is done properly at high field.

A.6 Lattice calibration techniques

Kapitza-Dirac diffraction is the technique most commonly employed on our experiment to obtain a calibration curve of lattice depth as a function of the VVA voltage set in Cicero. After optical evaporation, one of the two lattices is pulsed on for between 300 ns and 1 μs (at least when there's a bunch of power from the ALS). After a short time-of-flight, somewhere around 1.25 ms, an image of the cloud is taken to observe the spatially separated $\pm 2n\hbar k_L$ momentum orders. The known functional form of the population in each order for a given lattice depth and pulse duration is then used to back out the lattice depth. Note, though, that because the powers in the lattice beams are set using VVAs instead of PIDs (what the ODT beams have), the non-linear relationship between optical power and VVA voltage needs to be taken into account. This is taken care of in the existing KD code, but essentially what it does is pull voltage data from the lattice photodiode and associate each PD voltage with a certain distribution amongst momentum orders. A fit to order population versus lattice photodiode voltage is then generated and the free fit parameter gives the strength of the lattice in recoil energies per volt, i.e. E_R/Volt; this number is typically about 150 E_R/V for recent lattice experiments. Note that this process relies on the human running the code to decide which fit parameter best captures the data, and in this way there is likely something that can be done to make this process more robust and less of an interpretive art. However, once this value is extracted, one can then set the lattice depth by back-calculating the corresponding photodiode voltage for the desired depth and then finding through trial-and-error the lattice VVA voltage which gives this PD reading.

A.7 Trap painting

One technique which really juiced the atom counts in our BECs is the implementation of trap painting, where the RF sources of both ODT AOMs are frequency modulated by another external function generator, in our case Siglent SDG2122X AWGs. The idea is that a shift in the drive frequency of an AOM results in the diffracted orders emerging at slightly different angles which manifests as a change in position when also considering the path length between the diffracted order and the atoms. In this way, sufficiently fast modulation of the AOM drive frequency results in a modified time-averaged trapping potential with a larger trap volume. This technique was first tested after we installed the Azurlight 130 W 1064 nm amplifier which allowed us to maximize the number of captured atoms as the sheer amount of power allowed for both trap painting and large

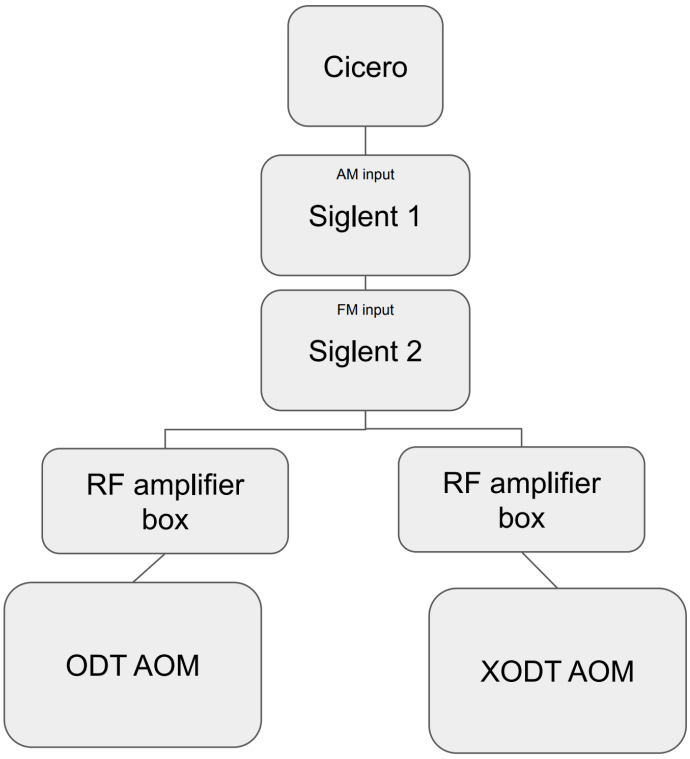

Figure A.3: Schematic of our trap painting setup.

atom capture.

Our trap painting scheme is accomplished using two Siglent SDGS2122X arbitrary waveform generators, as shown in Figure A.3, and we'll refer to the Siglents as S1 and S2 for brevity. The settings are listed at the end of this section. Here's how our trap painting setup works:

1. An analog voltage from Cicero is sent to the Aux In/Out port of S1. S1 is set to generate and output a 10 kHz signal, and this is the frequency modulation signal. S1 is configured to be in AM mode with an external source, and the amplitude of the output signal is determined by the voltage sent from Cicero.

2. The output of S1 is sent to the Aux In/Out port of S2. S2 is responsible for generating the RF waveforms which are amplified to drive both the ODT and XODT AOMs. Both S2 outputs are set to FM mode with the source set to external with frequency deviations of 2 MHz. This means that the frequency of each channel changes by $\pm$ 2 MHz at most.

3. By changing the voltage from Cicero, we can vary the amount of frequency modulation in the ODT and XODT RF signals which determines how far each beam

moves, i.e. we can paint the trap more or less by changing the voltage from Cicero.

The degree to which the trap is painted is controlled by an analog voltage from Cicero, and this is what allows us to increase the painting strength from zero at the start of transfer hold (transfer from magnetic trap to optical dipole trap) to some maximum value and then ramp the strength down during optical evaporation. Currently, the KP1VVA analog output channel in Cicero controls the painting strength. We have typically found that a maximum frequency deviation of 3 MHz or less is what our ODT PIDs can handle before (we think) movement of the beam off of the photodiode causes the PIDs to flip out. Several attempts have been made to check the alignment of each ODT beam to their respective photodiodes, but it has not been immediately obvious that either beam is close the edge of the PD, and attempts to improve the alignment have proved very challenging due to the location of the relevant optics.

For reference, here are the current settings as of February 2024:

- Siglent 1 channel 1:
  - Mode: amplitude modulation
  - Source: external
  - Frequency: 10 kHz
  - Amplitude: 6 V_{pp}
  - Offset: 0 Vdc
  - Phase: 0°
  - Load: HiZ
- Siglent 2 channel 1 (ODT channel):
  - Mode: frequency modulation
  - Source: external
  - Frequency: 99.2 MHz
  - Amplitude: 1.8 V_{pp}
  - Offset: 0 Vdc
  - Phase: 0°
  - Frequency deviation: 2 MHz
  - Load: 50 Ω
- Siglent 2 channel 2 (XODT channel):
  - Mode: frequency modulation
  - Source: external

- Frequency: 99 MHz
- Amplitude: 1.5 V_{pp}
- Offset: 0 Vdc
- Phase: 0°
- Frequency deviation: 2 MHz
- Load: 50 Ω

A.8 ODT beam PID controller

The control scheme for our dipole trap beams is unique in that it is the only instance in which we use PID control to set the beam powers via set point voltages, as opposed to sending voltages directly to their VVAs, which are non-linear devices. PID control is used to bypass this non-linearity, allowing us to create ODT ramp profiles in Cicero which directly set the optical powers.

Starting from Cicero, two analog output channels are dedicated to the ODT and XODT beams and the voltages from these outputs determine the respective power set points for each beam. As photodiode voltage is approximately linear with power, each set point is a proxy for the power the beam. Due to the finite resolution of the National Instruments analog card outputs, about 5 mV, it is important to maximize the dynamic range of usable set point voltages. As a concrete example, if a set point of 1.2 V is applied to the PID controller from Cicero, but the optical in that particular beam does not result in a photodiode voltage greater than 1 V, we are limited in our control of the beam to the range 0-1 V. That gives us 1 V/5 mV= 200 points of granularity between 0 W and the beam's maximum power, say, 20 W. Then, each increment in voltage between corresponds to a change of 200 mW, which is quite large. The remedy for this is accomplished with a simple voltage divider which scales the relevant voltage from Cicero, 0-10 V, to an appropriate range for the set point of the PID controller for a given beam. A power calibration for each trapping beam is taken by varying the PID set point and measuring the post-chamber power with a high-power power head. This calibration reveals not only the power balance between the two dipole beams, but also the set point voltage at which each beam power is maximized. This can then be used to construct a voltage divider which ideally maps the relevant Cicero range to the relevant PID set point range.

A.9 Requirements for each cooling stage

1. Factors affecting the MOT:
    - Field strength in Zeeman slower sections as set by their respective current supplies. Most important from section D to A (reverse order).
    - Cycler and repump powers.

- MOT beam polarization
- Overlap between field zero and MOT beam intersection
- Atomic beam shutter
- Oven temperature/atomic flux
- Cycler, repump and Zeeman slower beam frequencies
- Zeeman slower beam power
- Zeeman slower beam alignment and focusing
- Counter-propagating-ness of MOT beams along same axes
- MOT beam power balance, typically adjusted via the telescope lenses
- Shimming of the Earth's magnetic field

2. Factors affecting GM:

   - Forward beam alignment/overlap with MOT
   - Retro beam alignment
   - Power
   - GM EOM frequencies
   - GM DP AOM frequency
   - Which sideband on GM injection lock
   - Duration of GM in sequence (GMTime)
   - Polarization (pre-retro waveplate)

3. Factors affecting D1 pumping:

   - Power
   - Frequency (D1 AOM and relevant GM optics)
   - Polarization, to a much greater degree than GM
   - Alignment to GM
   - Bias field
   - Duration of D1 pumping in sequence (D1PumpTime)

4. Factors affecting RF evaporation:

   - Plug beam flag
   - Plug beam power
   - Plug beam focusing and alignment
   - Centering of MOT relative to magnetic trap field zero
   - RF frequency sweep rate, initial and final frequency values
   - RF power
   - Stability of coils and location of field zero

- Generating large enough field/are current supplies hitting 500 A each?

5. Factors affecting ODTs:
    - Where ODTs overlap relative to plug beam in the cloud
    - ODT power, alignment and overlap (relative to each other)
    - Trap painting/how to ramp up the painting strength
    - ODT AOM frequencies relative to each other/which AOM orders are used for ODTs
    - Temperature of cloud at evapD
    - Ramping down plug beam power and blocking with flag
6. Factors affecting state transfer:
    - Bias field along Zeeman slower axis using slower shim supply
    - RF sweep rate, initial and final frequencies
    - RF power HOW MUCH DO WE USE
7. Factors affecting optical evaporation and BEC formation:
    - OpEvap time, decay time tau
    - Painting on or off, how the painting strength is ramped down
    - Beam powers, relative power balance between beams (should be roughly 3:5 or 5:7 ODT:XODT, XODT has telescope that ODT path doesn't)
    - Interference between ODT beams/using different AOM orders
    - Thermalization rate via scattering length CHECK/set by magnetic field
    - Degree of evaporation/dividing down more or less
8. Factors affecting HF BEC quality and stability:
    - Force cancellation, undesired field gradients, shimming of Earth's field
    - Temperature in ODTs
    - Stray light (plug beam, zeroth order resonant light, LEDs on shutter PCBs, GM path, ZS path)
    - evapD stability
    - 1064 power stability, properly following PID set points during optical evaporation
    - Residual field curvature
    - HF imaging frequency (affects the apparent quality and atom number of the BEC)

9. Factors affecting NI BEC quality and stability:

    - HF force cancellation
    - NI force cancellation
    - Scattering length at NI, i.e. is it actually non-interacting
    - Field transition ramp time
    - Value of curve field at NI
    - NI imaging frequency (affects the apparent quality and atom number of the BEC)

A.10 Oven nozzle construction

The pre-Peter Dotti nozzle design used a double-sided blank 316 SS flange as the basis for the nozzle. The V-shaped cutout, known as the V-groove, has typically been done by the Physics Machine Shop using a wire EDM which allows the bottom of the V to be cut precisely, at least when done properly. Due to the packing structure resulting from stacked microcapillaries, it is critical that the bottom of the V-groove only hold a single tube, so the diameter of the wire EDM cut should be about the outer diameter of a single tube. In cases where the bottom of the groove supported more than one tube, it has been virtually impossible to create the desired array as tubes can be pushed into and out of the groove, resulting in a highly unstable array (pushing on the top of the array would cause the other tubes to shift around, was not stable even when clamped). The Dotti design, which will be discussed further in Peter Dotti's thesis, completely solves the V-groove issue as instead of a groove, it uses two machined triangles which form a V when placed facing one another. It is much easier to cut a very sharp edge on an outer surface than an inner one because the cutting radius of the tool does not impact the final shape or sharpness of the triangles. The portion of a Peter design nozzle that worked on had perfect packing, so this nozzle design revision is definitely superior. This also eliminates the risk associated with machining a part that has a knife edge; we have had setbacks from knife edges which were deformed somehow during machine of the V-groove.

For either nozzle design, construction largely consists of carefully placing microcapillaries into the V-groove. We have often attached 1/2" posts to a small optical breadboard and used RA90s to create a sort of holder for the nozzle flange. It is much easier to place the tubes if the nozzle flange is held at an angle instead of straight up and down. As the tubes are liable to spill and get all over the place, we use a tray made from aluminum foil to catch any wayward capillaries. We use a microscope with a ring light around its objective lens to look at the V-groove and assess the packing quality as tubes are deposited (at least one of the earliest nozzles was built by-eye). A pair of tweezers with a curve is also quite helpful given the orientation of the nozzle when packing.

A.11 Baking

Achieving and maintaining ultra-high vacuum is critical for the operation of any cold atom machine, and baking is one of the tools which makes UHV possible. The purpose of a bake is to remove water and other chemical compounds which limit the ultimate pressure that can be achieved in a particular vacuum system. In our lab, machine bakes use an external turbomolecular pump connected to the machine via a bellows to pump out material which is liberated during the bake. The machine itself is covered in heating elements and thermocouples and then wrapped in insulation, be it foil or fiberglass wrapped in foil. It is important to have enough heating elements so that the temperatures of the various vacuum components can be controlled and kept in a tight grouping around the same temperature. The heating elements are AC-powered and are connected to Variacs, which are variable voltage transformers which take 120 V AC and convert it down to a lower voltage. This allows one to adjust the amount of heat generated by each heating element and thus keep temperatures approximately uniform across the machine and minimize thermal gradients. Thermal gradients, specifically across CF flanges and seals, can result in the failure of the gasket seal and thus leaks, so it is key to minimize thermal gradients. Bakes operate at elevated temperatures as vapor pressure is exponential in temperature so baking for a week at 200° C will result in significantly better pressures than baking for two weeks at 100° C. Ramping to bake temperature from room temperature has a timescale typically limited by view ports and windows, both of which have glass-to-metal seals which can only be safely ramped at a certain rate, something like 2-3° C/min for the lithium view ports. Additionally, ramping temperatures quickly makes it more challenging to correct for gradients. The turbo pump is often used instead of ion pumps as the lifetime of the turbo does not depend on how much crap it pumps out, and ion pump performance, at least for Gamma ion pumps, starts to degrade above 85° C. Also, bake temperatures by design should result in a much higher gas load in the system and thus higher pressure and depending on how high the pressure goes, this may mean ion pump lifetimes are significantly reduced if run at this pressure. Hydrogen bakes are done typically around 450° C, and as the name suggests, the purpose is to remove hydrogen embedded within vacuum components. Once liberated, hydrogen does not meaningfully re-enter the component, so unlike a water bake, hydrogen bakes can often be done without actually pumping on the components while they are baked. Hydrogen bakes become necessary when trying to achieve UHV pressures. Glass-to-metal seals are also usually the limiting factor on the maximum safe bake temperature, though anti-reflection coatings on windows can also limit the ultimate temperature.

Appendix B

Analysis and simulation code

For the purposes of ease of access and wider distribution, the relevant code for each of the following sections has been uploaded to the Weld lab GitHub, which can be found at `https://github.com/weldlabucsb`.

B.1 Extracting thermodynamic quantities from experimental images

Refer to `https://github.com/weldlabucsb/thermodynamicEngineAnalysis`.

B.2 Simulating a continuously trapped atom interferometer

Refer to `https://github.com/weldlabucsb/ScienceInSilico/tree/main/atomInterferometry`.

Bibliography

[1] C. J. Foot, *Atomic Physics*. Oxford University Press, 2005.

[2] L. Pitaevskii and S. Stringari, *Bose-Einstein Condensation*. Oxford University Press, 2003.

[3] C. Pethick and H. Smith, *Bose-Einstein Condensation in Dilute Gases*. Cambridge University Press, 2nd ed., 2008.

[4] M. Holthaus, *Floquet engineering with quasienergy bands of periodically driven optical lattices*, *J. Phys. B: At. Mol. Opt. Phys.* **49** (2016), no. 1 013001.

[5] E. Q. Simmons, R. Sajjad, K. Keithley, H. Mas, J. L. Tanlimco, E. Nolasco-Martinez, Y. Bai, G. H. Fredrickson, and D. M. Weld, *Thermodynamic engine with a quantum degenerate working fluid*, *Phys. Rev. Res.* **5** (Oct, 2023) L042009.

[6] K. Singh, *Floquet Engineering with Ultracold Lithium in Optical Lattices*. PhD thesis, UC Santa Barbara, 2019.

[7] Z. A. Geiger, *An Apparatus for Dynamical Quantum Emulation Using Ultracold Lithium*. PhD thesis, UC Santa Barbara, 2017.

[8] C. Chin, R. Grimm, P. Julienne, and E. Tiesinga, *Feshbach Resonances in Ultracold Gases*, *Reviews of Modern Physics* **82** (Apr., 2010) 1225–1286.

[9] S. E. Pollack, D. Dries, M. Junker, Y. P. Chen, T. A. Corcovilos, and R. G. Hulet, *Extreme Tunability of Interactions in a Li 7 Bose-Einstein Condensate*, *Physical Review Letters* **102** (Mar., 2009) 090402.

[10] Z. A. Geiger, K. M. Fujiwara, K. Singh, R. Senaratne, S. V. Rajagopal, M. Lipatov, T. Shimasaki, R. Driben, V. V. Konotop, T. Meier, and D. M. Weld, *Observation and Uses of Position-Space Bloch Oscillations in an Ultracold Gas*, *Physical Review Letters* **120** (May, 2018) 213201.

[11] K. M. Fujiwara, Z. A. Geiger, K. Singh, R. Senaratne, S. V. Rajagopal, M. Lipatov, T. Shimasaki, and D. M. Weld, *Experimental realization of a relativistic harmonic oscillator*, *New J. Phys.* **20** (2018), no. 6 063027.

[12] C. Fujiwara, K. Singh, Z. A. Geiger, R. Senaratne, S. V. Rajagopal, M. Lipatov, and D. M. Weld, *Transport in floquet-bloch bands*, *Phys. Rev. Lett.* **122** (2019), no. 1 010402.

[13] A. Cao, C. J. Fujiwara, R. Sajjad, E. Q. Simmons, E. Lindroth, and D. Weld, *Probing nonexponential decay in floquet–bloch bands*, *Zeitschrift für Naturforschung A* **75** (May, 2020) 443–448.

[14] R. Sajjad, J. L. Tanlimco, H. Mas, A. Cao, E. Nolasco-Martinez, E. Q. Simmons, F. L. N. Santos, P. Vignolo, T. Macrì, and D. M. Weld, *Observation of the quantum boomerang effect*, *Phys. Rev. X* **12** (Feb, 2022) 011035.

[15] K. Singh, C. Fujiwara, Z. Geiger, E. Simmons, M. Lipatov, A. Cao, P. Dotti, S. Rajagopal, R. Senaratne, T. Shimasaki, M. Heyl, A. Eckardt, and D. Weld, *Quantifying and controlling prethermal nonergodicity in interacting floquet matter*, *Phys. Rev. X* **9** (2019), no. 4 041021.

[16] A. Cao, R. Sajjad, H. Mas, E. Q. Simmons, J. L. Tanlimco, E. Nolasco-Martinez, T. Shimasaki, H. E. Kondakci, V. Galitski, and D. M. Weld, *Interaction-driven breakdown of dynamical localization in a kicked quantum gas*, *Nature Physics* **18** (Nov., 2022) 1302–1306.

[17] A. Cao, R. Sajjad, E. Q. Simmons, C. J. Fujiwara, T. Shimasaki, and D. M. Weld, *Transport controlled by poincaré orbit topology in a driven inhomogeneous lattice gas*, *Phys. Rev. Res.* **2** (Aug, 2020) 032032.

[18] C. J. Fujiwara, *Dynamics of Ultracold Lithium in Modulated Optical Lattices*. PhD thesis, UC Santa Barbara, 2019.

[19] S. V. Rajagopal, *Realizing and probing driven quantum systems with ultracold gases*. PhD thesis, UC Santa Barbara, 2019.

[20] R. Senaratne, *Quantum Simulation of Strongly-Driven Systems Using Ultracold Lithium and Strontium*. PhD thesis, UC Santa Barbara, 2018.

[21] R. Sajjad, *Driving Fast and Slow: Dynamics of Periodically Modulated Quantum Gases*. PhD thesis, UC Santa Barbara, 2024.

[22] R. Senaratne, S. V. Rajagopal, Z. A. Geiger, K. M. Fujiwara, V. Lebedev, and D. M. Weld, *Effusive atomic oven nozzle design using an aligned microcapillary array*, *Rev. Sci. Instrum.* **86** (2015), no. 2 023105.

[23] A. T. Grier, I. Ferrier-Barbut, B. S. Rem, M. Delehaye, L. Khaykovich, F. Chevy, and C. Salomon, Λ*-enhanced sub-doppler cooling of lithium atoms in* D_1 *gray molasses*, *Phys. Rev. A* **87** (Jun, 2013) 063411.

[24] M. Weidemüller, T. Esslinger, M. A. Ol'shanii, A. Hemmerich, and T. W. Hänsch, *A Novel Scheme for Efficient Cooling below the Photon Recoil Limit*, *Europhysics Letters (EPL)* **27** (July, 1994) 109–114.

[25] S. Giorgini, L. P. Pitaevskii, and S. Stringari, *Condensate fraction and critical temperature of a trapped interacting bose gas*, *Phys. Rev. A* **54** (1996), no. 6 R4633–R4636.

[26] W. Ketterle, D. S. Durfee, and D. M. Stamper-Kurn, *Making, probing and understanding Bose-Einstein condensates*, Apr., 1999. arXiv:cond-mat/9904034.

[27] J. Szczepkowski, R. Gartman, M. Witkowski, L. Tracewski, M. Zawada, and W. Gawlik, *Analysis and calibration of absorptive images of bose–einstein condensate at nonzero temperatures*, *Review of Scientific Instruments* **80** (2009), no. 5 053103.

[28] R. Grimm, M. Weidemüller, and Y. B. Ovchinnikov, *Optical dipole traps for neutral atoms*, in *Advances In Atomic, Molecular, and Optical Physics* (B. Bederson and H. Walther, eds.), vol. 42, pp. 95–170. Academic Press, 2000.

[29] F. Bloch, *Über die quantenmechanik der elektronen in kristallgittern*, *Z. Physik* **52** (1929), no. 7 555–600.

[30] M. Ben Dahan, E. Peik, J. Reichel, Y. Castin, and C. Salomon, *Bloch oscillations of atoms in an optical potential*, *Phys. Rev. Lett.* **76** (1996), no. 24 4508–4511.

[31] H. T. Quan, Y.-x. Liu, C. P. Sun, and F. Nori, *Quantum thermodynamic cycles and quantum heat engines*, *Phys. Rev. E* **76** (sep, 2007) 031105.

[32] Y. Zheng and D. Poletti, *Work and efficiency of quantum otto cycles in power-law trapping potentials*, *Phys. Rev. E* **90** (July, 2014) 012145.

[33] Y. Zheng and D. Poletti, *Quantum statistics and the performance of engine cycles*, *Phys. Rev. E* **92** (July, 2015) 012110.

[34] R. Kosloff and Y. Rezek, *The quantum harmonic otto cycle*, *Entropy* **19** (2017), no. 4 136.

[35] S. Hamedani Raja, S. Maniscalco, G. S. Paraoanu, J. P. Pekola, and N. Lo Gullo, *Finite-time quantum Stirling heat engine*, *New J. Phys.* **23** (Mar., 2021) 033034.

[36] M. Beau, J. Jaramillo, and A. Del Campo, *Scaling-up quantum heat engines efficiently via shortcuts to adiabaticity*, *Entropy* **18** (2016), no. 5 168.

[37] J. Li, T. Fogarty, S. Campbell, X. Chen, and T. Busch, *An efficient nonlinear Feshbach engine*, *New J. of Phys.* **20** (Jan., 2018) 015005.

[38] Y.-Y. Chen, G. Watanabe, Y.-C. Yu, X.-W. Guan, and A. del Campo, *An interaction-driven many-particle quantum heat engine and its universal behavior*, *npj Quantum Inf.* **5** (oct, 2019) 1–6.

[39] N. Yunger Halpern, C. D. White, S. Gopalakrishnan, and G. Refael, *Quantum engine based on many-body localization*, *Phys. Rev. B* **99** (2019), no. 2 024203.

[40] G. Barontini and M. Paternostro, *Ultra-cold single-atom quantum heat engines*, *New J. Phys.* **21** (2019), no. 6 063019.

[41] F. Carollo, K. Brandner, and I. Lesanovsky, *Nonequilibrium Many-Body Quantum Engine Driven by Time-Translation Symmetry Breaking*, *Phys. Rev. Lett.* **125** (Dec., 2020) 240602.

[42] T. Keller, T. Fogarty, J. Li, and T. Busch, *Feshbach engine in the Thomas-Fermi regime*, *Phys. Rev. Research* **2** (Aug., 2020) 033335.

[43] M. Gluza, J. a. Sabino, N. H. Ng, G. Vitagliano, M. Pezzutto, Y. Omar, I. Mazets, M. Huber, J. Schmiedmayer, and J. Eisert, *Quantum field thermal machines*, *PRX Quantum* **2** (Jul, 2021) 030310.

[44] M. Boubakour, T. Fogarty, and T. Busch, *Interaction-enhanced quantum heat engine*, *Phys. Rev. Research* **5** (2023), no. 1 013088.

[45] J. Eglinton, T. Pyharanta, K. Saito, and K. Brandner, *Thermodynamic geometry of ideal quantum gases: A general framework and a geometric picture of BEC-enhanced heat engines*, *arXiv.2212.12076* (Dec., 2022).

[46] N. M. Myers, F. J. Peña, O. Negrete, P. Vargas, G. De Chiara, and S. Deffner, *Boosting engine performance with Bose-Einstein condensation*, *New J. Phys.* **24** (Feb., 2022) 025001.

[47] J. Roßnagel, O. Abah, F. Schmidt-Kaler, K. Singer, and E. Lutz, *Nanoscale Heat Engine Beyond the Carnot Limit*, *Phys. Rev. Lett.* **112** (Jan., 2014) 030602.

[48] K. Zhang, F. Bariani, and P. Meystre, *Quantum Optomechanical Heat Engine*, *Phys. Rev. Lett.* **112** (Apr., 2014) 150602.

[49] J.-M. Park, S. Lee, H.-M. Chun, and J. D. Noh, *Quantum mechanical bound for efficiency of quantum Otto heat engine*, *Phys. Rev. E* **100** (July, 2019) 012148.

[50] F. Wu, L. Chen, F. Sun, C. Wu, F. Guo, and Q. Li, *Quantum degeneracy effect on performance of irreversible Otto cycle with ideal Bose gas*, *Energy Convers. and Manag.* **47** (Nov., 2006) 3008–3018.

[51] J. Roßnagel, S. T. Dawkins, K. N. Tolazzi, O. Abah, E. Lutz, F. Schmidt-Kaler, and Kilian Singer, *A single-atom heat engine*, *Science* **352** (2016), no. 6283 325–329.

[52] J. Bu, J. Zhang, G. Ding, J. Li, J. Zhang, B. Wang, W. Ding, W. Yuan, L. Chen, S. Özdemir, F. Zhou, H. Jing, and M. Feng, *Enhancement of quantum heat engine by encircling a Liouvillian exceptional point*, *Phys. Rev. Lett.* **130** (Mar, 2023) 110402.

[53] J. P. S. Peterson, T. B. Batalhão, M. Herrera, A. M. Souza, R. S. Sarthour, I. S. Oliveira, and R. M. Serra, *Experimental characterization of a spin quantum heat engine*, *Phys. Rev. Lett.* **123** (Dec, 2019) 240601.

[54] J.-P. Brantut, C. Grenier, J. Meineke, D. Stadler, S. Krinner, C. Kollath, T. Esslinger, and A. Georges, *A thermoelectric heat engine with ultracold atoms*, *Science* **342** (2013), no. 6159 713–715.

[55] Y. Zou, Y. Jiang, Y. Mei, X. Guo, and S. Du, *Quantum heat engine using electromagnetically induced transparency*, *Phys. Rev. Lett.* **119** (2017), no. 5 050602.

[56] J. Nettersheim, S. Burgardt, Q. Bouton, D. Adam, E. Lutz, and A. Widera, *Power of a quasispin quantum otto engine at negative effective spin temperature*, *PRX Quantum* **3** (Dec., 2022) 040334.

[57] I. Reyes-Ayala, M. Miotti, M. Hemmerling, R. Dubessy, H. Perrin, V. Romero-Rochin, and V. S. Bagnato, *Carnot Cycles in a Harmonically Confined Ultracold Gas across Bose–Einstein Condensation*, *Entropy* **25** (Feb., 2023) 311.

[58] J. Klatzow, J. N. Becker, P. M. Ledingham, C. Weinzetl, K. T. Kaczmarek, D. J. Saunders, J. Nunn, I. A. Walmsley, R. Uzdin, and E. Poem, *Experimental demonstration of quantum effects in the operation of microscopic heat engines*, *Phys. Rev. Lett.* **122** (2019), no. 11 110601.

[59] Q. Bouton, J. Nettersheim, S. Burgardt, D. Adam, E. Lutz, and A. Widera, *A quantum heat engine driven by atomic collisions*, *Nat. Commun.* **12** (2021), no. 1 2063.

[60] J. Koch, K. Menon, E. Cuestas, S. Barbosa, E. Lutz, T. Fogarty, T. Busch, and A. Widera, *A quantum engine in the BEC–BCS crossover*, *Nature* **621** (2023), no. 7980 723–727.

[61] J.-M. Park, S. Lee, H.-M. Chun, and J. D. Noh, *Quantum mechanical bound for efficiency of quantum otto heat engine*, *Phys. Rev. E* **100** (2019), no. 1 012148.

[62] G. Watanabe, B. P. Venkatesh, P. Talkner, M.-J. Hwang, and A. del Campo, *Quantum statistical enhancement of the collective performance of multiple bosonic engines*, *Phys. Rev. Lett.* **124** (2020), no. 21 210603.

[63] J. Jaramillo, M. Beau, and A. d. Campo, *Quantum supremacy of many-particle thermal machines*, *New J. Phys.* **18** (2016), no. 7 075019.

[64] K. Keithley, *Complex Langevin simulation of the coherent states path integral for bosonic many-body problems*. PhD thesis, UC Santa Barbara, 2024.

[65] C. Zener, *Non-adiabatic crossing of energy levels*, *Proc. R. Soc. A* **137** (1932), no. 833 696–702.

[66] S. Stringari, *Collective excitations of a trapped bose-condensed gas*, *Phys. Rev. Lett.* **77** (1996), no. 12 2360–2363.

[67] A. Cao, *Studying quantum dynamics in driven degenerate gases*. Undergraduate dissertation, UC Santa Barbara, 2021.

[68] E. W. Weisstein, "Abel transform." https://mathworld.wolfram.com/AbelTransform.html.

[69] M.-G. Hu, M. J. Van de Graaff, D. Kedar, J. P. Corson, E. A. Cornell, and D. S. Jin, *Bose polarons in the strongly interacting regime*, *Phys. Rev. Lett.* **117** (2016), no. 5 055301.

[70] F. Dalfovo, C. Minniti, S. Stringari, and L. Pitaevskii, *Nonlinear dynamics of a Bose condensed gas*, *Physics Letters A* **227** (Mar., 1997) 259–264.

[71] M. J. Moran and H. N. Shapiro, *Fundamentals of Engineering Thermodynamics*. Wiley, 2006.

[72] V. Romero-Rochín, *Equation of state of an interacting bose gas confined by a harmonic trap: The role of the "harmonic" pressure*, *Phys. Rev. Lett.* **94** (2005), no. 13 130601.

[73] V. Romero-Rochín and V. S. Bagnato, *Thermodynamics of an ideal gas of bosons harmonically trapped: equation of state and susceptibilities*, *Brazilian Journal of Physics* **35** (Sept., 2005) 607–613.

[74] N. Sandoval-Figueroa and V. Romero-Rochín, *Thermodynamics of trapped gases: Generalized mechanical variables, equation of state, and heat capacity*, *Physical Review E* **78** (Dec., 2008) 061129.

[75] C. Mishra and T. Busch, 2023. Private correspondence.

[76] J. G. Muga, X. Chen, A. Ruschhaupt, and D. Guéry-Odelin, *Frictionless dynamics of bose–einstein condensates under fast trap variations*, *J. Phys. B: At. Mol. Opt. Phys.* **42** (2009), no. 24 241001.

[77] T.-Y. Huang, B. A. Malomed, and X. Chen, *Shortcuts to adiabaticity for an interacting bose–einstein condensate via exact solutions of the generalized ermakov equation*, *Chaos* **30** (2020), no. 5 053131.

[78] P. R. Berman, *Atom Interferometry*. Academic Press, 1997.

[79] K. E. McAlpine, D. Gochnauer, and S. Gupta, *Excited-band bloch oscillations for precision atom interferometry*, *Phys. Rev. A* **101** (2020), no. 2 023614.

[80] T. Rahman, A. Wirth-Singh, A. Ivanov, D. Gochnauer, E. Hough, and S. Gupta, *Bloch Oscillation Phases investigated by Multi-path Stuckelberg Atom Interferometry*, Apr., 2023. arXiv:2308.04134.

[81] S. Shevchenko, S. Ashhab, and F. Nori, *Landau–zener–stückelberg interferometry*, *Physics Reports* **492** (2010), no. 1 1–30.

[82] L. Salasnich, A. Parola, and L. Reatto, *Effective wave equations for the dynamics of cigar-shaped and disk-shaped bose condensates*, *Phys. Rev. A* **65** (2002), no. 4 043614.